

## N O T I C E

THIS DOCUMENT HAS BEEN REPRODUCED FROM  
MICROFICHE. ALTHOUGH IT IS RECOGNIZED THAT  
CERTAIN PORTIONS ARE ILLEGIBLE, IT IS BEING RELEASED  
IN THE INTEREST OF MAKING AVAILABLE AS MUCH  
INFORMATION AS POSSIBLE

JPL PUBLICATION 81-77

(NASA-CR-168426) CONTROL SYSTEM DESIGN FOR  
THE LARGE SPACE SYSTEMS TECHNOLOGY REFERENCE  
PLATFORM (Jet Propulsion Lab.) 112 p  
HC A06/MF A01

N82-17255

CSSL 229

Unclass

G3/18 08908

# Control System Design for the Large Space Systems Technology Reference Platform

Rance S. Edmunds

January 15, 1982



**NASA**

National Aeronautics and  
Space Administration

Jet Propulsion Laboratory  
California Institute of Technology  
Pasadena, California

JPL PUBLICATION 81-77

# **Control System Design for the Large Space Systems Technology Reference Platform**

**Rance S. Edmunds**

January 15, 1982

**NASA**

National Aeronautics and  
Space Administration

**Jet Propulsion Laboratory**  
California Institute of Technology  
Pasadena, California

The research described in this publication was carried out by the Jet Propulsion Laboratory, California Institute of Technology, under contract with the National Aeronautics and Space Administration.

## FOREWORD

The research described in this report was performed by the Control and Energy Conversion Division of the Jet Propulsion Laboratory.

## ACKNOWLEDGEMENTS

This report was prepared with the encouragement and support of Steve Szirmay, Manager of the Automated Systems Section, and Guillermo Rodriguez, Supervisor of the Analysis and Simulation Group. I would like to thank these two people as well as Fernando Tolivar, Dave Schaechter, and Tom Brown for stimulating and helpful discussions during the preparation of this report.

## ABSTRACT

This report documents modeling and control system design for the Large Space Systems Technology (LSST) Reference Platform. The LSST Reference Platform consists of a central bus structure, solar panels, and platform arms on which a variety of experiments may be mounted. Simple structural models and classical frequency domain control system designs are developed. The report shows that operation of multiple independently articulated payloads on a single platform presents major problems when subarc second pointing stability is required. Experiment compatibility will be an important operational consideration for systems of this type.

Contents

	<u>Page</u>
I. INTRODUCTION . . . . .	1
II. STRUCTURAL MODEL . . . . .	3
A. Configuration . . . . .	3
B. Parameter Values and Natural Frequencies . . . . .	3
C. Mode Shapes . . . . .	4
D. Controllability . . . . .	5
E. Observability . . . . .	7
III. CONTROL SYSTEM REQUIREMENTS . . . . .	17
A. Overview . . . . .	17
B. Stability Requirements . . . . .	17
IV. CONTROL SYSTEM DESIGN . . . . .	19
A. Control Concepts . . . . .	19
B. Bus Controller Design . . . . .	21
C. Experiment Controller Design . . . . .	24
D. Combined Design . . . . .	25
E. Closed Loop System Eigenvalues . . . . .	26
V. CONTROL SYSTEM EVALUATION . . . . .	35
A. Transient Response . . . . .	35
B. Additional Factors Which Can Affect Performance . . . . .	36
VI. SUMMARY AND FUTURE STUDY . . . . .	37
 APPENDICES	
A. MODEL FOR PLATFORM WITH FLEXIBLE CROSS ARMS . . . . .	39
B. MODEL FOR PLATFORM WITH RIGIDLY ATTACHED EXPERIMENTS . . . . .	52
C. TRANSFER FUNCTIONS . . . . .	69
D. MODEL FOR PLATFORM WITH TWO HINGED EXPERIMENTS ATTACHED . . . . .	86
E. A TECHNIQUE FOR RESHAPING THE RIGID BODY MODES OF A SPACECRAFT . . . . .	94
F. TIME RESPONSE PLOTS FOR RUN F10 . . . . .	100
REFERENCES . . . . .	105

## Tables

	Page
2-1. Parameter Values . . . . .	9
2-2. Natural Frequencies for the LSST Reference Platform . . . . .	10
2-3. Rigid Body Mode Shapes Before Reshaping . . . . .	11
2-4. Elastic Mode Shapes . . . . .	11
2-5. Rigid Body Mode Shapes After Reshaping . . . . .	12
2-6. $\phi^{TB}$ for Eigenvectors of Tables 2-4 and 2-5 . . . . .	12
2-7. $C\phi$ for Eigenvectors of Tables 2-4 and 2-5 . . . . .	12
3-1. Platform Requirements . . . . .	18
4-1. Control System Gains for Performance Analysis . . . . .	27
5-1. Performance Results . . . . .	36
A-1. Parameter Values . . . . .	46
A-2. Modal Frequencies (Hz) . . . . .	46
B-1. Run Parameters . . . . .	60
B-2. Natural Frequencies (Hz) . . . . .	61
B-3. Mode Shapes for Run 6 . . . . .	62



## Figures

		<u>Page</u>
1-1.	LSST Reference Platform Configuration . . . . .	2
2-1.	LSST Reference Platform Model . . . . .	13
2-2.	Rigid Body Modes Before Reshaping . . . . .	14
2-3.	First Four Elastic Modes . . . . .	15
2-4.	Rigid Body Modes After Reshaping . . . . .	16
4-1.	Control Concepts for the LSST Reference Platform . . . . .	28
4-2.	Bus Controller Block Diagram . . . . .	29
4-3.	Alternate Bus Controller Block Diagram . . . . .	30
4-4.	Experiment Controller Block Diagram . . . . .	31
4-5.	Control System Configuration . . . . .	32
4-6.	Closed Loop Pole Positions for Data Set 1 . . . . .	33
4-7.	Closed Loop Pole Positions for Data Set 2 . . . . .	34
A-1.	Platform Arm Model. . . . .	47
A-2.	Beam Element . . . . .	48
A-3.	Two Beam Elements . . . . .	49
A-4.	Mode Shapes . . . . .	50
A-5.	Cantilever Beam . . . . .	51
B-1.	Model for Platform X Axis . . . . .	63
B-2.	Two Element Types . . . . .	64
B-3.	Mode Shapes For Type 1 Element . . . . .	65
B-4.	Rigid Body Modes . . . . .	66
B-5.	Elastic Modes for Platform Arms . . . . .	67
B-6.	Elastic Modes for Solar Panels . . . . .	68
C-1.	Discrete Mass System . . . . .	81
C-2.	Pole/Zero Configuration for $\theta_1/T_1(S)$ . . . . .	82
C-3.	Pole/Zero Configuration for $\theta_2/T_2(S)$ . . . . .	83
C-4.	Pole/Zero Configuration for $\theta_1/T_2(S)$ and $\theta_2/T_1(S)$ . . . . .	84
C-5.	Pole/Zero Configuration for $\theta_1/T_3(S)$ and $\theta_3/T_1(S)$ . . . . .	85
D-1.	Experiment Package Configurations . . . . .	92
D-2.	Free Body Diagram for Experiment Packages . . . . .	93
E-1.	Reshaping Process for Mode Shapes Having Identical Eigenvalues. . .	99
F-1.	Actuator Torque and Angular Response for Experiment 1, Run F-10 . .	102
F-2.	Actuator Torque and Angular Response for Central Bus, Run F-10. . .	103
F-3.	Actuator Torque and Angular Response for Experiment 3, Run F-10 . .	104

## I. INTRODUCTION

This report documents modeling and control system design for the Large Space Systems Technology (LSST) Reference Platform. The LSST Reference Platform consists of a central bus structure, solar panels, and platform arms on which a variety of experiments may be mounted. Figure 1-1 shows one possible configuration.

The objective of this report is to identify major control problems associated with precision pointing of experiment payloads. Simple structural models and classical frequency domain control system designs are used.

A major result of this report is to show that operation of multiple independently articulated payloads on a single platform will present major problems when high performance is required. Experiment compatibility will be an important operational consideration for any systems of this type.

The report which follows has six sections and six appendices. Section II defines the structural model for the platform. Mode shapes and frequencies are presented and controllability/observability issues discussed. Section III defines control system requirements. In Section IV the control system design is developed. Rate plus position feedback controllers are used. Control system design is evaluated in Section V, and in Section VI a summary is given along with comments on future study options.

The Appendices document the model development for the platform structure. The model is developed in a building block fashion using finite element techniques. In Appendix A a model for the flexible platform cross arms is given. In Appendix B the flexible solar panels are added. Appendix C presents transfer functions for the model of Appendix B. Two-hinged experiments are added to the model in Appendix D, and in Appendix E a technique for reshaping rigid body modes is given. Appendix F presents time response plots in support of Section V.

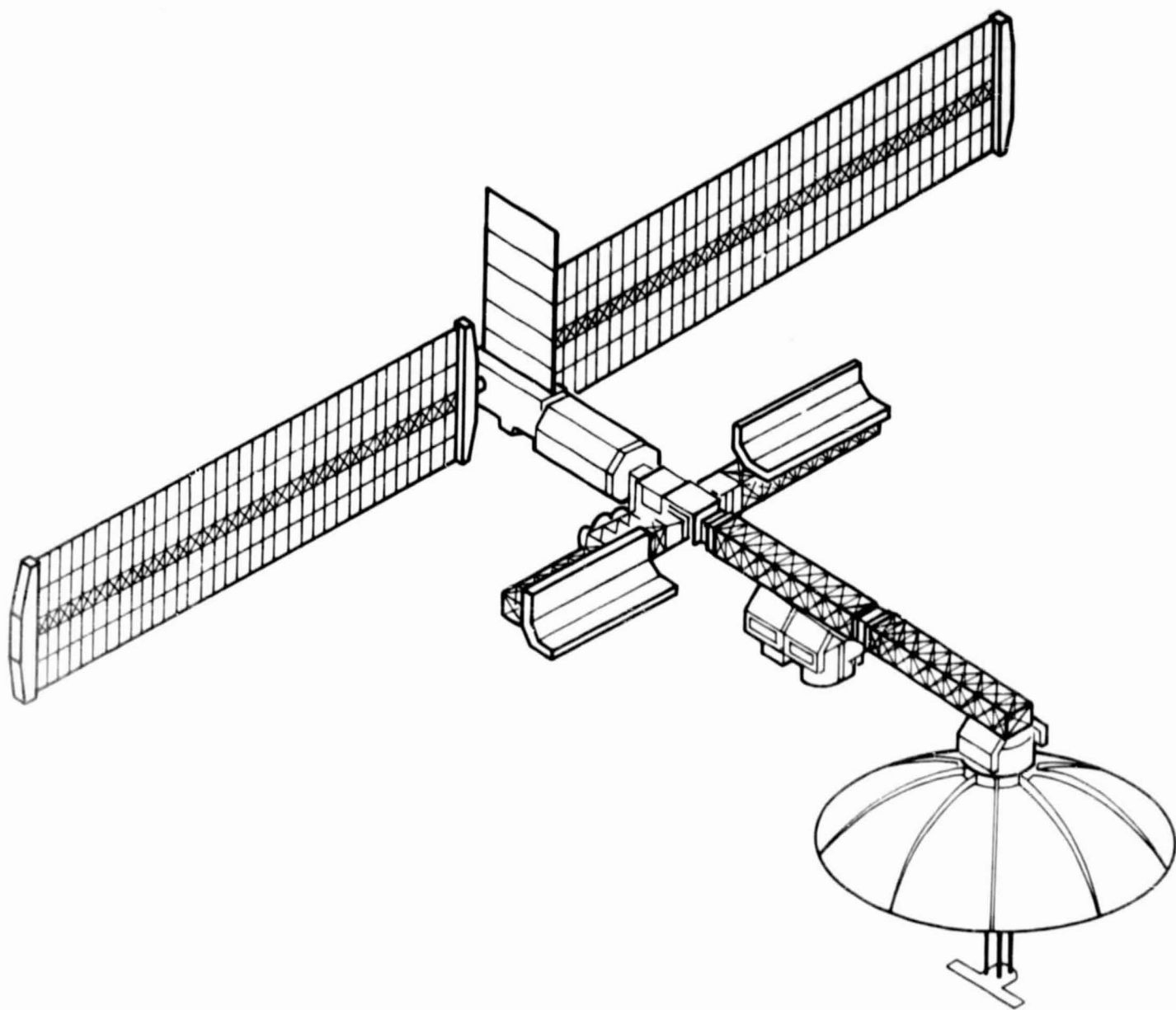


Fig. 1-1. LSST Reference Platform Configuration

## II. STRUCTURAL MODEL

This section presents mode shapes for the LSST Reference Platform. Techniques developed in Appendix E are used to reshape the rigid body mode shapes so that they are easier to interpret. Some comments on controllability and observability are then made.

### A. CONFIGURATION

Figure 2-1 shows a model of the spacecraft configuration. This configuration is the same as that presented in Appendix D. The variables  $V_i$   $i = 1, 2, \dots, 6$  are translational degrees of freedom;  $\theta_i$   $i = 1, 2, 3$  and  $\gamma_1, \gamma_3$  are rotational degrees of freedom.  $V_1, V_2, V_3, \theta_1, \theta_2,$  and  $\theta_3$  are associated with the platform arms,  $V_4, V_5,$  and  $V_6$  with the solar panels and  $\gamma_1, \gamma_3$  with the experiment packages. The central bus mass and inertia are represented by  $M_2, M_5, I_2,$  and  $I_5$  ( $M_2 = M_5 = 1/2$  total bus mass,  $I_2 = I_5 = 1/2$  total bus inertia). The bus is assumed to be rigid.

The experiment packages are hinged with respect to their bases. These bases have masses  $M_1, M_3$  and inertias  $I_1, I_3$  and are connected to the central bus by massless beams of length  $L_a$  and flexural rigidity  $EI_a$ . The experiment packages have masses  $M_1, M_3$  and inertias about their hinge point of  $I_1, I_3$ . The distances from the hinge point to the experiment package mass centers are  $L_1, L_3$ . The experiment packages and their connecting arms are assumed to be rigid.

The solar panels are represented by  $M_4, I_4, M_6, I_6$  ( $M_4 = M_6, I_4 = I_6$ ). The masses  $M_4$  and  $M_6$  are connected to the central bus by massless beams of length  $L_b$  and flexural rigidity  $EI_b$ .

### B. PARAMETER VALUES AND NATURAL FREQUENCIES

Table 2-1 lists two sets of parameter values used for simulation purposes. Parameters for the bus and solar panels are similar to those of Appendix B. Parameters for the experiment packages approximate those of SIRT<sup>\*</sup>. As can be seen from Table 2-1, the two data sets are identical except for the length of the platform arms.

\* Shuttle Infrared Telescope Facility (See Aviation Week, Sept. 15, 1980).

Table 2-2 lists the natural frequencies for the 6 elastic modes of the model. The primary difference between set 1 and set 2 is the change in frequency of the platform arm modes which results from shortening the arms per Table 2-1.

### C. MODE SHAPES

The mode shapes for the 5 rigid body modes and first 4 elastic modes are sketched in Fig. 2-2 and Fig. 2-3. These mode shapes do not change qualitatively for the different data sets.

Numerical values for the first 9 mode shapes for the parameters of Table 2-1, set 1, are given in Table 2-3 for the coordinates of interest ( $\theta_1, \theta_2, \theta_3, \gamma_1, \gamma_3$ ). These coordinates are associated with actuation and/or sensing. The center of mass for the solar panels ( $M_4, M_5, M_6$ ) and platform arms ( $M_1, M_2, M_3, M_1, M_3$ ) has been appended to each mode shape. Note that these mass centers are not associated with any physical point of the structure.

The rigid body mode shapes of Fig. 2-2 and Table 2-3 are more complicated than they need to be. For this reason, the technique developed in Appendix E was applied to obtain more pleasing shapes. The resulting shapes are presented in Fig. 2-4 and Table 2-5.

In order to obtain the rigid body shapes the following steps were used. First it was desired to eliminate translation of the solar panel center of mass from all but one mode. The computer algorithm selected the mode shape with the largest value of solar panel center of mass translation (mode 3 of Table 2-3) and using this mode shape as described in Appendix E it eliminated this coordinate from modes 1, 2, 4, and 5. This resulted in five new mode shapes.

Next the algorithm was told to eliminate the arm center of mass translation from all but one of the modes 1, 2, 4, or 5. Mode 1 was selected and four new mode shapes found.

Next, the algorithm was told to eliminate the bus rotation angle ( $\theta_2$ ) from all but one of the modes 2, 4, or 5. Mode 5 was selected and three new mode shapes were found.

Finally, the algorithm was told to eliminate the experiment rotation angle ( $\gamma_1$ ) from all but one of the modes 2 or 4. Mode 4 was selected and two new mode shapes resulted.

It should be noted that if a different set of coordinates or a different ordering had been selected, then different rigid body mode shapes may have resulted. The reason for selecting the mass center coordinates will be more clear when controllability/observability issues are discussed later in this section.

#### D. CONTROLLABILITY

The controllability of various modes can be seen as follows:  
The equations of motion for the platform are

$$M\ddot{x} + D\dot{x} + Kx = Bu$$

where

$M$ ,  $D$  and  $K$  =

mass, damping, and stiffness matrices for the structure, respectively.

$x$  = physical coordinate vector (dimension  $n$ )

$u$  = control vector (dimension  $m$ )

$B$  = control distribution matrix ( $n \times m$ )

In modal coordinates this equation becomes

$$\ddot{q} + \phi^T D \phi \dot{q} + \Lambda^2 q = \phi^T Bu$$

where  $\phi$  (the modal matrix) satisfies

$$x = \phi q$$

$$\phi^T M \phi = I_n$$

$$\phi^T K \phi = \Lambda^2 = \text{diag.} (\lambda_1^2, \lambda_2^2, \dots, \lambda_n^2)$$

$$\lambda_i = i^{\text{th}} \text{ natural frequency}$$

If we assume modal damping, then  $\phi^T D \phi = \hat{D}$  is diagonal. Hence, we see that the matrix product  $\phi^T B$  determines the ability of the control  $u$  to influence the modal dynamics.

The control forces (torques) applied to the platform are given by

$$F = Bu$$

where

$$u = [T_2 \ T_1 \ T_3]^T$$

= actuator torque vector ( $T_2$  is central bus torque,  $T_1$  and  $T_3$  are experiment torques)

$$B = \begin{bmatrix} 0 & 0 & 0 \\ 0 & 0 & 0 \\ 0 & 0 & 0 \\ 0 & -4.8E4 & 0 \\ 0 & 0 & -4.8E4 \\ 2.07E6 & 0 & 0 \\ 0 & 0 & 0 \\ 0 & 0 & 0 \\ 0 & 0 & 0 \\ 0 & 4.8E4 & 0 \\ 0 & 0 & 4.8E4 \end{bmatrix}$$

= Control distribution matrix

Notice that B includes torque scaling for each actuator. Notice also that the actuators which articulate the experiment systems ( $T_1$  and  $T_3$ ) apply a torque to the experiments and an equal and opposite torque to the platform arms at the point of attachment.

Table 2-6 gives the matrix product  $\phi^T B$  for the eigenvectors of Tables 2-4 and 2-5. Here, only the first 9 modes of  $\phi$  are included, so that  $\phi^T B$  is a 9 x 3 matrix.

We can determine the ability of an actuator to influence each mode directly from the elements of  $\phi^T B$ . For example, mode 1 (arm translation), mode 3 (solar panel translation), and mode 6 (solar panel symmetric bending) cannot be influenced by any of the three torque actuators and hence these modes are uncontrollable. Modes 4 and 8 can be influenced by  $T_1$  and  $T_3$  but not  $T_2$ .

It should be noted that for distinct eigenvalues, the ability of a force to influence a mode implies controllability of that mode (see Ref. 2-1). For modes associated with repeated eigenvalues, however, this is not the case. Since there are five rigid body modes, then at least five actuators are required to provide controllability of these modes. Clearly torque actuators cannot move the spacecraft mass center, so any mode shape having a spacecraft mass translation is not controllable. In Table 2-3 all of the rigid body modes have mass center translation. In Table 2-5 only modes 1 and 3 have CM translation, so that modes 2, 4, and 5 form a controllable subset of rigid body modes and modes 1 and 3 form an uncontrollable subset.

#### E. OBSERVABILITY

The sensors we will consider measure positions and rates of  $\theta_2$ ,  $\gamma_1$ , and  $\gamma_3$ . Since we have

$$x = \Phi q$$

the outputs are  $y = Cx$  where

$$x = [v_1 \ v_2 \ v_3 \ \theta_1 \ \theta_3 \ \theta_2 \ v_4 \ v_5 \ v_6 \ \gamma_1 \ \gamma_3]^T$$

$$C = \begin{bmatrix} 0 & 0 & 0 & 0 & 0 & 1 & 0 & 0 & 0 & 0 & 0 \\ 0 & 0 & 0 & 0 & 0 & 0 & 0 & 0 & 0 & 1 & 0 \\ 0 & 0 & 0 & 0 & 0 & 0 & 0 & 0 & 0 & 0 & 1 \end{bmatrix}$$

Now

$$y = Cx = C\Phi q$$

so  $C\Phi$  determines the influence of a given mode on the sensor outputs. Table 2-7 gives  $C\Phi$  for the eigenvectors of Tables 2-4 and 2-5.

From Table 2-7 we see that modes 1, 3, and 6 do not influence the system outputs, and hence are unobservable. A comparison of Table 2-7 with Table 2-6 shows that actuator and sensor influence results are the same (e.g. if  $\phi_1$  is influenced by  $T_1$ , then it influences the sensor output in  $\gamma_1$ . Similarly for  $T_2$  and  $\theta_2$ , and for  $T_3$  and  $\gamma_3$ ).



For distinct eigenvalues, the ability of a mode to influence a sensor output implies observability of that mode. For repeated eigenvalues, however, this is not the case. A minimum of five sensors would be required for observability of the rigid body modes of Table 2-3 or Table 2-5. The three rotation sensors have no capability to sense translation of either the platform arms or the solar panels. In Table 2-5 modes 2, 4, and 5 form an observable subset of rigid body modes, and modes 1 and 3 form an unobservable subset.

Since modes 1, 3, and 6 are neither influenced by the actuators, nor do they influence the sensor outputs we may eliminate them from further consideration in control system design.

Table 2-1. Parameter Values

<u>Parameter</u>	<u>Set 1</u>	<u>Set 2</u>
<u>Platform Arms</u>		
$L_a$ (m)	15	6
$EI_a$ ( $N\text{-m}^2 \times 10^6$ )	20	20
$M_1$ ( $kg \times 10^3$ )	0.3	same
$M_2$ ( $kg \times 10^3$ )	6.0	"
$M_3$ ( $kg \times 10^3$ )	0.3	"
$I_1$ ( $kg\text{-m}^2 \times 10^3$ )	0.1	"
$I_2$ ( $kg\text{-m}^2 \times 10^3$ )	50.0	"
$I_3$ ( $kg\text{-m}^2 \times 10^3$ )	0.1	"
<u>Solar Panels</u>		
$L_b$ (m)	20.0	same
$EI_b$ ( $N\text{-m}^2 \times 10^6$ )	0.1	"
$M_4$ ( $kg \times 10^3$ )	0.5	"
$M_5$ ( $kg \times 10^3$ )	6.0	"
$M_6$ ( $kg \times 10^3$ )	0.5	"
$I_5$ ( $kg\text{-m}^2 \times 10^3$ )	included in $I_2$	"
<u>Experiment Packages</u>		
$L_{e1}$ (m)	3.6	same
$L_{e3}$ (m)	3.6	"
$M_{e1}$ ( $kg \times 10^3$ )	3.3	"
$M_{e3}$ ( $kg \times 10^3$ )	3.3	"
$I_{e1}$ ( $kg\text{-m}^2 \times 10^3$ )	48.0	"
$I_{e3}$ ( $kg\text{-m}^2 \times 10^3$ )	48.0	"

Table 2-2. Natural Frequencies for the LSST Reference Platform

Mode	Set 1 <sup>(1)</sup>		Set 2 <sup>(2)</sup>	
	(Hz)	(rad/s)	(Hz)	(rad/s)
<u>Rigid Body Modes</u>				
1-5	0	0	0	0
<u>Solar Panel Mode</u>				
6 (1st symmetric)	.0471	.296	.0471	.296
7 (1st antisymmetric)	.0639	.401	.0984	.618
<u>Platform Arm Modes</u>				
8 (1st symmetric)	.912	5.73	3.59	22.5
9 (1st antisymmetric)	2.18	13.7	4.54	28.5
10 (2nd symmetric)	36.8	231.	58.4	367.
11 (2nd antisymmetric)	36.8	231.	58.5	367.
(1) Platform arm length = 15 m				
(2) Platform arm length = 6 m				

Table 2-3. Rigid Body Mode Shapes Before Reshaping

Coordinate	RIGID BODY MODES				
	1	2	3	4	5
$\theta_1$	1.49 E-4	1.23 E-5	-8.57 E-10	7.23 E-6	1.15 E-3
$\theta_3$	1.49 E-4	1.23 E-5	-8.57 E-10	7.23 E-6	1.15 E-3
$\theta_2$	1.49 E-4	1.23 E-5	-8.57 E-10	7.23 E-6	1.15 E-3
$Y_1$	2.46 E-3	-3.46 E-3	2.11 E-7	-2.92 E-3	-4.59 E-3
$Y_3$	-3.58 E-3	-3.08 E-3	3.82 E-7	3.24 E-3	-3.85 E-3
CM (S.P.)	-4.20 E-11	1.06 E-6	1.20 E-2	-3.99 E-7	-3.22 E-13
CM (ARMS)	6.14 E-3	3.30 E-4	1.74 E-7	6.10 E-3	-8.38 E-4

Table 2-4. Elastic Mode Shapes

Coordinate	ELASTIC MODES			
	6	7	8	9
$\theta_1$	3.28 E-18	1.25 E-3	-3.04 E-3	3.12 E-3
$\theta_3$	2.97 E-18	1.25 E-3	3.04 E-3	3.12 E-3
$\theta_2$	3.03 E-13	1.24 E-3	3.01 E-11	-4.14 E-3
$Y_1$	-2.90 E-16	-4.62 E-3	6.16 E-3	-2.57 E-3
$Y_3$	-1.01 E-17	-4.62 E-3	-6.16 E-3	-2.57 E-3
CM (S.P.)	-4.99 E-11	4.84 E-17	-8.56 E-19	2.29 E-20
CM (ARMS)	2.44 E-16	-2.36 E-9	-2.13 E-11	-3.53 E-11

Table 2-5. Rigid Body Mode Shapes After Reshaping

Coordinate	RIGID BODY MODES				
	1	2	3	4	5
$\theta_1$	3.28 E-10	-5.28 E-12	1.66 E-15	1.01 E-11	1.16 E-3
$\theta_3$	3.68 E-10	1.85 E-11	1.67 E-15	-2.25 E-11	1.16 E-3
$\theta_2$	3.38 E-10	3.24 E-14	1.67 E-15	1.01 E-15	1.16 E-3
$\gamma_1$	-1.21 E-9	-2.10 E-11	-5.28 E-14	-5.40 E-3	-4.30 E-3
$\gamma_3$	-1.34 E-9	-5.18 E-3	4.53 E-14	1.55 E-3	-4.30 E-3
CM (S.P.)	-2.38 E-15	2.37 E-15	1.20 E-2	-1.24 E-15	-1.13 E-17
CM (ARMS)	8.70 E-3	-1.52 E-11	-1.88 E-13	2.02 E-11	-1.20 E-11

Table 2-6.  $\phi^T B$  for the Eigenvectors of Tables 2-4 and 2-5

Mode	$T_2$	$T_1$	$T_3$
1	0	0	0
2	0	0	-2.48 E2
3	0	0	0
4	0	-2.59 E2	7.43 E1
5	2.39 E3	-2.62 E2	-2.63 E2
6	0	0	0
7	2.56 E3	-2.81 E2	-2.81 E2
8	0	4.42 E2	-4.42 E2
9	-8.56 E3	-2.73 E2	-2.73 E2

Table 2-7.  $C\phi$  for Eigenvectors of Tables 2-4 and 2-5

Coordinate	MODE								
	1	2	3	4	5	6	7	8	9
2	0	0	0	0	1.16E-3	0	1.24E-3	0	-4.14E-3
1	0	0	0	-5.40E-3	-4.29E-3	0	-4.61E-3	6.16E-3	-2.57E-3
3	0	-5.18E-3	0	1.55E-3	-4.29E-3	0	-4.61E-3	-6.16E-3	-2.57E-3

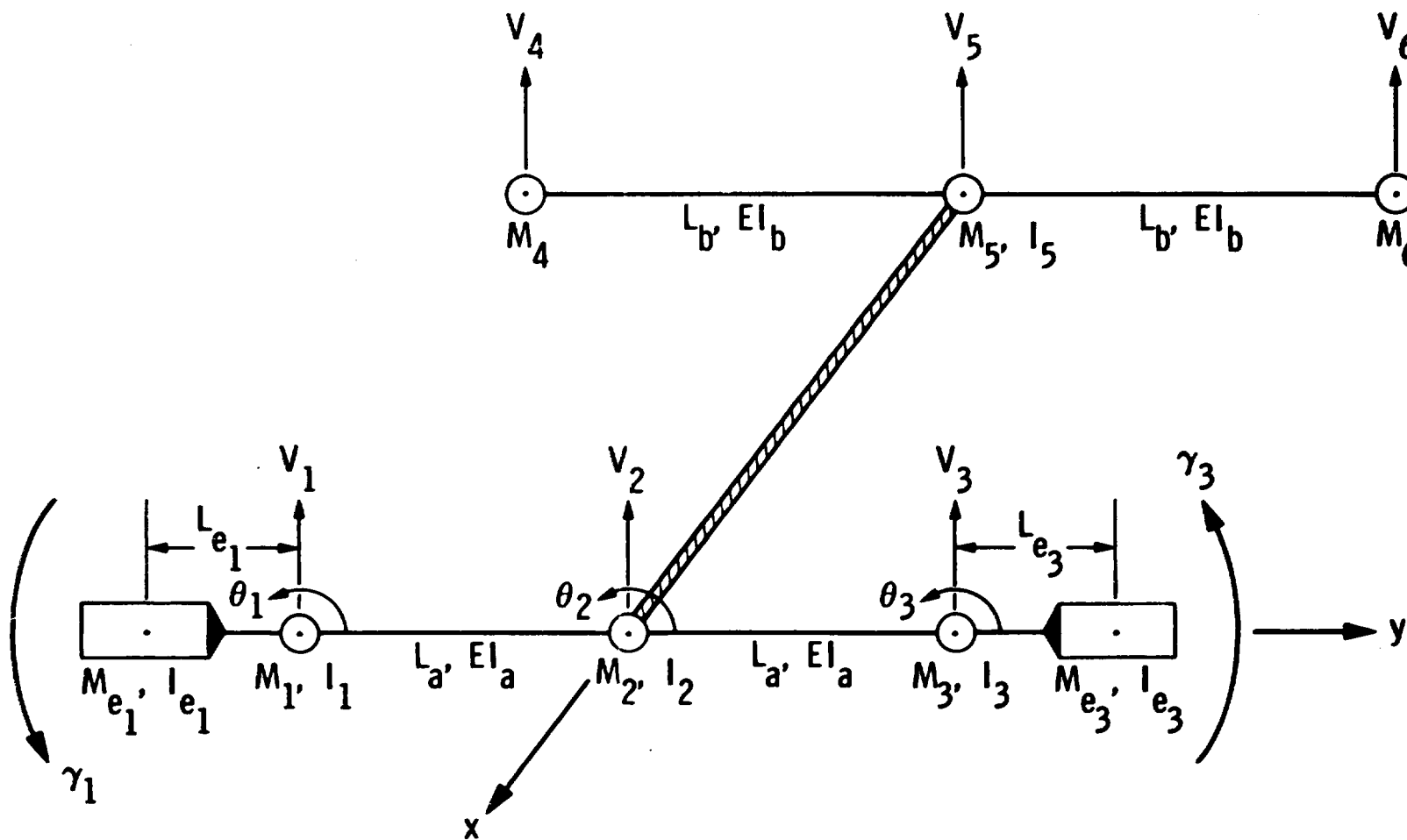
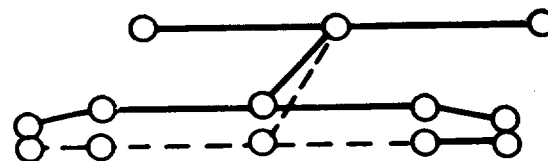
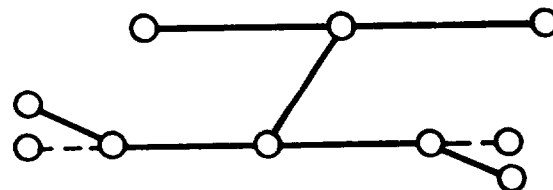


Fig. 2-1. LSST Reference Platform Model

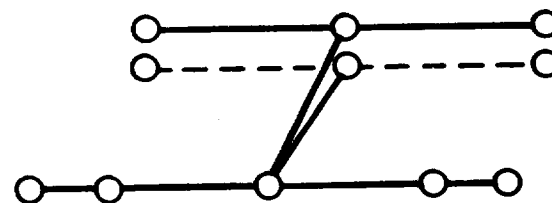
MODE 1: ARM TRANSLATION



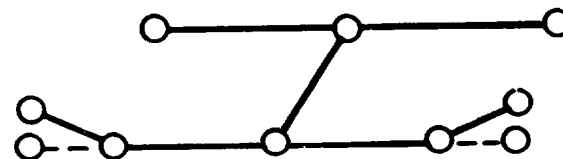
MODE 2: EXPERIMENT ROTATION, ANTISYMMETRIC



MODE 3: SOLAR PANEL TRANSLATION



MODE 4: EXPERIMENT ROTATION, SYMMETRIC



MODE 5: BUS ROTATION

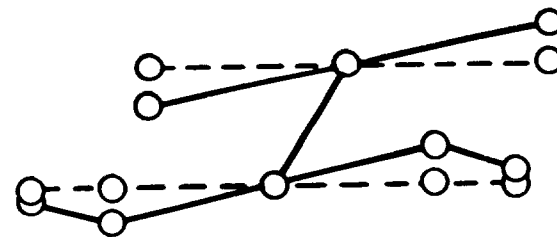
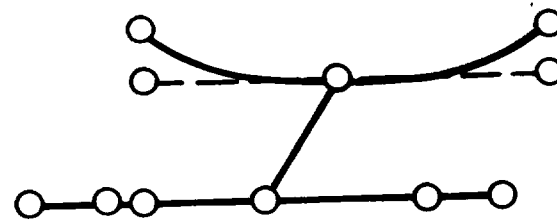
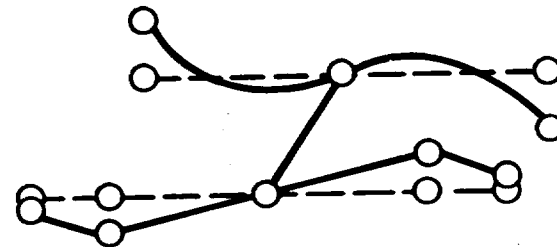


Fig. 2-2. Rigid Body Modes Before Reshaping

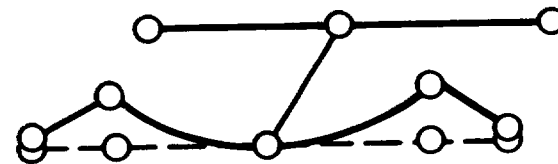
MODE 6: SOLAR PANEL, SYMMETRIC



MODE 7: SOLAR PANEL, ANTISYMMETRIC



MODE 8: ARM, SYMMETRIC



MODE 9: ARM, ANTISYMMETRIC

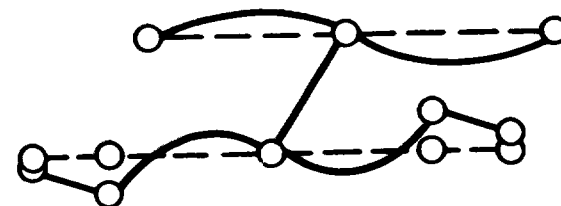
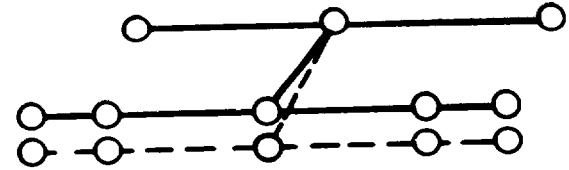


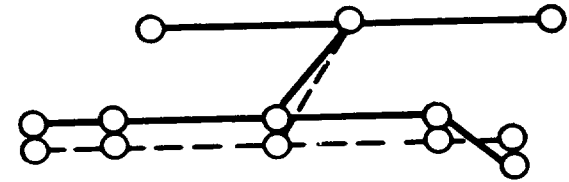
Fig. 2-3. First Four Elastic Modes



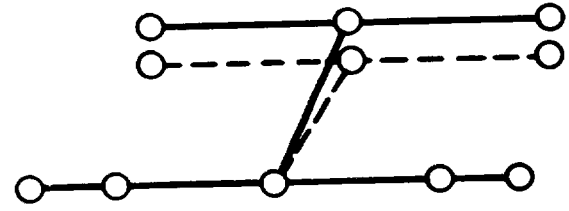
MODE 1: ARM TRANSLATION



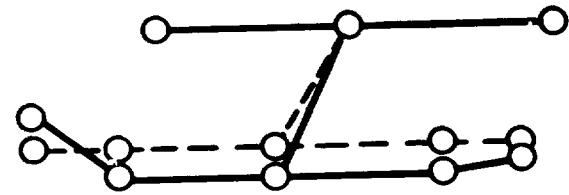
MODE 2: EXPERIMENT ROTATION



MODE 3: SOLAR PANEL TRANSLATION



MODE 4: EXPERIMENT ROTATION



MODE 5: BUS ROTATION

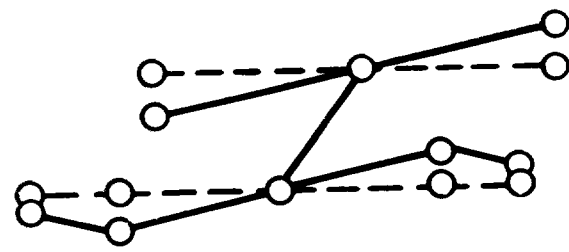


Fig. 2-4. Rigid Body Modes After Reshaping

### III. CONTROL SYSTEM REQUIREMENTS

This section gives a brief statement of the controls, objectives, and requirements for the platform.

#### A. OVERVIEW

There are many requirements which attitude control systems for the LSST Platform have to satisfy. These include a capability for:

- (1) stabilization and initial acquisition of celestial references
- (2) maintaining a prescribed attitude in the presence of various disturbance inputs
- (3) experiment pointing control
- (4) reorienting the gross pointing direction to obtain a new viewing configuration or for reboost
- (5) reboost (or station keeping) to maintain a specified orbit

Of these five requirements, only the second and third will be addressed in what follows.

#### B. STABILITY REQUIREMENTS

Requirements for attitude control include both accuracy and stability. In this report we shall limit ourselves to a consideration of stability. In addition to pointing stability we will also consider linear acceleration levels, since some experiments (e.g. material processing experiments) are concerned with these.

Table 3-1 lists requirements for pointing stability and acceleration levels for some of the more stringent missions being considered for the platform. Pointing stabilities in the range of .01 to 1 arc sec will almost certainly require sophisticated pointing systems. The shuttle infrared telescope facility has pointing requirements in this range (.1 arc sec).

Pointing stabilities in the range of 10 to 1000 arc sec will require less sophisticated pointing systems. In this range many users would prefer

the basic platform control system to meet their stability requirements. The cryogenically cooled telescope has pointing requirements in this range (30 arc sec).

Pointing stability requirements below .01 arc sec will probably require image motion compensation. This problem will not be addressed in this report. There are a number of users with pointing requirements between 1 and 10 arc seconds. Most probably they will require pointing systems although there are some users that would like the basic platform to provide this pointing capability. The high energy gamma telescope has pointing requirements in this range (6 arc sec).

Table 3-1. Platform Requirements

Requirement	Specification
pointing system stability	.05 to 5 $\mu$ rad (.01 to 1 arc sec)
platform stability	.05 to 5 mrad (10 to 1000 arc sec)
platform acceleration	.1 to 10 $\text{mm/s}^2$ ( $10^{-5}$ to $10^{-3}$ g)

#### IV. CONTROL SYSTEM DESIGN

This section documents control system design for the LSST Reference Platform of section II. The purpose of this design effort was to obtain some simple control system designs which would be suitable for identifying the major control problems associated with the LSST reference platform. No attempt has been made here to obtain designs having optimal performance in any sense. Classical frequency design techniques are used based on simplified rigid body models of the platform. Rate plus position feedback controllers are used with ideal actuators and sensors assumed. The bus and experiment package controllers are designed independently. Before beginning the control system design, several control concepts are discussed.

##### A. CONTROL CONCEPTS

Three control concepts for the LSST platform will be discussed in what follows. The first technique is the simplest conceptually and provides independent control for the bus structure and experiment packages. The second scheme allows for limited one-way information exchange between the bus and experiment package control systems. The final concept provides limited, or unlimited two-way information exchange between control systems.

##### 1. Independent Control

Figure 4-1 illustrates the various control schemes symbolically. Only two experiment packages are illustrated, but in actuality there could be many more. Independent control is the simplest conceptually. Here, each control system operates independently using its own set of sensors and actuators.

##### 2. One-Way Interface

With the one-way interface scheme the central bus can send information to each experiment package. In this case the bus controller operates independently, but the experiment package controllers take into account the data from the central bus structure in some way so as to improve pointing accuracy.

The one-way interface scheme could also be implemented in the other direction. That is, each experiment control system could send the bus controller information which would help it to minimize the effects of disturbance inputs introduced by that experiment package. This might be as simple as a status bit indicating whether or not the experiment control actuators are torquing, or, it could be a more complete information exchange. With this scheme the experiment package control systems would operate independently, but the bus controller would not be totally independent. This one-way interface approach would make the bus controller design dependent on varying experiment package designs and as such may not be very practical.

### 3. Two-Way Interface

This method gives each control system access to information available to the other control systems. This might be a partial or total information exchange. With this scheme the controllers are all interdependent to some extent. This dependence could be complete, so that in effect there is only one central controller, or it could be less complete allowing more independence of action. As the number of experiment packages increases, this two-way interface could become rather complicated. The two-way interface also makes the bus controller design dependent on the various experiment package designs and as such may not be very practical.

### 4. Sensors and Actuators

As a minimum we assume that each experiment package has some means of torquing to maintain its desired orientation. A two-axis (e.g. azimuth, elevation angle) torquing capability might be typical. In addition, each package may or may not have its own (angular) position and rate sensors. If an experiment package has position sensors, it may or may not have the ability to directly measure target position.

The bus controller will have a torquing capability plus position and rate sensors. As a minimum, sensors and actuators will be located

on the central bus structure, but additional actuators and sensors could be located on the flexible portion of the structure if necessary to obtain the desired performance.

The information exchange, then, can be one in which sensor and actuator information is exchanged, and/or one in which estimated state vector information is exchanged.

### 5. Design Approach

The approach to designing a control system for the LSST platform should be in the order of conceptual complexity. First the independent controls approach, then the one-way interface. The two-way interface may or may not be a viable alternative and should be attempted only as a last resort. In fact any scheme which makes the bus controller dependent on the various experiment packages would be an operational nightmare and should be avoided if at all possible.

The bus controller should be attempted first with all actuators and sensors on the rigid central structure. However, if performance improvement is needed, the location of sensors on portions of the flexible structure might be considered. Location of actuators on the flexible structure is much more difficult and should be attempted only if other approaches fail to provide the required performance.

The remainder of this report considers only the simplest design approach, that being independent control systems for the central bus and each experiment. It will be assumed that each control system has its own torquers and its own position and rate sensors. All sensors will measure inertial position and rate.

#### B. BUS CONTROLLER DESIGN

A block diagram for the bus controller is shown in Fig. 4-2. Symbols in Fig. 4-2 are defined as follows

$\theta_c$  = Commanded bus angle (nominally zero)

$\theta$  = Actual bus angle (relative to some inertial coordinate system)

$T$  = Torque applied to bus by controller

$T_d$  = Disturbance Torque applied to bus

$J$  = Platform inertia

$\hat{J}$  = Torquer gain (an estimate of  $J$ )

$K_p$  = Position gain

$K_r$  = Rate gain

In Fig. 4-3 the block diagram has been redrawn in a format convenient for controller design purposes. Here  $K_r/K_p$  is the rate to position gain also called  $K_{rp}$  in what follows.

The forward loop transfer function from Fig. 4-3 is

$$G(s) = \frac{K_p \hat{J}}{J s^2}$$

The feedback loop transfer function is

$$H(s) = K_{rp} s + 1$$

From this the closed loop transfer function is

$$\begin{aligned} \frac{\theta}{\theta_c}(s) &= \frac{G(s)}{1+G(s)H(s)} \\ &= \frac{K_p \hat{J}}{J s^2 + K_p \hat{J} K_{rp} s + K_p \hat{J}} \end{aligned}$$

$$\text{or } \frac{\theta}{\theta_c}(s) = \frac{K_p \hat{J}/J}{s^2 + (K_p K_{rp} \hat{J}/J) s + K_p \hat{J}/J} .$$

Now if  $\hat{J} = J$  then we have

$$\frac{\theta}{\theta_c}(s) = \frac{K_p}{s^2 + K_{rp} s + K_p}$$

The characteristic equation for the system is then

$$s^2 + K_{rp} s + K_p = 0$$

Next define the damping and natural frequency as  $\zeta$  and  $\omega_n$  respectively,

so that

$$\omega_n^2 = K_p$$

$$2\zeta\omega_n = K_{rp}$$

From this we can determine  $K_p$  and  $K_{rp}$  given desired values for  $\omega_n$  and  $\zeta$

$$K_p = \omega_n^2 \tag{4-1}$$

$$K_r = 2\zeta\omega_n \tag{4-2}$$

$$K_{rp} = 2\zeta/\omega_n \tag{4-3}$$

Or, given  $K_p$  and  $K_{rp}$  we can determine  $\zeta$  and  $\omega_n$

$$\omega_n = \sqrt{K_p}$$

$$\zeta = \frac{1}{2} \sqrt{K_p} K_{rp}$$

$$= \frac{1}{2} K_r / \sqrt{K_p}$$

$$= \frac{1}{2} \omega_n K_{rp}$$

For the purposes of this design, we will choose

$$\omega_n = 0.01 \text{ Hz}$$

$$= 0.0628 \text{ rad/s}$$

$$\zeta = 0.707$$



then

$$K_p = \omega_n^2 = 3.94E-3 \text{ rad/s}^2$$

$$K_r = 88.6E-3 \text{ rad/s}$$

$$K_{rp} = 22.5 \text{ s}$$

To complete the controller design we must have a value for  $\hat{J}$ . Figure 2-1 shows a sketch of the platform model. It is not immediately obvious how to calculate  $\hat{J}$ , because of the hinged experiment packages. Suppose, however, that we assume that the experiment pointing angles ( $\gamma_1$  and  $\gamma_3$ ) remain zero. This is equivalent to saying that the commanded (inertial) pointing angles are zero for  $\gamma_1$  and  $\gamma_3$ , and that the experiment controllers are functioning ideally. Then so far as the bus controller is concerned the mass of the experiment  $M_{e1}$  can be lumped with the platform mass  $M_1$ ,\* and similarly with  $M_{e3}$  and  $M_3$ . Then  $\hat{J}$  can be calculated as follows

$$\hat{J} = (M_1 + M_{e1} + M_3 + M_{e3})(L_a)^2 + (M_4 + M_6)(L_6)^2 + I_2 + I_5$$

Then for the parameters of Table 2-1, set 1, we have

$$\begin{aligned} \hat{J} &= (0.3 + 3.3 + 0.3 + 3.3)E3 (15)^2 \\ &+ (0.5 + 0.5)E3 (20)^2 + 50E3 \\ &= 2.07E6 \text{ kg-m}^2 \end{aligned}$$

For Table 2-1, set 2 data we have

$$\begin{aligned} \hat{J} &= 7.2E3 (6)^2 + 1.0E3 (20)^2 + 50E3 \\ &= 0.709E6 \text{ kg-m}^2 \end{aligned}$$

This completes the bus controller design.

### C. EXPERIMENT CONTROLLER DESIGN

A block diagram for the experiment controllers is shown in Fig. 4-4. This figure is identical to Fig. 4-2 except for the additional commanded

\*The inertia of the experiment about its hinge point need not be included since we assume that the experiment does not rotate relative to an inertial reference frame.

inputs  $T_c$  and  $\dot{\gamma}_c$ .  $T_c$  and  $\dot{\gamma}_c$  are the commanded torque and rate respectively.

For the experiment controllers we will choose two values for the natural frequency:

$$\omega_n = 1 \text{ Hz} = 6.28 \text{ rad/s}$$

and

$$\omega_n = 0.1 \text{ Hz} = 0.628 \text{ rad/s}$$

In each case we will select  $\zeta = 0.707$ .

Now using Eqs. 4-1 through 4-3 we can compute the gains  $K_p$ ,  $K_r$ , and  $K_{rp}$ . For a 1-Hz controller we have:

$$K_p = \omega_n^2 = 39.4 \text{ rad/s}^2$$

$$K_r = 2\zeta\omega_n = 8.88 \text{ rad/s}$$

$$K_{rp} = 2\zeta/\omega_n = 0.225 \text{ s}$$

For the 0.1-Hz controller we have:

$$K_p = \omega_n^2 = 0.394 \text{ rad/s}^2$$

$$K_r = 2\zeta\omega_n = 0.888 \text{ rad/s}$$

$$K_{rp} = 2\zeta/\omega_n = 2.25 \text{ s}$$

The value for  $\hat{J}$  can be read directly from Table 2-1.

$$\hat{J} = I_{e1} = I_{e3} = 48E3 \text{ kg-m}^2$$

This completes the design of the experiment controllers.

#### D. COMBINED DESIGN

A block diagram for the combined system is shown in Fig. 4-5. The commanded inputs are shown  $\theta_{c2}$  for the bus controller,  $\gamma_{c3}$  for the experiment 3 controller, and  $\gamma_{c1}$ ,  $T_{c1}$  for the experiment 1 controller.\* For the purposes of design evaluation, only the experiment 1 controller has a non-

\*.  $\dot{\gamma}_{c1}$  is not shown on this diagram, because for the simulations conducted,  $\dot{\gamma}_{c1}$  was set to zero. A better design could have been achieved using a nonzero value for  $\dot{\gamma}_{c1}$ , but this was not realized until after all simulations had been completed.

zero commanded input. The success of the control system design is to be measured by how closely the bus and experiment 3 controllers maintain  $\theta_2$  and  $\gamma_3$  near zero in the presence of commanded slews of the experiment 1 controller.

#### E. CLOSED LOOP SYSTEM EIGENVALUES

The open loop eigenvalues for the LSST reference platform are given in Table 2-2. Table 4-1 shows the system gains used for simulation purposes. Figures 4-6 and 4-7 show the associated closed loop eigenvalues for these gain values, (uncontrollable/unobservable modes are not plotted unless noted otherwise).

Figure 4-6, Run F12, shows the closed loop eigenvalues for the 15-m platform arms when open loop torquing is used for experiment 1. Note the 2 closed loop poles at the origin. This is an indication that the rigid body mode associated with experiment 1 becomes uncontrollable when the feedback gains are set to zero. The bus controller frequency and damping are somewhat higher than the design values of .0628 rad/s and .707 damping. Also, the experiment 3 controller frequencies are somewhat higher than the design values, and critically damped. The elastic mode vibration frequencies all have low values of damping.

Figure 4-6, Run F10, shows the closed loop eigenvalues for 15-meter platform arms and 1.0-Hz experiment controllers. Note that the bus damping and frequency is close to the desired values of 0.707 and  $6.28E-2$  rad/s. The experiment control frequencies, however, are critically damped with frequencies of 5.0 and 59.0 rad/s. The elastic mode vibration frequencies (for the controllable modes) all have small values of damping.

Figure 4-6, Run F13, is similar to Run F10 except that the eigenvalues associated with the experiment 3 controller are shifted lower because of the lower gains used.

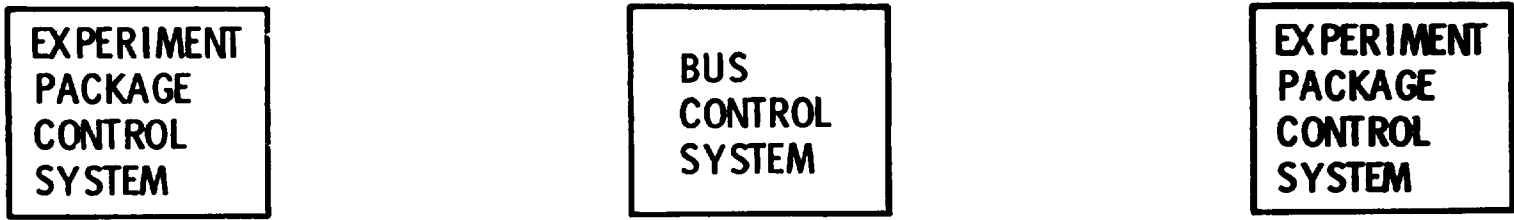
Runs F17 - F19 use the same estimate for the platform inertia ( $J = 2.07E6 \text{ kg-m}^2$ ) as for Runs F12, F10, and F13. The design value of

0.709 kg-m<sup>2</sup> was not used to demonstrate the effect of parameter error on system performance. The results are shown in Fig. 4-7. Note that in all cases closed loop system response remains stable. In fact, damping for the elastic modes of the platform is actually improved over many cases with 15-m platform arms. Based on the results shown in Figs. 4-6 and 4-7, we might say that the design is adequate for the purposes of identifying major control problems, although it is in no way an optimum design.

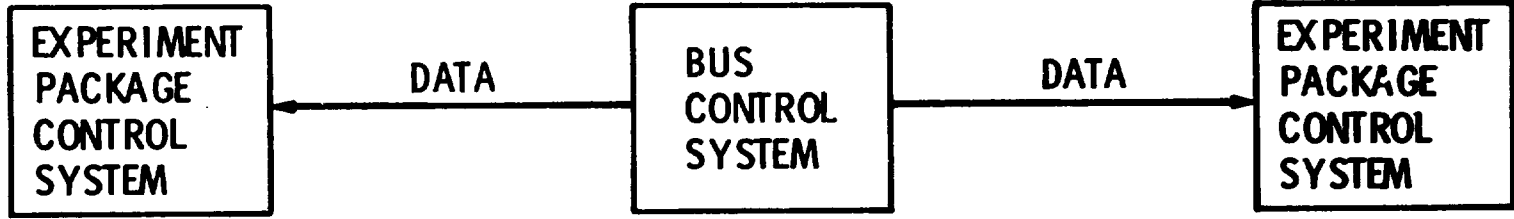
Table 4-1. Control System Gains for Performance Analysis

RUN	ARM LENGTH (m)	CONTROL BANDWIDTH		EXP. 1 GAINS		EXP. 3 GAIN	
		$w_{n1}$ (Hz)	$w_{n2}$ (Hz)	$K_p$ (rad/s <sup>2</sup> )	$K_r$ (rad/s)	$K_p$ (rad/s <sup>2</sup> )	$K_r$ (rad/s)
F12	15	*	1.0	0.0	0.0	39.4	8.88
F10	15	1.0	1.0	39.4	8.88	39.4	8.88
F13	15	1.0	0.1	39.4	8.88	.394	.888
F17	6	*	1.0	0.0	0.0	39.4	8.88
F18	6	1.0	1.0	39.4	8.88	39.4	8.88
F19	6	1.0	0.1	39.4	8.88	.394	.888
ALL RUNS USE THE FOLLOWING DATA: Bus Inertia est. $\hat{J} = 2.07E6 \text{ kg-m}^2$ Exp. 1 and Exp. 2 Inertial est. $J = 48.0E6 \text{ kg-m}^2$ Bus Gains $K_p = 3.94E-3 \text{ rad/s}^2$ $K_r = 88.6E-3 \text{ rad/s}$							
* Open Loop Torquing							

INDEPENDENT CONTROL:



ONE-WAY INTERFACE:



TWO-WAY INTERFACE:

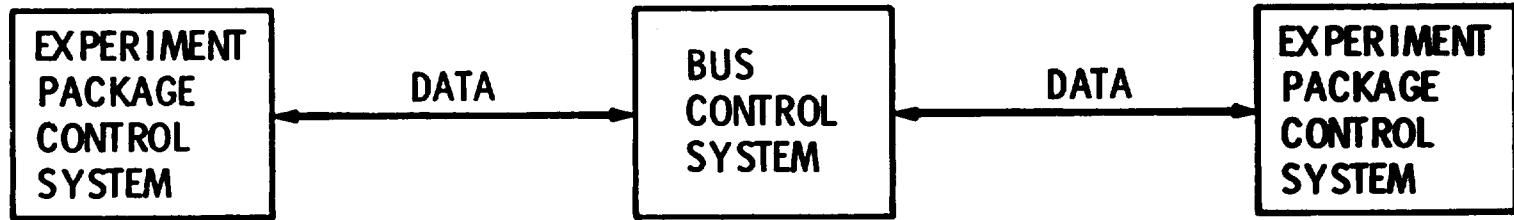


Fig. 4-1. Control Concepts for the LSST Reference Platform

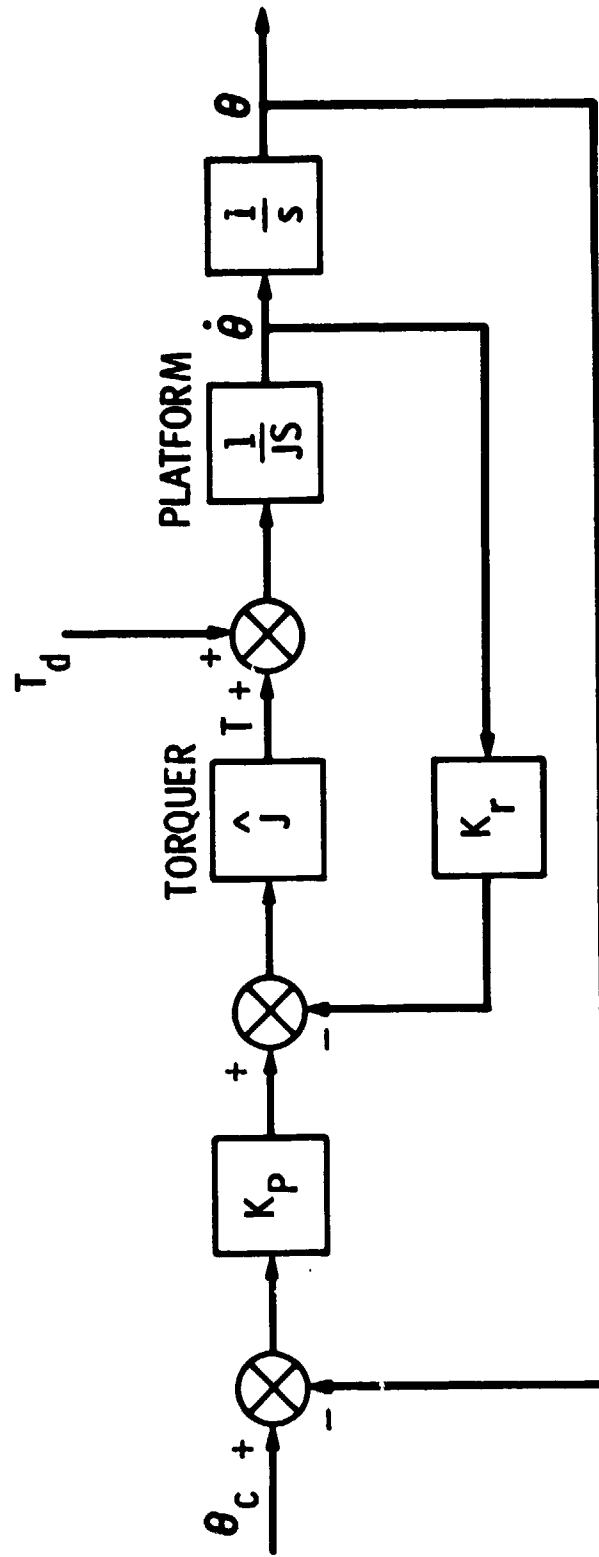


Fig. 4-2. Bus Controller Block Diagram

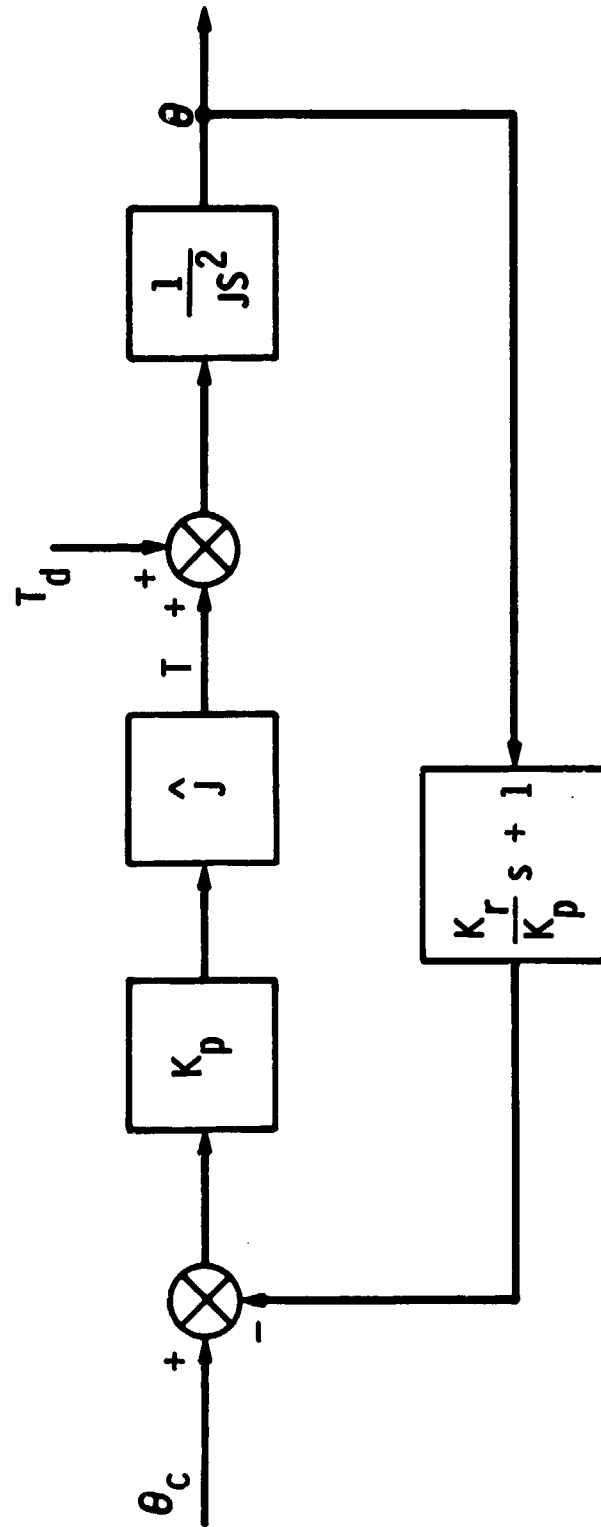


Fig. 4-3. Alternate Bus Controller Block Diagram

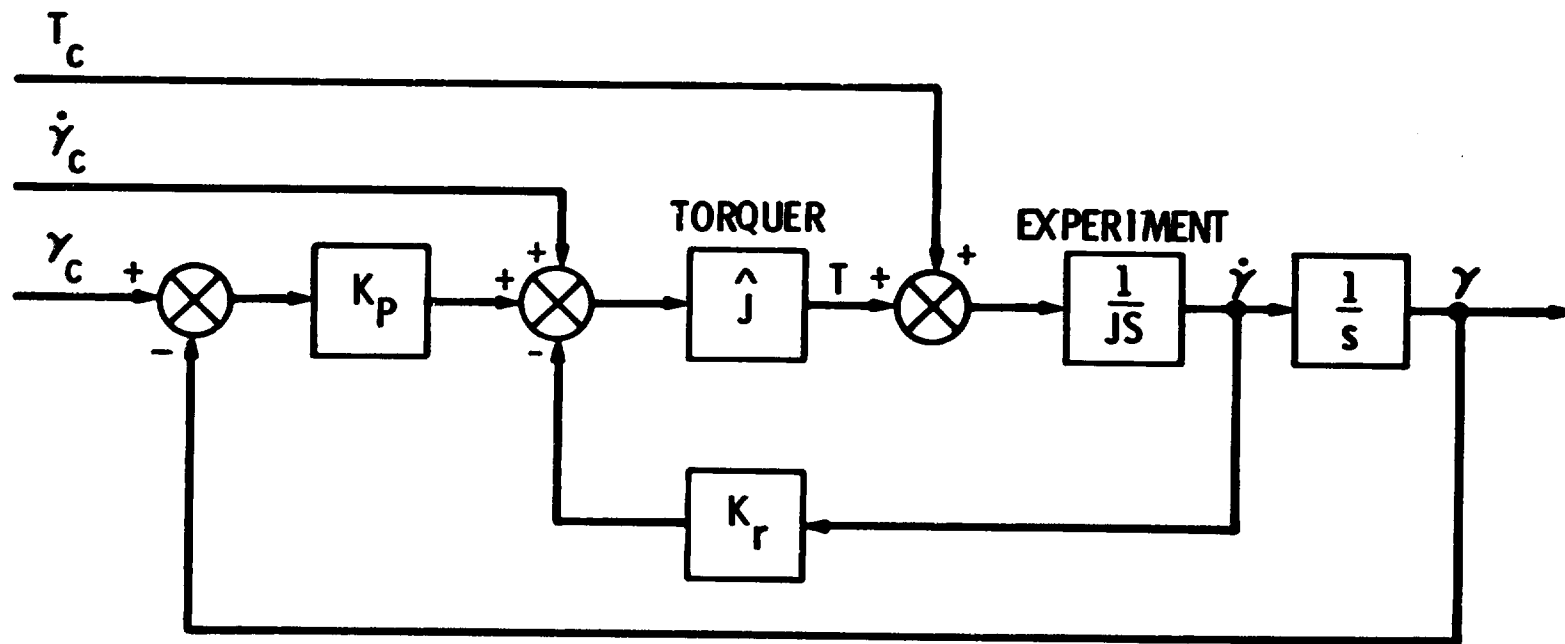


Fig. 4-4. Experiment Controller Block Diagram



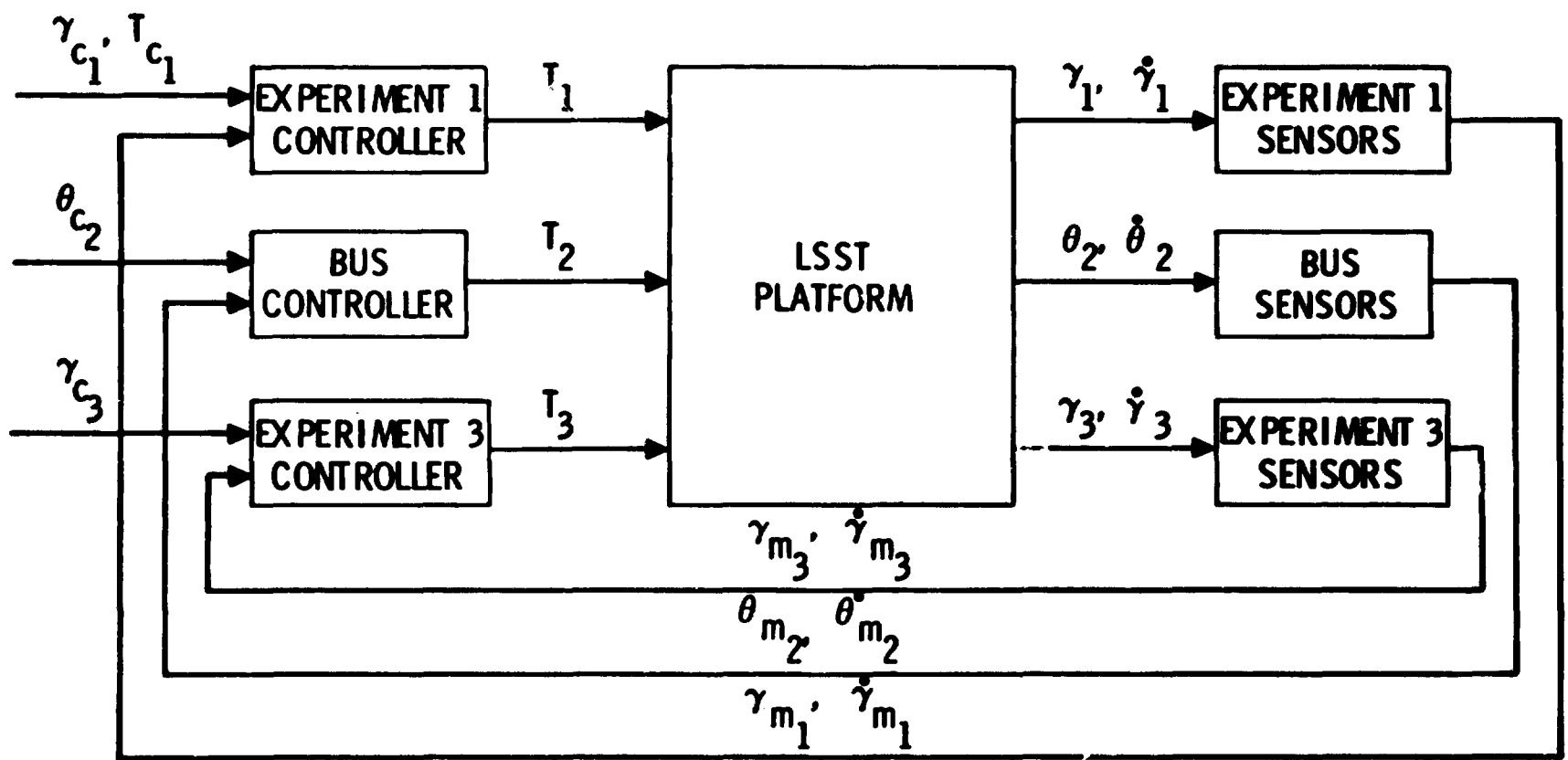


Fig. 4-5. Control System Configuration

ORIGINAL PAGE IS  
OF POOR QUALITY

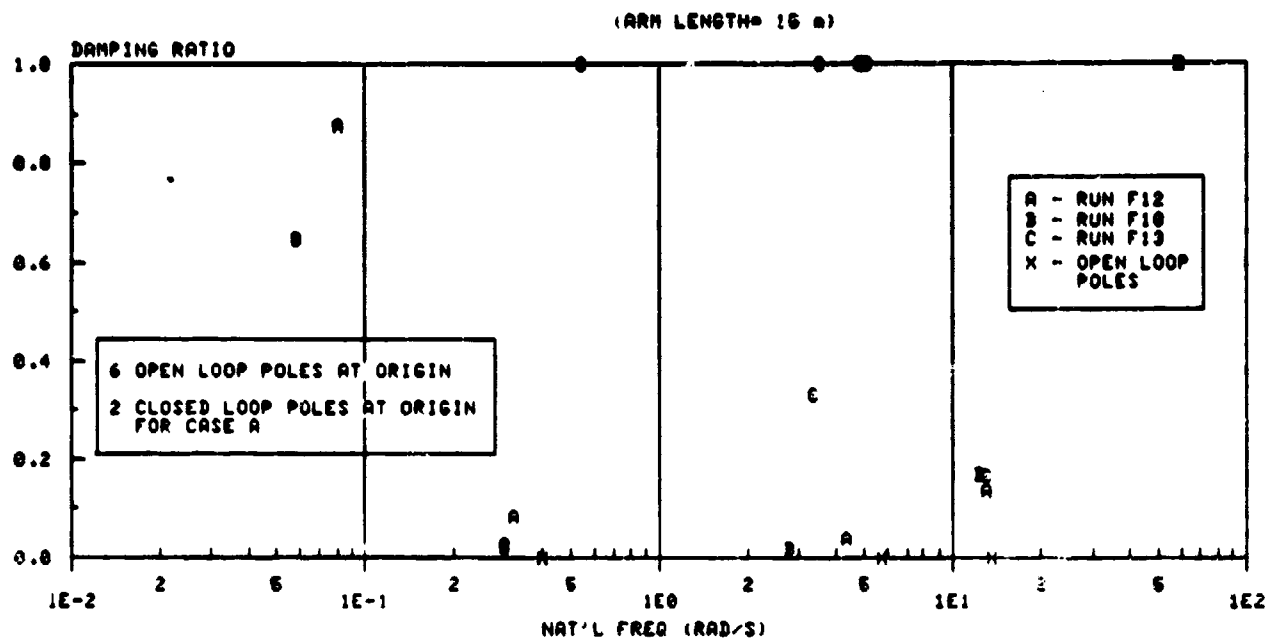


Fig. 4-6. Closed Loop Pole Positions for Data Set 1

ORIGINAL PAGE IS  
OF POOR QUALITY

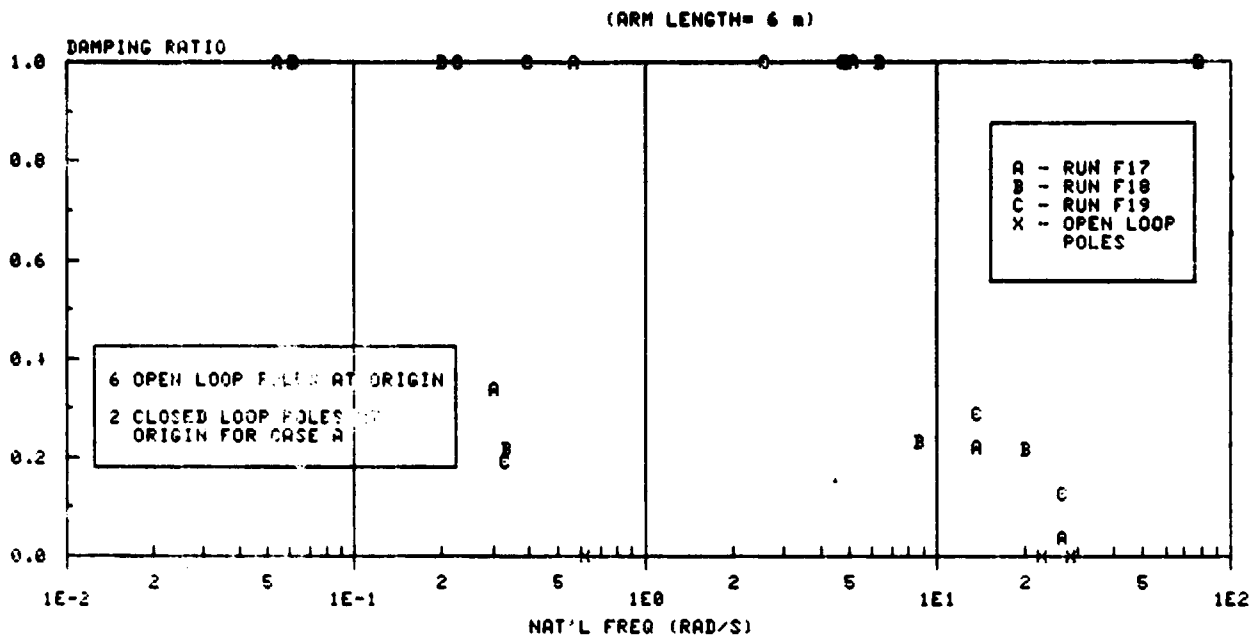


Fig. 4-7. Closed Loop Pole Positions for Data Set 2

## V. CONTROL SYSTEM EVALUATION

In this section the transient response performance of the combined system is examined. Comments are also made on additional factors which can affect performance.

### A. TRANSIENT RESPONSE

Computer simulations were performed to determine system performance. Table 5-1 summarizes the results (for a definition of the symbols used in Table 5-1, see Figs. 2-1 and 4-5). All runs were made with a bus control frequency ( $\omega_{n2}$ ) of 0.01 Hz. The commanded torque ( $T_{cl}$ ) was a square wave input of + 20 N - m, followed by an equal duration -20 N - m input. The commanded torque durations were chosen to give the desired final commanded angle ( $\gamma_{1c}$ ) at the end of the torquing sequence assuming that the base point ( $M_1$ ) was inertially fixed.\* The commanded angle as a time function was taken as the second integral of torque according to Newton's law (again with the assumption that the base point was fixed). The experiment inertias of Table 2-1 were used ( $T_{cl} = I_{e1} \ddot{\gamma}_{cl}$ ).

Table 5-1 presents the peak transient responses for the experiment 3 pointing angle ( $\gamma_3$ ), the bus pointing angle ( $\theta_2$ ) and the bus acceleration ( $\ddot{V}_2$ ). A comparison of Tables 5-1 and 3-1 shows that  $\gamma_3$  exceeds a stability requirement of 5  $\mu$ rad by up to 70 times, and is 60 to 7000 times a 0.05- $\mu$ rad requirement. Acceleration levels are within the 10-mm/s<sup>2</sup> requirement but exceed a 0.1-mm/s<sup>2</sup> requirement by 6 to 30 times.  $\theta_2$  performance is between 2 and 5 mrad (400 to 1000 arc sec). This is within the 5-mrad requirement but 40 to 100 times the 0.05-mrad requirement. From this we see that the pointing requirements of Table 3-1 cannot be easily met using controllers of the type considered here.

A comparison of the six representative simulation runs illustrates several clear trends. It should be kept in mind that experiment 1 is creating the disturbance, and experiment 2 (fixed to the bus) and experiment 3 are feeling the influence of the disturbance. Using a closed loop

---

\* In the simulations, the base point ( $M_1$ ) was not inertially fixed, so that the open loop torque command was in error.

controller for experiment 1 (compare Runs F10 and F12) results in a smoother disturbance torque profile, and as such improves pointing stability for both  $\gamma_3$  and  $\theta_2$ . It also reduces acceleration levels at the bus ( $\ddot{V}_2$ ). Increasing experiment 3 bandwidth (compare Runs F10 and F13) increases  $\gamma_3$  stability, but has an adverse affect on  $\ddot{V}_2$ . Decreasing the arm length (compare Runs F10 and F18) increases pointing stability of both  $\gamma_3$  and  $\theta_2$  and in most cases decreases acceleration level ( $\ddot{V}_2$ ). The reader is referred to Appendix F for time plots of an example simulation (Run F10).

#### B. ADDITIONAL FACTORS WHICH CAN AFFECT PERFORMANCE

There are many factors not considered in this study which could have a major influence on the absolute performance of the LSST reference platform. Imperfect sensors and actuators, gimbal friction and flexibility, and more complex structural dynamics could all result in poorer performance than that presented here. On the other hand improved controller gain selection or more sophisticated controllers could improve the performance results. For example, base motion compensation could be added using an additional sensor for each experiment package (an accelerometer), and image motion compensation could be implemented for some types of experiment packages by the addition of another actuator (a secondary mirror drive for example). For these reasons, the performance results of Table 5-1 should not be taken as absolutes in any sense. Yet Table 5-1 does indicate the difficulty which is faced when attempting to design a control system for a platform of this type.

Table 5-1. Performance Results

RUN	ARM LENGTH (m)	CONTROL BANDWIDTH		PEAK RESPONSE		
		$\frac{W_{n_1}}{\text{(Hz)}}$	$\frac{W_{n_3}}{\text{(Hz)}}$	$\frac{\gamma_3}{\text{(\mu rad)}}$	$\frac{\theta_2}{\text{(mrad)}}$	$\frac{\ddot{V}_2}{\text{(mm/s}^2\text{)}}$
F12	15.0	*	1.0	56.00	5.11	3.000
F10	15.0	1.0	1.0	7.59	3.27	0.964
F13	15.0	1.0	0.1	357.00	3.25	0.608
F17	6.0	*	1.0	12.20	3.10	0.848
F18	6.0	1.0	1.0	3.13	2.28	0.819
F19	6.0	1.0	0.1	254.00	2.26	0.819

\*OPEN LOOP TORQUING:  
 $\gamma_{C_1} = 88 \text{ mrad}$ ,  $T_{C_1} = 20 \text{ N-m}$ ,  $W_{n_2} = 0.01 \text{ Hz}$  for all runs.

## VI. SUMMARY AND FUTURE STUDY

Several control problems for the LSST Reference Platform have been identified and quantified in this report. Perhaps the most important of these is that operation of multiple independent control systems on a single platform presents a major problem when high performance is required. Experiment compatibility will be an important operational consideration. Control system design is complicated by large shifts in structural parameters which occur as a result of variations in the number and location of experiments mounted on the platform. Structural vibration frequencies in the controller bandwidth further complicate the design problem. It has been found that conventional controllers miss performance requirements by a wide margin when these factors are taken into account.

It should be noted that the lighter the platform is, independent of its stiffness, the greater is the controller interaction problem. The best structural design solution, from this standpoint, would be to place the Queen Mary in orbit. This might post other problems, however, from socio-political-economic viewpoints.

It should also be noted that problems with platform flexibility cannot be solved by simply making the platform arms more rigid. As Appendix F illustrates, elastic vibration of the solar panels is the dominant pointing error once the initial slew transient (of experiment 1) has subsided.

Two control approaches have been identified for future study. The first approach is to add additional sensors and/or actuators to individual experiment controllers. Base motion and image motion compensation fall in this category. The second approach is to allow information exchange between controllers, particularly one-way exchange from the bus controller to the experiment controllers. The challenge is to develop controllers which can significantly reduce the controller interaction problem and at the same time reduce controller sensitivity to structural parameter variations.

## APPENDIX A. MODEL FOR PLATFORM WITH FLEXIBLE CROSS ARMS

This Appendix documents the application of standard finite element techniques to modeling the LSST reference platform with experiments rigidly attached to the platform arms. The platform arms are modeled as flexible appendages to a rigid bus. The solar panels are assumed to be rigid. A six-degree-of-freedom model is developed for planar motion of the platform cross arms. The equations of motion are developed using a lumped mass approximation and a consistent mass matrix approach. The double diagonalization procedure for obtaining mode shapes and frequencies is discussed and the effect of parameter variations on mode shapes and frequencies is illustrated.

The purpose of this appendix is to provide a building block to more complete models of the LSST reference platform as developed in Appendices B and C. It is felt that this building block approach to modeling provides increased understanding of the structural model which is useful for controls design work.

### 1. Configuration

Figure A-1 shows the simplified configuration used for modeling of the platform cross arms. Motion is constrained to the plane. The motion of interest for the initial modeling activity will be for rotations about the x axis. These rotations are tightly coupled with displacements along the z axis. For small angles the y axis motion is considered negligible. Hence, the model has six degrees of freedom, the vertical displacements  $V_1, V_2, V_3$  and rotations  $\theta_1, \theta_2, \theta_3$ . The masses  $M_1$  and  $M_3$  (taken to be point masses) and inertias  $I_1$  and  $I_3$  are associated with two rigidly attached science and applications packages. The mass  $M_2$  and inertia  $I_2$  are associated with the central bus. The connecting elements are taken to be beams with length  $L$ , mass per unit length  $m$ , and flexural rigidity  $EI$ .

### 2. Stiffness Matrix

The stiffness matrix for a beam element is the standard one used for finite element techniques (see for example Ref. A-1, p. 158). With reference to Fig. A-2 we have,

$$\begin{bmatrix} F_1 \\ F_2 \\ T_1 \\ T_2 \end{bmatrix} = \frac{2EI}{L^3} \begin{bmatrix} 6 & -6 & 3L & 3L \\ -6 & 6 & -3L & -3L \\ 3L & -3L & 2L^2 & L^2 \\ 3L & -3L & L^2 & 2L^2 \end{bmatrix} \begin{bmatrix} V_1 \\ V_2 \\ \theta_1 \\ \theta_2 \end{bmatrix} \quad (\text{A-1})$$

Here,  $V_1$  and  $V_2$  are the vertical displacements of the beam end points, and  $\theta_1$  and  $\theta_2$  are the rotations at these points (positive slope = positive rotation).  $F_1$ ,  $F_2$  are the corresponding applied forces and  $T_1$ ,  $T_2$  are the applied torques.

Equation (A-1) can also be written

$$\begin{bmatrix} F_1 \\ T_1 \\ F_2 \\ T_2 \end{bmatrix} = \frac{2EI}{L^3} \begin{bmatrix} 6 & 3L & -6 & 3L \\ 3L & 2L^2 & -3L & L^2 \\ -6 & -3L & 6 & -3L \\ 3L & L^2 & -3L & 2L^2 \end{bmatrix} \begin{bmatrix} V_1 \\ \theta_1 \\ V_2 \\ \theta_2 \end{bmatrix} \quad (\text{A-2})$$

Next, if we have two beam elements, we can find the combined stiffness matrix using the standard direct stiffness approach. With reference to Fig. A-3 we have,

$$\begin{bmatrix} F_2 \\ T_2 \\ F_3 \\ T_3 \end{bmatrix} = \frac{2EI}{L^3} \begin{bmatrix} 6 & 3L & -6 & 3L \\ 3L & 2L^2 & -3L & L^2 \\ -6 & -3L & 6 & -3L \\ 3L & L^2 & -3L & 2L^2 \end{bmatrix} \begin{bmatrix} V_2 \\ \theta_2 \\ V_3 \\ \theta_3 \end{bmatrix} \quad (\text{A-3})$$



So that combining Eq. (A-2) and Eq. (A-3) we obtain

$$\begin{bmatrix} F_1 \\ T_1 \\ F_2 \\ T_2 \\ F_3 \\ T_3 \end{bmatrix} = \frac{2EI}{L} \begin{bmatrix} 6 & 3L & -6 & 3L & 0 & 0 \\ 3L & 2L^2 & -3L & L^2 & 0 & 0 \\ -6 & -3L & 12 & 0 & -6 & -3L \\ 3L & L^2 & 0 & 4L^2 & -3L & L^2 \\ 0 & 0 & -6 & -3L & 6 & -3L \\ 0 & 0 & 3L & L^2 & -3L & 2L^2 \end{bmatrix} \begin{bmatrix} v_1 \\ \theta_1 \\ v_2 \\ \theta_2 \\ v_3 \\ \theta_3 \end{bmatrix} \quad (\text{A-4})$$

K

Equation (A-4) defines the stiffness matrix (K) for the system of Fig. A-1.

### 3. Mass Matrix

The consistent mass matrix is the standard used for finite element techniques (see Ref. A-1, p. 163 for example).

If the mass per unit length of the beam in Fig. A-2 is  $m$  then the consistent mass matrix for this beam element is

$$\begin{bmatrix} F_1 \\ F_2 \\ T_1 \\ T_2 \end{bmatrix} = \frac{mL}{420} \begin{bmatrix} 156 & 54 & 22L & -13L \\ 54 & 156 & 13L & -22L \\ 22L & 13L & 4L^2 & -3L^2 \\ -13L & -22L & -3L^2 & 4L^2 \end{bmatrix} \begin{bmatrix} \ddot{v}_1 \\ \ddot{v}_2 \\ \ddot{\theta}_1 \\ \ddot{\theta}_2 \end{bmatrix} \quad (\text{A-5})$$

Equation (A-5) can be rewritten

$$\begin{bmatrix} F_1 \\ T_1 \\ F_2 \\ T_2 \end{bmatrix} = \frac{mL}{420} \begin{bmatrix} 156 & 22L & 54 & -13L \\ 22L & 4L^2 & 13L & -3L^2 \\ 54 & -13L & 156 & -22L \\ -13L & -3L^2 & -22L & 4L^2 \end{bmatrix} \begin{bmatrix} \ddot{v}_1 \\ \ddot{\theta}_1 \\ \ddot{v}_2 \\ \ddot{\theta}_2 \end{bmatrix} \quad (\text{A-6})$$

The consistent mass matrix for the second mass element is identical (since we assume  $m$  and  $L$  are the same), so the combined result is

$$\begin{bmatrix} F_1 \\ T_1 \\ F_2 \\ T_2 \\ F_3 \\ T_3 \end{bmatrix} = \frac{mL}{420} \underbrace{\begin{bmatrix} 156 & 22L & 54 & -13L & 0 & 0 \\ 22L & 4L^2 & 13L & -3L^2 & 0 & 0 \\ 54 & 13L & 312 & 0 & 54 & -13L \\ -13L & -3L^2 & 0 & 8L^2 & 13L & -3L^2 \\ 0 & 0 & 54 & 13L & 156 & -22L \\ 0 & 0 & -13L & -3L^2 & -22L & 4L^2 \end{bmatrix}}_{M_B} \begin{bmatrix} \ddot{V}_1 \\ \ddot{\theta}_1 \\ \ddot{V}_2 \\ \ddot{\theta}_2 \\ \ddot{V}_3 \\ \ddot{\theta}_3 \end{bmatrix} \quad (\text{A-7})$$

To the mass matrix of Eq. (A-7) we must add the discrete masses and inertias of Fig. A-1

$$M_D = \begin{bmatrix} M_1 & & & & & \\ & I_1 & & & & \\ & & M_2 & & & \\ & & & I_2 & & \\ & & & & M_3 & \\ & & & & & I_3 \end{bmatrix} \quad (\text{A-8})$$

so that the mass matrix for the system of Fig. A-1 is

$$M = M_B + M_D$$

with  $M_B$  taken from Eq. (A-7).

#### 4. The Equation of Motion

The equation of motion for the system of Fig. A-1 is

$$M \ddot{V} + K V = F \quad (\text{A-9})$$

where

$$V = [V_1 \theta_1 V_2 \theta_2 V_3 \theta_3]^T = \text{nodal coordinate vector}$$

$$F = [F_1 T_1 F_2 T_2 F_3 T_3]^T = \text{force vector}$$

and  $M$  and  $K$  are as defined above.

In many cases, the effect of  $M_B$  is negligible and the equation of motion may be approximated as

$$M_D \ddot{V} + K V = F \quad (A-10)$$

with  $M_D$  defined by Eq. (A-8).

### 5. The Eigenvalue Problem

If we set  $V = v e^{ist}$  where  $v$  is a scalar and  $f$  is a vector of dimension 6, then Eq. (A-9) gives us

$$(-s^2 M f + K f) v e^{ist} = F \quad (A-11)$$

now set  $F = 0$  and  $s^2 = \lambda$ , so

$$\lambda M f = K f \quad (A-12)$$

To put this in the standard eigenvalue problem form we will use a double diagonalization procedure:

First we chose  $\phi_1$  so that

$$F = \phi_1 g \text{ and } \phi_1^T M \phi_1 = I \quad (A-13)$$

here  $\phi_1$  is the eigenvector matrix of  $M$ , with the individual eigenvectors scaled to satisfy Eq. (A-13).

Applying Eq. (A-13) to Eq. (A-12) we obtain

$$\lambda g = \phi_1^T K \phi_1 g \quad (A-14)$$

or

$$\lambda g = \hat{K} g \quad (A-15)$$

This is now in standard eigenvalue form. Now set

$$g = \phi_2 h$$

where  $\phi_2$  is the eigenvalue matrix for  $\hat{K}$ . Then

$$\lambda h = \phi_2^T \hat{K} \phi_2 h = Kh \quad (A-16)$$

Now,  $\hat{K}$  is symmetric and hence  $K$  is too. So  $\phi_2^T \hat{K} \phi_2$  is diagonal and consists of the eigenvalues of the system. The eigenvectors are

$$\begin{aligned} h_1 &= [1 \ 0 \ 0 \ 0 \ 0 \ 0] \\ h_2 &= [0 \ 1 \ 0 \ 0 \ 0 \ 0] \\ &\vdots \\ h_6 &= [0 \ 0 \ 0 \ 0 \ 0 \ 1] \end{aligned} \tag{A-17}$$

These can be transformed back into the coordinates of Fig. (A-2) with

$$\phi_i = \phi_1 \phi_2 h_i \quad i = 1, \dots, 6 \tag{A-18}$$

This solution procedure for the eigenvalue problem is well known and avoids inverting the mass matrix. It also allows the eigenvalue routines to work with symmetric matrices throughout. Notice, however, that if Eq. (A-10) is to be used,  $M_D$  is already diagonal and hence easily inverted. In this case, there is no need to use the double diagonalization procedure.

The  $\phi_i$  of Eq. (A-18) are the system mode shapes and the natural frequencies are given by

$$\omega_i = \sqrt{\lambda_i} \quad i = 1, \dots, 6 \tag{A-19}$$

## 6. Effects of Parameter Variations

Table A-1 presents eight sets of parameter values which were used to represent the platform arm model for Fig. A-1. These values are believed to be representative of a power system/platform similar to the 25-kW power system reference concept proposed by Marshall Space Flight Center.

Table A-2 presents the modal frequencies associated with the parameter values of Table A-1. The mode shapes are shown in Fig. A-4 (the mode shapes do not vary qualitatively with changes in parameter values). The following observations can be made:

- A comparison of the results for data sets 7 and 8 show that the mass per unit length of the beam element has a negligible effect on the frequencies. Hence, the consistent mass matrix approach may be set aside in favor of the simpler diagonal lumped mass matrix.

- A comparison of results for data sets 2 and 3 shows that the inertias ( $I_1, I_2, I_3$ ) have little effect on the first symmetric bending mode (mode 3).
- A comparison of results for data sets 4 and 5 shows that the inertia  $I_2$  has little effect on the second bending modes (modes 5 and 6).
- Increasing  $L, M_1$ , or  $I_1$  reduces the modal frequencies and increasing  $EI$  increases them.

#### 7. Comparison of Results to those for a Simple End Loaded Cantilever Beam

The modal frequencies for the first bending mode may be compared to those of a simple end loaded cantilever beam (see Fig. A-5).

The tip deflection is (see for example, Ref. A-2, p. 518)

$$y = \frac{FL^3}{3EI}$$

So the stiffness is

$$K = \frac{F}{y} = \frac{3EI}{L^3}$$

The differential equation is:

$$M \ddot{y} + K y = 0$$

$$\ddot{y} + \frac{K}{M} y = 0$$

So that the natural frequency of vibration is just

$$\omega_n^2 = \frac{K}{m} = \frac{3EI}{ML^3} \tag{A-20}$$

using the parameter values of data set 2 we see

$$\begin{aligned} \omega_n &= \frac{3 \times 38.45 \times 10^6}{(3 \times 10^3) \times (3)^3} = 37.74 \text{ rad/sec} \\ &= 6.0 \text{ Hz} \end{aligned}$$

This is close to the results of data sets 1-5 (5.3 to 7.3 Hz). Hence, to a first approximation, Eq. (A-20) can be used to estimate the lowest frequency of the system of Fig. A-1.

Table A-1. Parameter Values

Data Set	L (m)	$EI_2$ ( $N\text{-m}^2 \times 10^6$ )	m (kg/m)	$M_1$ ( $kg\text{-} \times 10^3$ )	$M_2$ ( $kg\text{-} \times 10^3$ )	$M_3$ ( $kgm^2 \times 10^3$ )	$I_1$ ( $kgm^2 \times 10^3$ )	$I_2$ ( $kgm^2 \times 10^3$ )	$I_3$ ( $kgm^2 \times 10^3$ )
1	3	38.45	12.3	3	13	3	0	86	0
2	↓	↓	0	↓	↓	↓	0	0	0
3	↓	↓	↓	↓	↓	↓	1.2	47	1.0
4	↓	↓	↓	↓	↓	↓	1.2	559	1.2
5	↓	↓	↓	↓	↓	↓	4.2	↓	4.2
6	15	↓	↓	↓	↓	↓	1.2	↓	1.2
7	↓	19.2	↓	↓	↓	↓	↓	↓	↓
8	↓	↓	12.3	↓	↓	↓	↓	↓	↓

Table A-2. Modal Frequencies (Hz)

Data Set	Mode Number					
	1	2	3	4	5	6
1	0	0	7.3	7.7	641	642
2	↓	↓	7.3	907	1139	1753
3	↓	↓	6.8	8.4	34	35
4	↓	↓	6.0	6.8	34	35
5	↓	↓	5.3	5.8	20	22
6	↓	↓	0.6	1.0	14	14
7	↓	↓	0.5	0.7	10	10
8	↓	↓	0.5	0.7	9	9

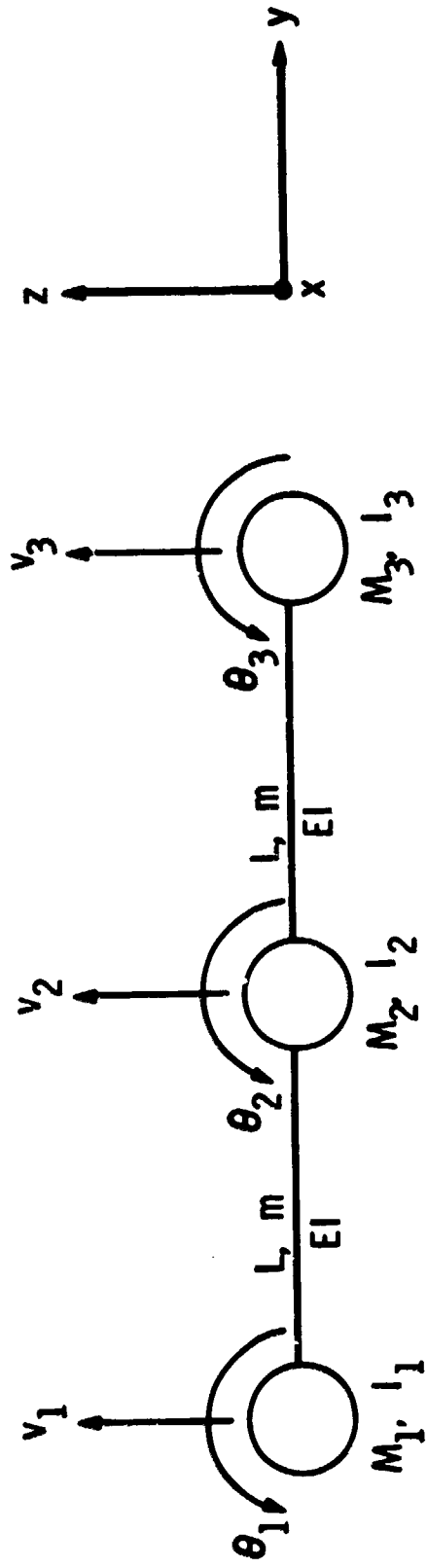


Fig. A-1. Platform Arm Model

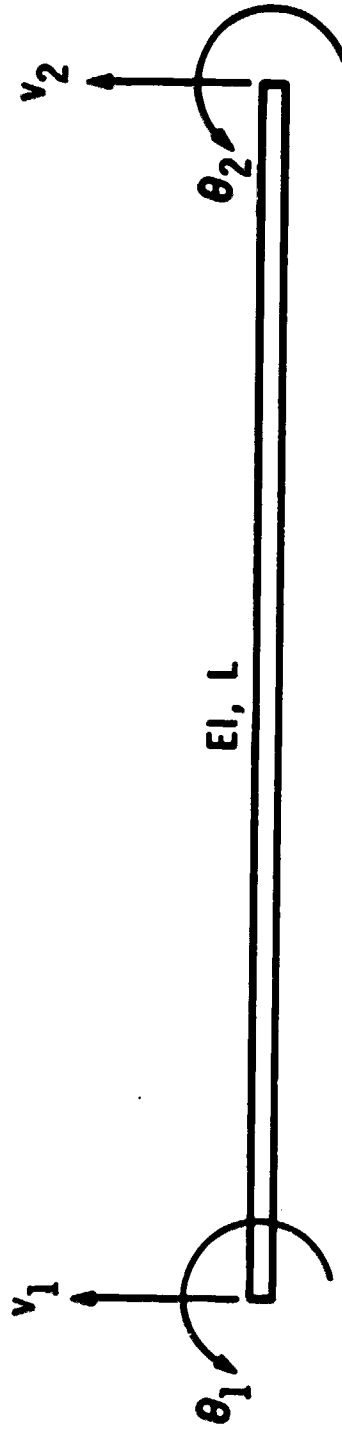


FIG. A-2. Beam Element



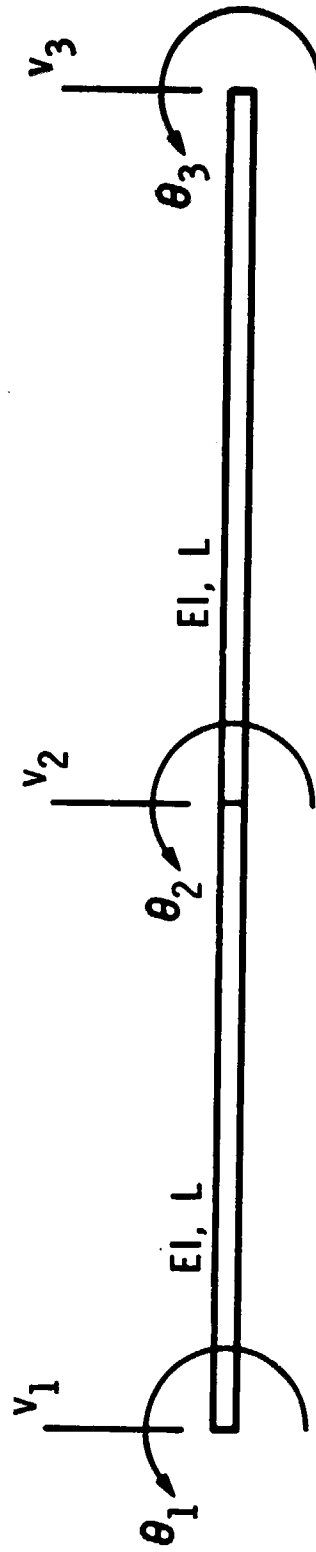
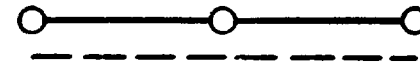
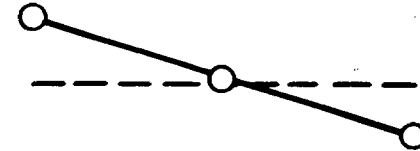


Fig. A-3. Two Beam Elements

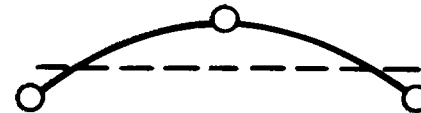
**MODE 1: RIGID BODY TRANSLATION**



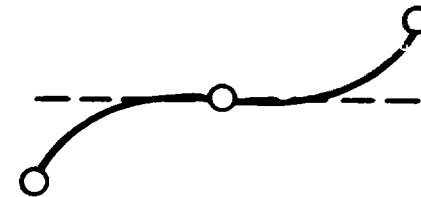
**MODE 2: RIGID BODY ROTATION**



**MODE 3: 1st SYMMETRIC BENDING**



**MODE 4: 1st ANTISYMMETRIC BENDING**



**MODE 5: 2nd SYMMETRIC BENDING**



**MODE 6: 2nd ANTISYMMETRIC BENDING**

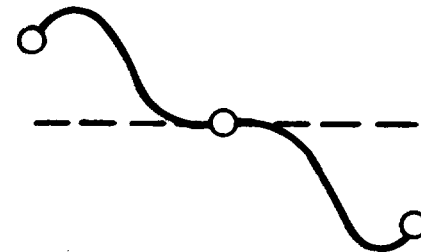


Fig. A-4. Mode Shapes

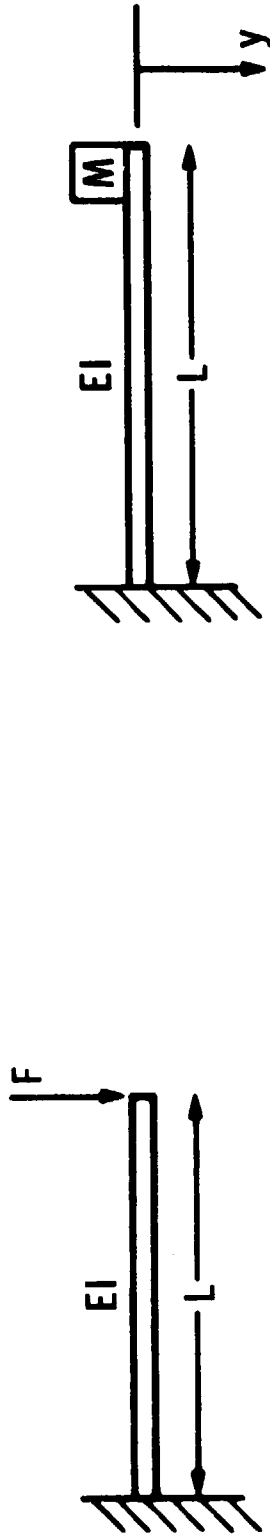


Fig. A-5. Cantilever Beam

## APPENDIX B. MODEL FOR PLATFORM WITH RIGIDLY ATTACHED EXPERIMENTS

This Appendix documents the application of standard techniques to modeling the LSST platform with experiments attached rigidly to the platform arms. The platform arms and solar panels are modeled as flexible appendages to a rigid bus.

Nine-degree- and eleven-degree-of-freedom models are developed by adding flexible solar panels to the model developed in Appendix A.

### 1. Configuration

Figure B-1 shows a simplified configuration used for developing an eleven-degree-of-freedom model for the LSST reference platform. The two degrees of freedom  $\theta_4$  and  $\theta_5$  are later eliminated (see sections which follow) to obtain a nine-degree-of-freedom model. The variables  $\theta_4$ ,  $\theta_5$ ,  $\theta_6$ ,  $V_4$ ,  $V_5$ , and  $V_6$  are associated with the solar panels. The central bus mass and inertia are represented by  $M_2$ ,  $M_5$ ,  $I_2$ , and  $I_5$  ( $M_2 = M_5 = 1/2$  total bus mass,  $I_2 = I_5 = 1/2$  total bus inertia). The two experiment (payload) packages are represented by  $M_1$ ,  $I_1$  and  $M_3$ ,  $I_3$ . The masses  $M_1$  and  $M_3$  are assumed to be connected to the bus by massless beams of length  $L_a$  and flexural rigidity  $EI_a$ . The solar panels are represented by  $M_4$ ,  $I_4$  and  $M_6$ ,  $I_6$  ( $M_4 = M_6$ ,  $I_4 = I_6$ ). The masses  $M_4$  and  $M_6$  are assumed to be connected to the central bus by massless beams of length  $L_b$  and flexural rigidity  $EI_b$ . Since the bus is rigid we have  $\theta_2 = \theta_5$ .

### 2. Solar Panel Model

The solar panel model has six degrees of freedom (before applying the constraint that  $\theta_2 = \theta_5$ ). The stiffness matrix found by finite element techniques (see Appendix A, Eq. (A-4)) is

$$\begin{bmatrix} F_4 \\ T_4 \\ F_5 \\ T_5 \\ F_6 \\ T_6 \end{bmatrix} = \frac{2EI_b}{L_b} \underbrace{\begin{bmatrix} 6 & 3L & -6 & 3L & 0 & 0 \\ & 2L^2 & -3L & L^2 & 0 & 0 \\ & & 12 & 0 & -6 & 3L \\ & & & 4L^2 & -3L & L^2 \\ & & & & 6 & -3L \\ & & & & & 2L^2 \end{bmatrix}}_{K_b} \begin{bmatrix} V_4 \\ \theta_4 \\ V_5 \\ \theta_5 \\ V_6 \\ \theta_6 \end{bmatrix}$$

Here  $F_i$ ,  $i = 4,5,6$  are the forces associated with the displacements  $V_i$ ,  $i = 4,5,6$ ; and  $T_i$ ,  $i = 4,5,6$  are the torques associated with the rotations  $\theta_i$ ,  $i = 4,5,6$ .

A diagonal mass matrix is used (see Appendix A, Eq. (A-8)).

$$\begin{bmatrix} F_4 \\ T_4 \\ F_5 \\ T_5 \\ F_6 \\ T_6 \end{bmatrix} = \underbrace{\begin{bmatrix} M_4 & & & & & \\ & I_4 & & & & \\ & & M_5 & & & \\ & & & I_5 & & \\ & & & & M_6 & \\ & & & & & I_6 \end{bmatrix}}_{M_D} \begin{bmatrix} \ddot{V}_4 \\ \ddot{\theta}_4 \\ V_5 \\ \ddot{\theta}_5 \\ V_6 \\ \ddot{\theta}_6 \end{bmatrix}$$

### 3. Constraint Implementation ( $\theta_2 = \theta_5$ )

The stiffness and mass matrices for the platform have an identical form, (Appendix A Eqs. (A-4) and (A-8)). In order to combine them we set  $T_2 = T_5$ , and  $\theta_2 = \theta_5$  to obtain an 11 by 11 mass matrix and stiffness matrix.

This procedure is straightforward. First reorder the rows and columns of the matrices so that for the platform arms we have the  $T_2, \theta_2$  equation on the bottom:

$$\begin{bmatrix} F_1 \\ T_1 \\ F_2 \\ F_3 \\ T_3 \\ T_2 \end{bmatrix} = \begin{bmatrix} \text{reordered} \\ \text{stiffness} \\ \text{matrix} \\ \text{(or reordered} \\ \text{mass matrix)} \end{bmatrix} \begin{bmatrix} V_1 \\ \theta_1 \\ V_2 \\ V_3 \\ \theta_3 \\ \theta_2 \end{bmatrix}$$

For the solar panels reorder the rows and columns of the matrices so that the  $T_5, \theta_5$  equation is on the top (and then set  $T_5 = T_2, \theta_5 = \theta_2$ ):

$$\begin{bmatrix} T_2 \\ F_4 \\ T_4 \\ F_5 \\ F_6 \\ T_6 \end{bmatrix} = \begin{bmatrix} \text{reordered} \\ \text{stiffness} \\ \text{matrix} \\ \text{(or reordered} \\ \text{mass matrix)} \end{bmatrix} \begin{bmatrix} \theta_2 \\ V_4 \\ \theta_4 \\ V_5 \\ V_6 \\ \theta_6 \end{bmatrix}$$





and  $K_{tt}$ ,  $K_{t\theta}$ ,  $K_{\theta t}$ ,  $K_{\theta\theta}$ , are the partitioned elements of the reordered stiffness matrix.

Now set  $I_4 = I_6 = 0$ . Also set  $T_4 = T_6 = 0$ , since we assume that no external torques will be applied to the masses  $M_4$ ,  $M_6$ .

$$\begin{bmatrix} F_t \\ 0 \end{bmatrix} = \begin{bmatrix} K_{tt} & K_{t\theta} \\ K_{\theta t} & K_{\theta\theta} \end{bmatrix} \begin{bmatrix} v_t \\ v_\theta \end{bmatrix}$$

then

$$K_{\theta t} v_t + K_{\theta\theta} v_\theta = 0$$

or

$$v_\theta = -K_{\theta\theta}^{-1} K_{\theta t} v_t \quad (\text{B-1})$$

and so

$$F_t = (K_{tt} - K_{t\theta} K_{\theta\theta}^{-1} K_{\theta t}) v_t$$

So the reduced stiffness matrix is represented by:

$$\hat{K} = K_{tt} - K_{t\theta} K_{\theta\theta}^{-1} K_{\theta t} \quad (\text{B-2})$$

Using  $\hat{K}$  and  $\hat{M}$  we can now work the problem with nine degrees of freedom instead of eleven. Also, Eq. (B-1) can be used to solve for  $\theta_4$  and  $\theta_6$  under the assumption that  $I_4 = I_6 = 0$ . Notice that  $\theta_4$  and  $\theta_6$  will not be zero.

### 5. The Equation of Motion

The equation of motion for the system of Fig. B-1 is

$$\hat{M} \ddot{v}_t + \hat{K} v_t = F_t$$

where  $\hat{M}$ ,  $\hat{K}$ ,  $v_t$ , and  $F_t$  are as previously defined.

### 6. The Eigenvalue Problem

The eigenvalue problem has the same form as that given in Appendix A, Eq. (A-12)

$$\lambda \hat{M} f = \hat{K} f$$



where  $\lambda$  is the scalar eigenvalue ( $\lambda = \omega_n^2$  = natural frequency squared) and  $f$  is the eigenvector (or mode shape) associated with  $\lambda$ .

### 7. Mode Shapes for System Elements

In order to visualize the system mode shapes, it is instructive to first examine the mode shapes of the individual elements. Our model has two types of elements as shown in Fig. B-2. Type 1 has 4 degrees of freedom giving two rigid body modes and two elastic modes. Type 2 has 3 degrees of freedom, giving two rigid body modes and one elastic mode.

Figure B-3 shows the mode shapes for the type 1 element. The type 2 element has the same first three mode shapes shown in Fig. B-3 but lacks the 4th mode.

The first two mode shapes involve no strain energy (since the beam element connecting the end masses is undeformed) and have  $\omega_n = 0$ . The 4th mode shape has a higher strain energy than the 3rd mode and also a higher natural frequency.

### 8. Sample Computer Run Results

Four computer runs were made with the eleven-degree-of-freedom model and two runs with the nine-degree-of-freedom model. Table B-1 lists the parameter values used and Table B-2 the resulting natural frequencies.

Comparison of runs 4 and 5 show that the results are identical for the first nine modes. In other words, run nine confirms the fact that eliminating  $\theta_4$  and  $\theta_6$  is equivalent to setting  $I_4$  and  $I_6$  to zero.

Comparison of runs 2 and 3 shows that increasing the mass and inertia of the experiments ( $M_1, I_1, M_3, I_3$ ) results in lower frequencies for the bending modes of the platform arms, but has little or no effect on the solar panel modes.

Comparison of runs 1 and 2 shows that increasing  $L$  and decreasing  $EI$  lowers the natural frequencies as we would expect.

As pointed out in Appendix A, the lowest frequency is roughly proportional to  $\sqrt{EI/ML^3}$  or

$$\omega_n = C \sqrt{\frac{EI}{ML^3}}; C = \text{constant}$$

Between runs 1 and 2 this ratio for the platform arms changed by an amount

$$\frac{\omega_{n1}}{\omega_{n2}} = \sqrt{\frac{1000/10}{1}} = 10.0$$

This agrees well with the computer run results for the 1st symmetric mode:

$$\frac{\omega_{n1}}{\omega_{n2}} = 3.91/.546 = 7.2 \quad \text{for platform arms}$$

$$\frac{\omega_{n1}}{\omega_{n2}} = .356/.035 = 10 \quad \text{for solar panels.}$$

Comparison of runs 2 and 4 shows what the result of neglecting  $I_4$  and  $I_6$  is on the modes retained. The platform arm modes are unaffected and the solar panel mode frequencies increase somewhat (compare modes 8 and 9 for runs 2 and 4). When using the nine-degree-of-freedom model, the flexural rigidity (EI) can be reduced somewhat as compared with the eleven-degree-of-freedom model if the same modal frequencies are desired for the modes 8 and 9.

The mode shapes for the system of Fig. B-1 are sketched in Figs. B-4 through B-6. The mode shapes do not differ qualitatively from run to run. The shapes are various combinations of the element shapes sketched in Fig. B-3. Table B-3 lists the mode shapes quantitatively for run 6.

#### 9. Comments on Interaxis Coupling

The mode shapes of Figs. B-4 through B-6 demonstrate clearly that x and y axis rotations are tightly coupled (see Fig. B-1 for axis definition). For example, any input which excites the symmetric bending modes of the platform arm will cause the rotations  $\theta_1$  and  $\theta_3^*$ . But, because the symmetric bending mode results in a displacement  $V_2$ , this motion will cause rotations of  $M_2$  and  $M_5$  about their y axes. This in turn will excite torsional modes (not modeled in this paper) associated with the solar panels and platform arms. In this way, we can see that all six masses will have rotations about their y axes as a result of an excitation of a platform arm symmetric mode.

---

\*The torques  $T_1$  and  $T_3$ , for example, will excite these modes (but  $T_2$  will not).

The magnitude of this coupling will depend on the parameters of the model and may or may not be small enough to permit meaningful single axis control system designs. This coupling effect will be examined more carefully in future work.

Table B-1 Run Parameters










<u>Parameter</u>	<u>Run 1</u>	<u>Run 2</u>	<u>Run 3</u>	<u>Run 4</u>	<u>Run 5</u>	<u>Run 6</u>
<u>Platform Arms</u>						
$L_a$ (m)	5	15				15
$EI_a$ ( $N\text{-m}^2 \times 10^6$ )	40	20				20
$M_1$ ( $kg \times 10^3$ )	3	3	12	3	3	3
$I_1$ ( $kg\text{-m}^2 \times 10^3$ )	1	1	4	1	1	1
$M_2$ ( $kg \times 10^3$ )	6					6
$I_2$ ( $kg\text{-m}^2 \times 10^3$ )	60					50
$M_3$ ( $kg \times 10^3$ )	3	3	13	3	3	3
$I_3$ ( $kg\text{-m}^2 \times 10^3$ )	1	1	4	1	1	1
<u>Solar Panels</u>						
$L_b$ (m)	20					20
$EI_b$ ( $N\text{-m}^2 \times 10^6$ )	10	.1				.1
$M_4$ ( $kg \times 10^3$ )	0.5					.5
$I_4$ ( $kg\text{-m}^2 \times 10^3$ )	50	50	50	0.001	0	0
$M_5$ ( $kg \times 10^3$ )	6					6
$I_5$	X	X	X	X	X	X
$M_6$ ( $kg \times 10^3$ )	0.5					.5
$I_6$ ( $kg\text{-m}^2 \times 10^3$ )	50	50	50	0.001	0	0

Table B-2 Natural Frequencies (Hz)

<u>Rigid Body Modes</u>	<u>Run 1</u>	<u>Run 2</u>	<u>Run 3</u>	<u>Run 4</u>	<u>Run 5</u>	<u>Run 6</u>
1 (solar panel translation)	0	—————→				0
2 (arm translation)	0	—————→				0
3 (rotation)	0	—————→				0
<u>Platform Arm Modes</u>						
4 (1st symmetric)	3.91	.546	.430	.546	.546	.546
5 (1st antisymmetric)	5.75	2.04	1.98	2.04	2.04	2.04
6 (2nd symmetric)	29.3	11.7	5.86	11.7	11.7	11.7
7 (2nd antisymmetric)	29.3	11.7	5.95	11.7	11.7	11.7
<u>Solar Panel Modes</u>						
8 (1st symmetric)	.356	.035	.035	.047	.047	.0471
9 (1st antisymmetric)	.584	.039	.035	.049	.049	.0493
10 (2nd symmetric)	1.33	.133	.133	22.5	X	X
11 (2nd antisymmetric)	1.37	.130	.129	22.5	X	X

Table B-3 Mode Shapes for Run 6

Coordinate	Mode Number and Displacement								
	1	2	3	4	5	6	7	8	9
V <sub>1</sub>	0	-9.1E-3	-1.1E-2	9.1E-3	2.4E-3	7.4E-4	7.5E-4	0	-6.0E-3
V <sub>2</sub>	0	-9.1E-3	0	-9.1E-3	0	-7.4E-4	0	0	0
V <sub>3</sub>	0	-9.1E-3	1.1E-2	9.1E-3	-2.4E-3	7.4E-4	-7.5E-4	0	6.0E-3
1	0	0	7.4E-4	-1.8E-3	-2.5E-3	2.2E-2	2.2E-2	0	4.0E-4
3	0	0	7.4E-4	1.8E-3	-2.5E-3	-2.2E2	2.2E-2	0	4.0E-4
2	0	0	7.4E-4	0	4.1E-3	0	4.6E-4	0	3.9E-4
V <sub>4</sub>	1.2E-2	0	-1.5E-2	0	4.0E-5	0	1.3E-7	2.9E-2	-2.8E-2
V <sub>5</sub>	1.2E-2	0	0	0	0	0	0	-4.9E-3	0
V <sub>6</sub>	1.2E-2	0	1.5E-2	0	-4.0E-5	0	-1.3E-7	2.9E-2	-2.8E-2

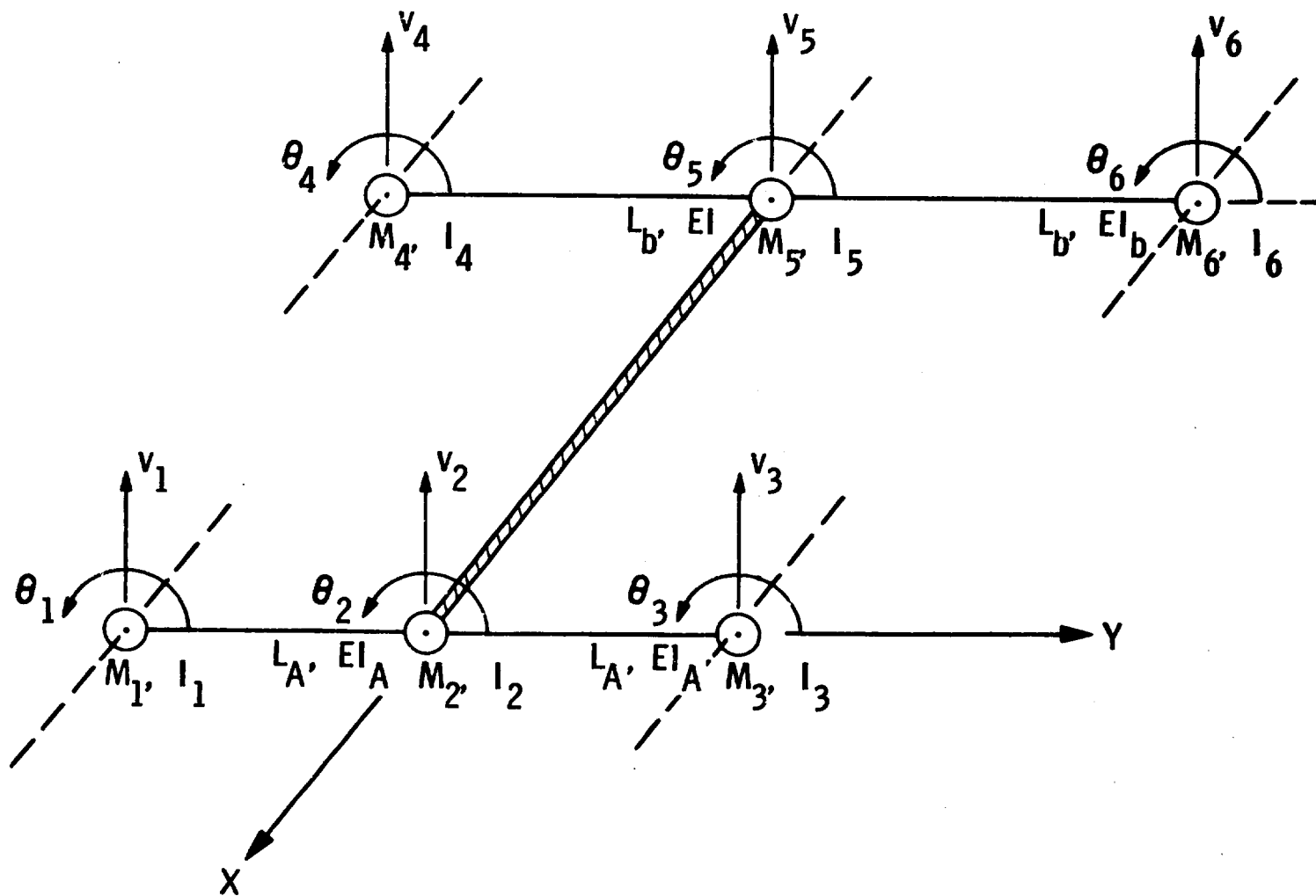
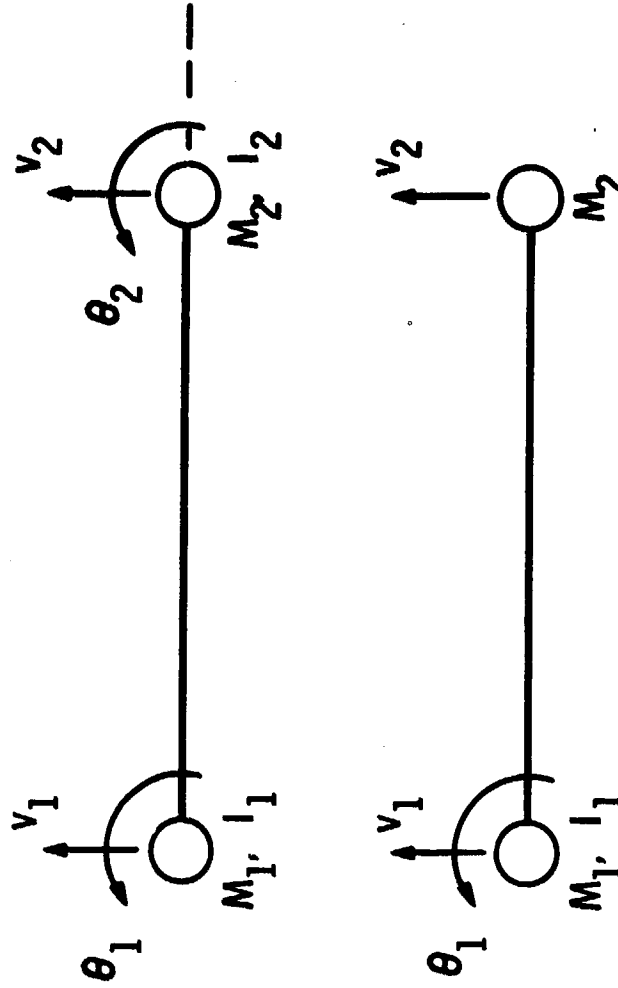


Fig. B-1. Model for Platform X Axis



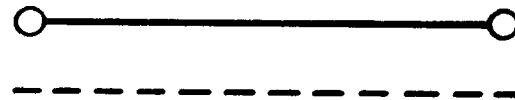
TYPE 1 ELEMENT

TYPE 2 ELEMENT

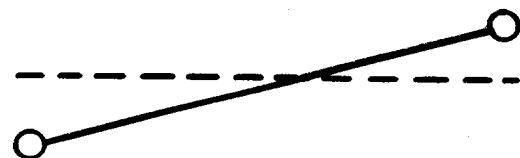
Fig. B-2. Two Element Types



MODE 1: RIGID BODY TRANSLATION



MODE 2: RIGID BODY ROTATION



MODE 3: 1st BENDING MODE

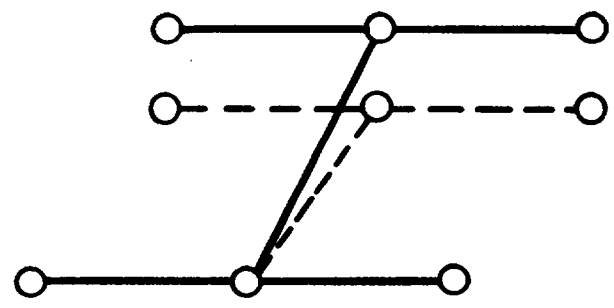


MODE 4: 2nd BENDING MODE

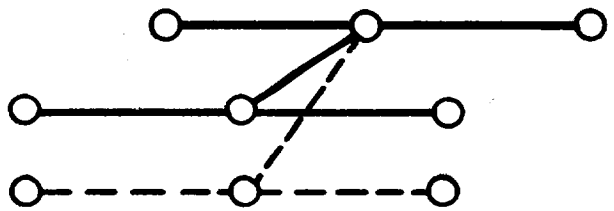


Fig. B-3. Mode Shapes for Type 1 Element

**MODE 1: RIGID BODY TRANSLATION OF SOLAR PANELS**



**MODE 2: RIGID BODY TRANSLATION OF PLATFORM ARMS**



**MODE 3: RIGID BODY ROTATION**

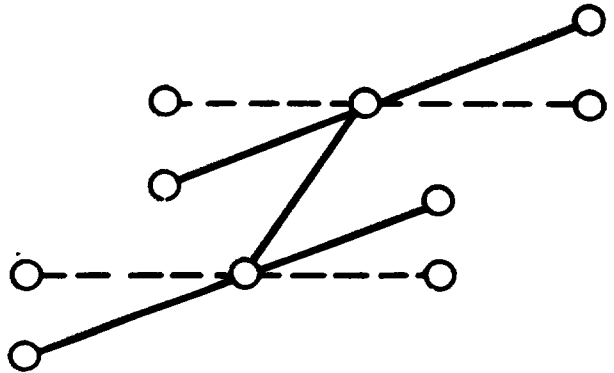
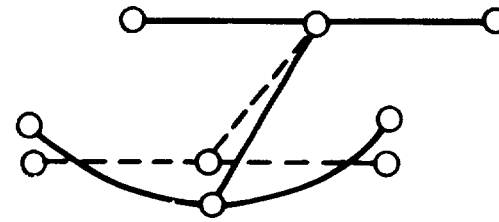
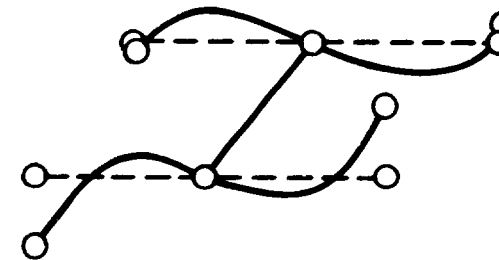


Fig. B-4. Rigid Body Modes

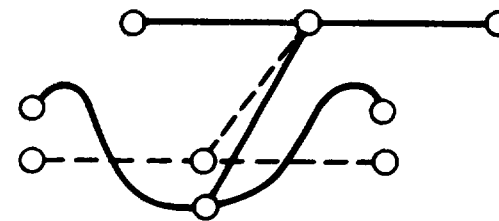
MODE 4: 1st SYMMETRIC BENDING MODE



MODE 5: 1st ANTISYMMETRIC BENDING MODE



MODE 6: 2nd SYMMETRIC BENDING MODE



MODE 7: 2nd ANTISYMMETRIC BENDING MODE

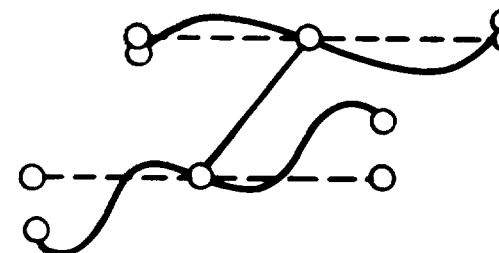
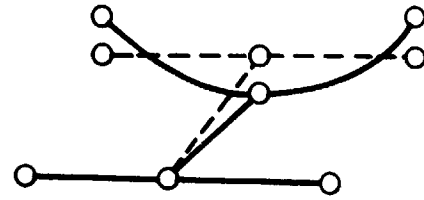
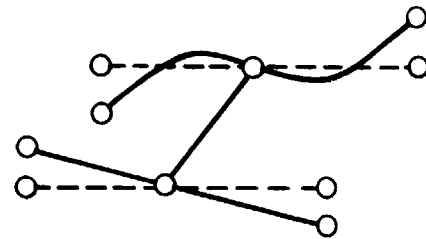


Fig. B-5. Elastic Modes for Platform Arms

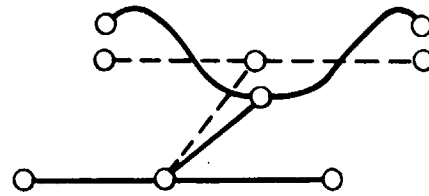
MODE 8: 1st SYMMETRIC BENDING MODE



MODE 9: 1st ANTISYMMETRIC BENDING MODE



MODE 10: 2nd SYMMETRIC BENDING MODE



MODE 11: 2nd ANTISYMMETRIC BENDING MODE

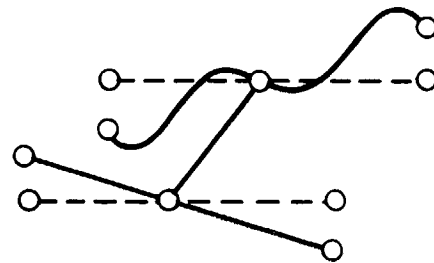


Fig. B-6. Elastic Modes for Solar Panels

## APPENDIX C. TRANSFER FUNCTIONS

This Appendix documents transfer functions for the nine-degree-of-freedom model of Appendix B. Transfer functions are developed from modal data. Comments on observability and controllability are made for torque actuators and angular position sensors on the central bus or on the platform arms. Transfer functions are included for noncolocated actuators and sensors.

### 1. Transfer Function Derivation

This section addresses the derivation of transfer functions between a force (or torque) at any point in a structure to a sensor at any point in the structure.

For this purpose the system model is assumed to have  $n$  degrees of freedom and be of the form

$$\ddot{Mx} + Kx = F = Bu \quad (C-1)$$

$$y = Cx$$

where

$x$  is the  $n$  "dimensional" nodal coordinate vector

$u$  is the  $m$  "dimensional" control input vector

$F$  is the  $n$  "dimensional" force vector

$y$  is the  $l$  "dimensional" output vector

$M$  is the  $n \times n$  mass matrix

$K$  is the  $n \times n$  stiffness matrix

$B$  is the  $n \times m$  control distribution matrix

$C$  is the  $l \times n$  output matrix

Let  $\phi$  be the  $n \times n$  matrix of eigenvectors for this system such that:

$$\phi^T M \phi = I$$

and

$$\phi^T K \phi = \Lambda^2$$

where  $I$  is the identity matrix and  $\Lambda^2$  is the diagonal matrix of eigenvalues (or modal frequencies squared).

Then Eq. (C-1) can be rewritten in terms of the modal coordinates  $q$  ( $x = \phi q$ ) as

$$\ddot{q} + \Lambda^2 q = \phi^T F \quad (C-2)$$

Suppose we now assume modal damping\* and write

$$\ddot{q} + D\dot{q} + \Lambda^2 q = \phi^T F \quad (C-3)$$

where  $D$  is a diagonal damping matrix.

Now take the Laplace transform of Eq. (C-3) to obtain:

$$q(s) = (s^2 I + sD + \Lambda^2)^{-1} \phi^T F \quad (C-4)$$

or in terms of the original coordinates

$$x(s) = \phi (s^2 I + sD + \Lambda^2)^{-1} \phi^T F(s) \quad (C-5)$$

Equation (C-5) gives the transfer matrix relating  $F$  to  $x$ . The transfer matrix between  $u$  and  $y$  is given by

$$y(s) = C \phi (s^2 I + sD + \Lambda^2)^{-1} \phi^T B u(s) \quad (C-6)$$

To find the transfer function between any force ( $F_j$ ) and nodal coordinate ( $x_k$ ) we proceed as follows: define

$$\begin{aligned} Q(s) &= (s^2 I + sD + \Lambda^2)^{-1} \\ &= \text{diag. } (Q_1(s) \ Q_2(s) \ \dots \ Q_n(s)) \end{aligned}$$

$$Q_i(s) = (s^2 + 2\zeta_i \omega_i s + \omega_i^2)^{-1}$$

$$\phi_i = [\phi_{1i} \ \phi_{2i} \ \dots \ \phi_{ni}]$$

and

$$\phi_i^T = [\phi_{1i} \ \phi_{2i} \ \dots \ \phi_{ni}]^T$$

\*See, for example, Ref. A-1, pages 194-199 for a discussion of this assumption.

where

$\phi_{ji}$  is the  $j$ th component of the  $i$ th eigenvector

$\zeta_i$  =  $i$ th modal damping coefficient

$\omega_i$  =  $i$ th natural frequency

Then, from Eq. (C-5) we have

$$\begin{aligned} x(s) &= [\phi_1 \ \phi_2 \ \dots \ \phi_n] \begin{bmatrix} Q_1(s) \\ Q_2(s) \\ \vdots \\ Q_n(s) \end{bmatrix} \begin{bmatrix} \phi_1^T \\ \phi_2^T \\ \vdots \\ \phi_n^T \end{bmatrix} F(s) \\ &= \left( \sum_{i=1}^n \phi_i Q_i(s) \phi_i^T \right) F(s) \end{aligned} \quad (C-7)$$

Equation (C-7) is an alternate representation of the transfer matrix given in Eq. (C-5). Now define

$$x(s) = (x_1 \ x_2 \ \dots \ x_n)^T$$

$$F(s) = (F_1 \ F_2 \ \dots \ F_n)^T$$

so that

$$x_k(s) = \left( \sum_{i=1}^n \phi_{ki} Q_i(s) \phi_{ji} \right) F_j(s) \quad (C-8)$$

Equation (C-8) defines the transfer function between the force  $F_j$  and the nodal coordinate  $x_k$ .

Using (C-7) we can write (C-6) as

$$\begin{aligned} y(s) &= C \left( \sum_{i=1}^n \phi_i Q_i \phi_i^T \right) B u(s) \\ &= \left( \sum_{i=1}^n C \phi_i Q_i \phi_i^T B \right) u(s) \end{aligned} \quad (C-9)$$

now set

$$B = [B_1^T \ B_2^T \ \dots \ B_n^T]^T$$

$$C = [C_1 \ C_2 \ \dots \ C_k]$$

where each  $B_i$  is a  $1 \times m$  row vector and each  $C_i$  is a  $n \times 1$  column vector.

Then

$$\begin{aligned} \phi_i^T B &= \sum_{j=1}^n \phi_{ji} B_j \triangleq \hat{B}_i \\ &= 1 \times m \text{ row vector} \end{aligned}$$

and

$$\begin{aligned} C \phi_i &= \sum_{j=1}^n C_j \phi_{ji} \triangleq \hat{C}_i \\ &= l \times 1 \text{ column vector} \end{aligned}$$

$$y(s) = \left[ \sum_{i=1}^n \left( \sum_{j=1}^n C_j \phi_{ji} \right) Q_i(s) \left( \sum_{j=1}^n \phi_{ji} B_j \right) \right] u(s) \quad (C-10)$$

$$= \left[ \sum_{i=1}^n \hat{C}_i Q_i(s) \hat{B}_i \right] u(s) \quad (C-11)$$

now, define

$$\hat{B}_i = (\hat{B}_{i1} \hat{B}_{i2} \dots \hat{B}_{im})$$

$$\hat{C}_i = (\hat{C}_{1i} \hat{C}_{2i} \dots \hat{C}_{li})^T$$

where  $\hat{B}_{ij}$  and  $\hat{C}_{ki}$  are scalars. Define

$$y(s) = (y_1 \ y_2 \ \dots \ y_l)^T$$

$$u(s) = (u_1 \ u_2 \ \dots \ u_m)^T$$

so that

$$y_k(s) = \left[ \sum_{i=1}^n \hat{C}_{ki} Q_i(s) \hat{B}_{ij} \right] u_j(s) \quad (C-12)$$

Equation (C-12) defines the transfer function between the control input  $u_j$  and the output  $y_k$ .

## 2. Transfer Function Symmetry

Equation (C-8) demonstrates that the following two transfer functions are equivalent:



$$\frac{x_k}{F_j}(s) = \frac{x_j}{F_k}(s)$$

This result is known as Maxwell's law of reciprocal deflections (discovered in 1864)\*. The symmetry seen here arises because of the symmetry of the original M and K matrices.

### 3. Transfer Function Zeros

The number of zeros ( $N_z$ ) in the numerator of Eq. (C-7) (or (C-12)) is not at all obvious. An upper bound is  $N_z = n - 2$ . This can be seen by expanding Eq. (C-7) over a common denominator which is the product

$$\prod_{i=1}^n (s^2 + 2 \zeta_i \omega_i s + \omega_i^2)$$

However, in many cases the degree of the numerator polynomial will be less than  $n-2$  when  $k \neq j$ .

As an example, consider the system of Fig. C-1. For this system the transfer function  $x_1(s)/F_1(s)$  has 6 zeros,  $x_2(s)/F_1(s)$  has 4 zeros,  $x_3(s)/F_1(s)$  has 2 zeros, and  $x_4(s)/F_1(s)$  has no zeros.

This can be demonstrated as follows. The system equations are ( $K_{ij} \triangleq K_i + K_j$ )

$$\underbrace{\begin{bmatrix} M_1 s^2 + K_1 & & & & & \\ & -K_1 & & & & \\ & & M_2 s^2 + K_{12} & & & \\ & & & -K_2 & & \\ & & & & M_3 s^2 + K_{23} & \\ & & & & & -K_3 \\ & & & & & & M_4 s^2 + K_3 \end{bmatrix}}_{Ms^2 + K} \begin{bmatrix} x_1 \\ x_2 \\ x_3 \\ x_4 \end{bmatrix} = \begin{bmatrix} F_1 \\ F_2 \\ F_3 \\ F_4 \end{bmatrix}$$

To find the inverse of the matrix  $(Ms^2 + K)$  we can use Cramer's rule. The numerator of the inverse has the form

\* See for example, Ref. C-1, p. 494.

$$\begin{bmatrix} N_{11} & N_{12} & N_{13} & N_{14} \\ N_{21} & N_{22} & N_{23} & N_{24} \\ N_{31} & N_{32} & N_{33} & N_{34} \\ N_{41} & N_{42} & N_{43} & N_{44} \end{bmatrix}$$

and the denominator is the determinant of  $(Ms^2 + K)$ . Each element  $N_{ij}$  is found by deleting the  $i$ th row and  $j$ th column of  $Ms^2 + K$  and taking the determinant with proper sign. So

$$N_{11} = \begin{vmatrix} M_2 s^2 + K_{12} & -K_2 & 0 \\ -K_2 & M_3 s^2 + K_{23} & -K_3 \\ 0 & -K_3 & M_4 s^2 + K_3 \end{vmatrix}$$

In this case, the coefficient of the  $s^6$  term is  $M_2 M_3 M_4$  so  $N_{11}$  has degree 6. For  $N_{12}$  we have:

$$N_{12} = - \begin{vmatrix} -K_1 & -K_2 & 0 \\ 0 & M_3 s^2 + K_{23} & -K_3 \\ 0 & -K_3 & M_4 s^2 + K_3 \end{vmatrix}$$

In this case, there is no  $s^6$  term and the  $s^4$  term coefficient is  $K_1 M_3 M_4$ .

For  $N_{13}$  we have:

$$N_{13} = \begin{vmatrix} -K_1 & M_2 s^2 + K_{12} & 0 \\ 0 & -K_2 & -K_3 \\ 0 & 0 & M_4 s^2 + K_3 \end{vmatrix} = (M_4 s^2 + K_3) (K_1 \cdot K_2)$$

So, in this case, we have  $s^2$  as the highest degree of  $s$ .

For  $N_{14}$  we have:

$$N_{14} = - \begin{vmatrix} -K_1 & M_2 s^2 + K_{12} & -K_2 \\ 0 & -K_2 & M_3 s^2 + K_{23} \\ 0 & 0 & -K_3 \end{vmatrix} = -K_1 \cdot K_2 \cdot K_3$$

so  $N_{14}$  is just a constant term, and there are no zeros in the transfer functions  $x_4(s)/F_1(s) = x_1(s)/F_4(s)$ .

So we conclude that for chain systems of this type we can determine pretty much by inspection the number of (finite) zeros. For other systems this is not so easy, especially when the M and K matrices are full or nearly full.

It should be noted, however, that if zeros at infinity are included, then every transfer function can be thought of as having the same number of zeros as poles.

Suppose that we compute the transfer functions using Eq. (C-7). Then because of computational inaccuracies the order of the numerator polynomial for each transfer function will almost always turn out to be  $n-2$  for systems of any size.

If a polynomial root finder is employed it will attempt to find  $n-2$  roots. It may or may not be successful and if it is successful, some of the roots found may have very large magnitudes. The user of such a program should understand that the most probable explanation for the root finder bombing out or obtaining roots with very large magnitude is that the true system has fewer zeros than  $n-2$ .

If the root finder does bomb out, it is necessary to reduce the polynomial to a lower degree (by simple truncation) before attempting another solution. If the root finder obtains very large values for the zeros (as compared to the pole magnitudes) then these zeros should usually be discarded (which is equivalent to replacing them by zeros at infinity). Some judgement is required, however, on what is "too large."

#### 4. Numerical Results for Nine-Degree-of-Freedom Model

The initial control problem for this structure is related to the angles,  $\theta_1$ ,  $\theta_2$ ,  $\theta_3$  where  $\theta_1$  and  $\theta_3$  are the experiment pointing angles and  $\theta_2$  is the central bus orientation angle.

The associated control torques are defined as  $T_1$ ,  $T_2$ , and  $T_3$ ; where  $T_i$ ,  $i = 1, 2, 3$  is the torque applied at  $M_i$ ,  $i = 1, 2, 3$  about the x axis.

The transfer functions of interest are:

$\frac{\theta_1}{T_1}(s)$  = transfer function between a torque applied at  $M_1$  and the rotation angle at same location.

$\frac{\theta_2}{T_2}(s)$  = transfer function between a torque applied at the central bus and the rotation angle at same location.

$\frac{\theta_1}{T_2}(s)$  = transfer function between a torque applied at the central bus and the rotation angle at  $M_1$ .

$\frac{\theta_1}{T_3}(s)$  = transfer function between a torque applied at  $M_3$  and the rotation angle at  $M_1$ .

Also of interest are the following transfer functions

$$\text{and } \frac{\theta_2}{T_1}(s) = \frac{\theta_1}{T_2}(s)$$

$$\frac{\theta_2}{T_1}(s) = \frac{\theta_1}{T_3}(s)$$

There are many other possible transfer functions of lesser interest which will not be discussed.

Figures C-2 through C-5 present pole/zero configurations for the four principal transfer functions resulting from the model of Appendix B using

the Run 6 data set parameters. For simplicity of plotting no damping has been added. The gain (K) of the transfer function has also been shown using the following convention

$$G(s) = \frac{K (s-Z_1)(s-Z_2) \dots (s-Z_m)}{(s-P_1)(s-P_2) \dots (s-P_m)}$$

where

$Z_i$  = the  $i$ th zero

and

$P_j$  = the  $j$ th pole.

### 5. Observability and Controllability

The pole/zero plots of Figs. C-2 through C-5 give us information on observability and controllability. Whenever pole/zero cancellation occurs this is an indication that either observability or controllability (or both) has been lost (see next section).

Figure C-2 shows us that for  $\frac{\theta_1}{T_1}$  (s) there is a pole/zero cancellation at  $\omega = 0.296$  rad/s. This frequency corresponds to the first symmetric mode of the solar panels. Any motion observed at  $M_1$  as a result of solar panel motion must be transmitted through the bus. The symmetric modes of the solar panels, however, are not transmitted to the platform arms (see Appendix B) so this indicates a lack of observability. Furthermore, this mode is not controllable since rotations and displacements of the platform arm cannot excite the symmetric modes of the solar panels.

Figure C-3 shows us that for  $\frac{\theta_2}{T_2}$  (s) there are pole/zero cancellations at  $\omega = 0.296, 3.43,$  and  $73.3$  rad/s. These frequencies correspond to the symmetric modes of the solar panels and platform. Since the symmetric modes do not affect  $\theta_2$  these modes are not observable, and since a torque  $T_2$  cannot excite these modes they are not controllable either.

Figure C-4 shows us that for  $\frac{\theta_1}{T_2}$  (s) and  $\frac{\theta_2}{T_1}$  (s) there are pole zero cancellation at  $\omega = 0.296, 3.43,$  and  $73.3$  rad/s. As before the solar panel mode is neither controllable or observable. This is true for both

$\frac{\theta_1}{T_1}(s)$  and  $\frac{\theta_2}{T_1}(s)$ . The platform arm symmetric modes are observable in  $\frac{\theta_1}{T_2}(s)$  but not controllable. In the case of  $\frac{\theta_2}{T_1}(s)$  the reverse is true: the platform arm symmetric modes are controllable but not observable.

Figure C-5 shows us that for  $\frac{\theta_1}{T_3}(s)$  and  $\frac{\theta_3}{T_1}(s)$  all the modes are controllable and observable except the solar panel symmetric modes which are neither controllable nor observable.

It should be noted that controllability and observability of a particular mode are necessary if we are to change the dynamics of a system related to that mode, but do not in themselves assure us that a satisfactory control system design can be achieved. For example, the configurations of Figs. C-3 and C-4 will be much more difficult to control because of the consecutive pole patterns on (or near) the imaginary axes, and because of the right-half plane zero(s).

It should be noted that although the symmetric modes of the platform arms and solar panels are not controllable or observable at the central bus when considering  $\theta_2$  and  $T_2$ , they become both controllable and observable when torques and motions about the y-axis of the bus are included. The present model does not include these torques explicitly, but they are implicit in the forces  $F_2$  and  $F_5$  and the displacements  $V_2$  and  $V_5$ .

## 6. More on Pole Zero Cancellations

In the previous section we used arguments associated with the mode shapes to determine whether pole zero cancellation arose from loss of controllability or from loss of observability, or both. In this section we will make the argument a bit more precise.

The system equations as stated earlier are:

$$\ddot{Mx} + Kx = F$$

and

$$\ddot{q} + \Lambda^2 q = \Phi^T F \quad (C-13)$$

where

$$x = \Phi q \quad (C-14)$$

and  $\phi$  is the eigenvector (mode shape) matrix. Here  $x$  represents physical coordinates, and  $q$  the modal coordinates. For illustrative purposes, consider a 3-dimensional system with  $x = [x_1 \ x_2 \ x_3]^T$ ,  $q = [q_1 \ q_2 \ q_3]^T$ ,  $F = [F_1 \ F_2 \ F_3]^T$ , and

$$\phi = \begin{bmatrix} \phi_{11} & \phi_{21} & \phi_{31} \\ \phi_{12} & \phi_{22} & \phi_{32} \\ \phi_{13} & \phi_{23} & \phi_{33} \end{bmatrix}$$

Here  $[\phi_{i1} \ \phi_{i2} \ \phi_{i3}]^T$  represents the  $i$ th mode shape. Now, Eq. (C-13) can be written as follows

$$\begin{bmatrix} \ddot{q}_1 + \omega_1^2 q_1 \\ \ddot{q}_2 + \omega_2^2 q_2 \\ \ddot{q}_3 + \omega_3^2 q_3 \end{bmatrix} = \begin{bmatrix} \phi_{11} & \phi_{12} & \phi_{13} \\ \phi_{21} & \phi_{22} & \phi_{23} \\ \phi_{31} & \phi_{32} & \phi_{33} \end{bmatrix} \begin{bmatrix} F_1 \\ F_2 \\ F_3 \end{bmatrix}$$

From this it is clear that for  $q_m$  to be influenced by  $F_j$  we must have  $\phi_{mj} \neq 0$  (this is the controllability issue).

Similarly, Eq. (C-14) can be written

$$\begin{bmatrix} x_1 \\ x_2 \\ x_3 \end{bmatrix} = \begin{bmatrix} \phi_{11} & \phi_{21} & \phi_{31} \\ \phi_{12} & \phi_{22} & \phi_{32} \\ \phi_{13} & \phi_{23} & \phi_{33} \end{bmatrix} \begin{bmatrix} q_1 \\ q_2 \\ q_3 \end{bmatrix}$$

From this we see that for  $q_m$  to influence the output at  $x_k$  we must have  $\phi_{mk} \neq 0$  (this is the observability issue).

Now consider an  $n$ -dimensional system. The transfer function between the Force  $F_j$  and output  $x_k$  was found before (see Eq. (C-7)). For the

undamped case we have:

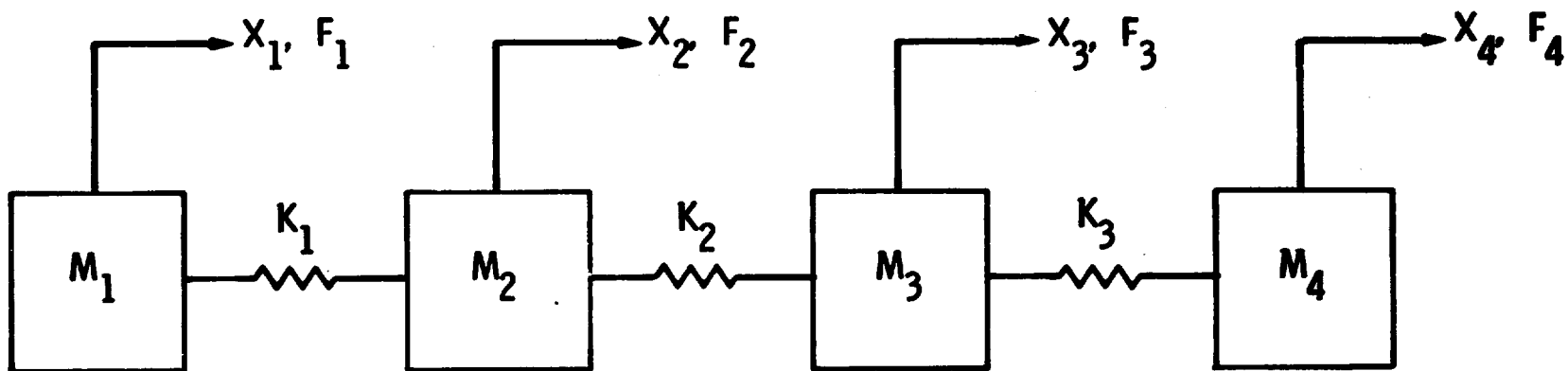
$$\begin{aligned} \frac{x_k}{F_j}(s) &= \sum \frac{\phi_{1j}\phi_{1k}}{s^2 + \omega_1^2} \\ &= \frac{\phi_{1j}\phi_{1k}}{s^2 + \omega_1^2} + \dots + \frac{\phi_{mj}\phi_{mk}}{s^2 + \omega_m^2} + \dots + \frac{\phi_{nj}\phi_{nk}}{s^2 + \omega_n^2} \end{aligned} \quad (C-15)$$

Now, if either  $\phi_{mj} = 0$  or  $\phi_{mk} = 0$ , then the term involving  $s^2 + \omega_m^2$  disappears (i.e., the transfer function has no pole at  $s^2 + \omega_m^2$ ). Hence, if  $\frac{x_k}{F_j}(s)$  is written with the term  $s^2 + \omega_m^2$  in its denominator, it must have the same term in the numerator. In other words, we must have pole zero cancellation. Hence, we can examine the entries in the eigenvector matrix to determine controllability and observability; or we can look for pole zero cancellations in the transfer functions and if they occur look at the eigenvector matrix to determine their cause.

The discussion in this section and the last has implicitly assumed that the natural frequencies are distinct. If they are not distinct (for example we may have several rigid body modes) then our comments must be modified slightly.

Looking at Eq. (C-15) we see that pole zero cancellation will certainly occur if  $\phi_{mj} = 0$  or  $\phi_{mk} = 0$ . However, if  $\omega_1 = \omega_2$  (for example) then it is possible to have pole zero cancellation even when  $\phi_{1j}\phi_{1k}$  and  $\phi_{2j}\phi_{2k}$  are non-zero. Thus  $\phi_{mj} \neq 0$ ,  $\phi_{mk} \neq 0$  is necessary for controllability/observability but not sufficient. If, however,  $\phi_{mj}\phi_{mk} \neq 0$  and  $\omega_m$  is a distinct (nonrepeated) eigenvalue, then this mode will be controllable and observable ( $\phi_{mj}\phi_{mk} \neq 0$  is necessary and sufficient). For additional discussion on this topic the reader is referred to Ref. 2-1.





$X_i$  = INERTIA DISPLACEMENT AT MASS  $M_i$   
 $F_i$  = FORCE APPLIED AT MASS  $M_i$

Fig. C-1. Discrete Mass System

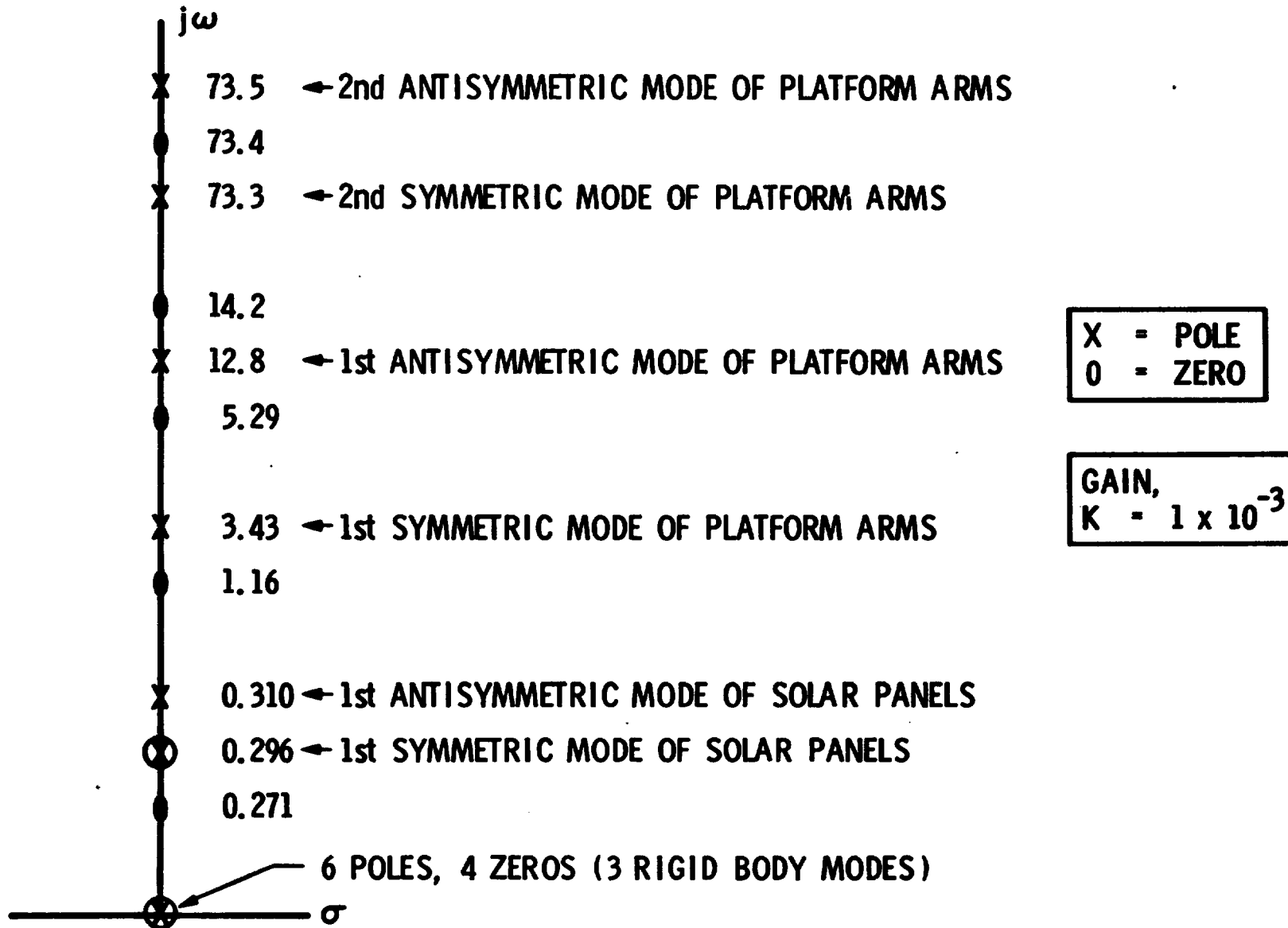


Fig. C-2. Pole/Zero Configuration for  $\theta_1/T_1(s)$

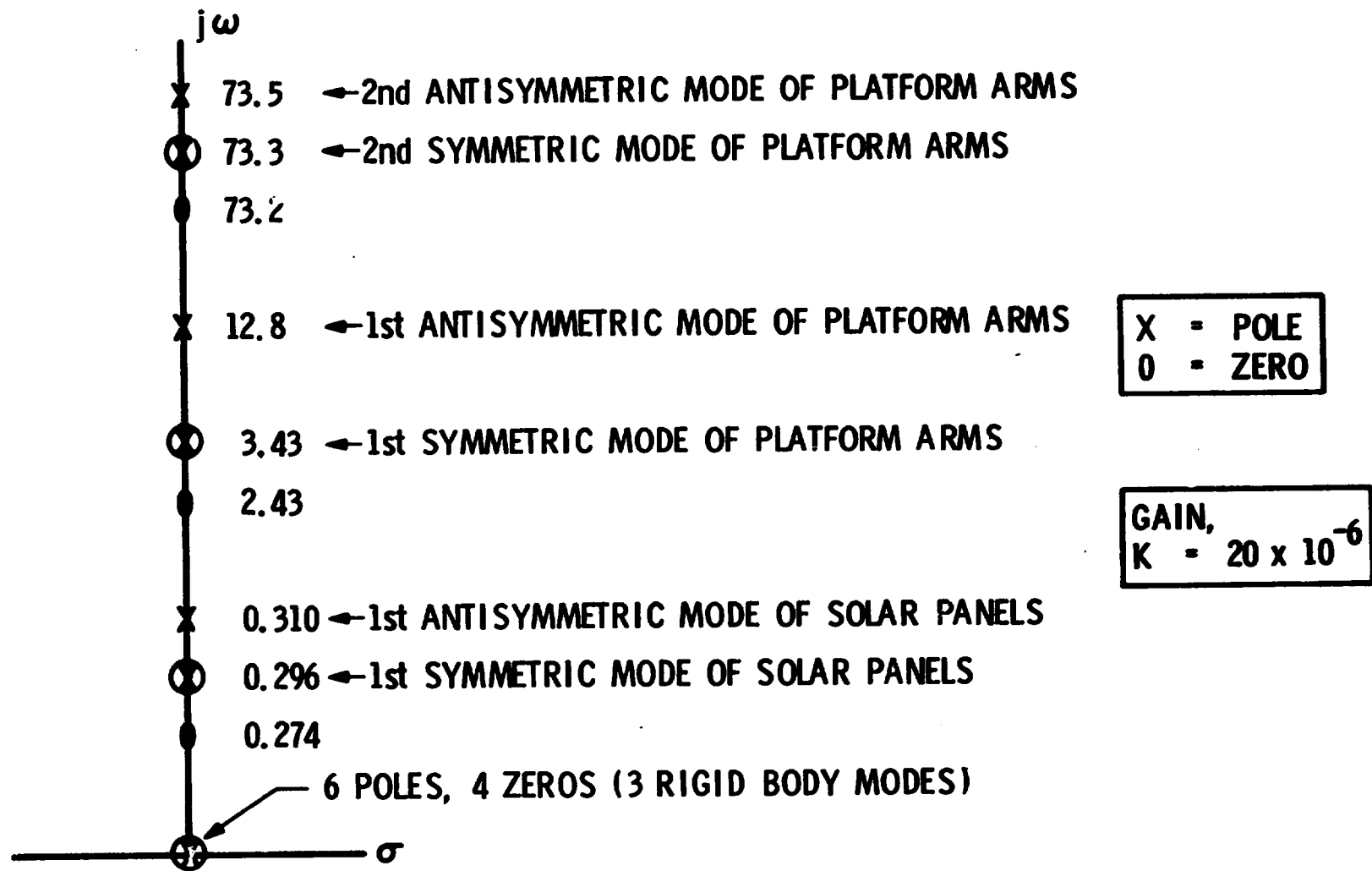


Fig. C-3. Pole/Zero Configuration for  $\theta_2/T_2(s)$

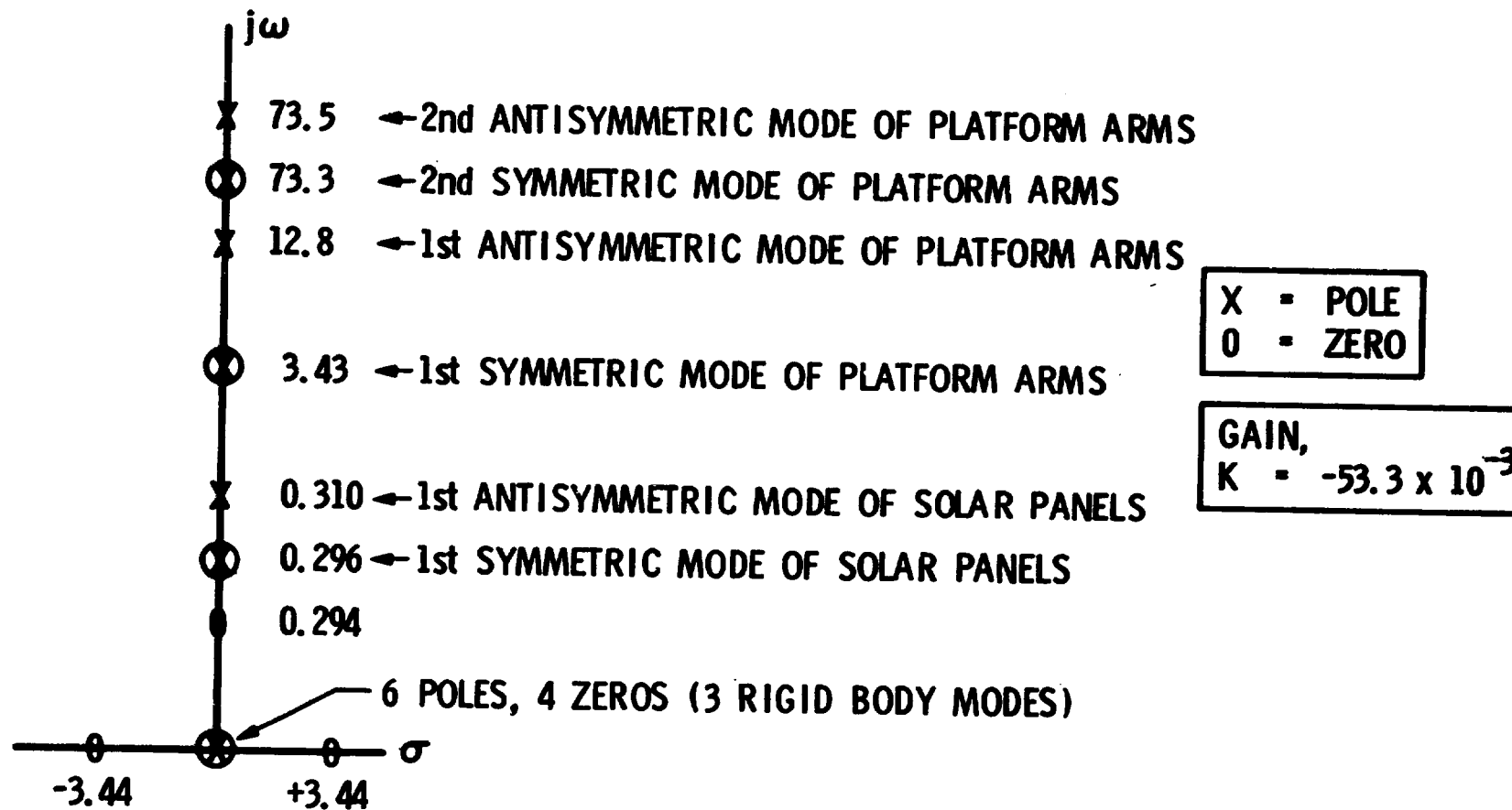


Fig. C-4. Pole/Zero Configuration for  $\theta_1/T_2(s)$  and  $\theta_2/T_1(s)$

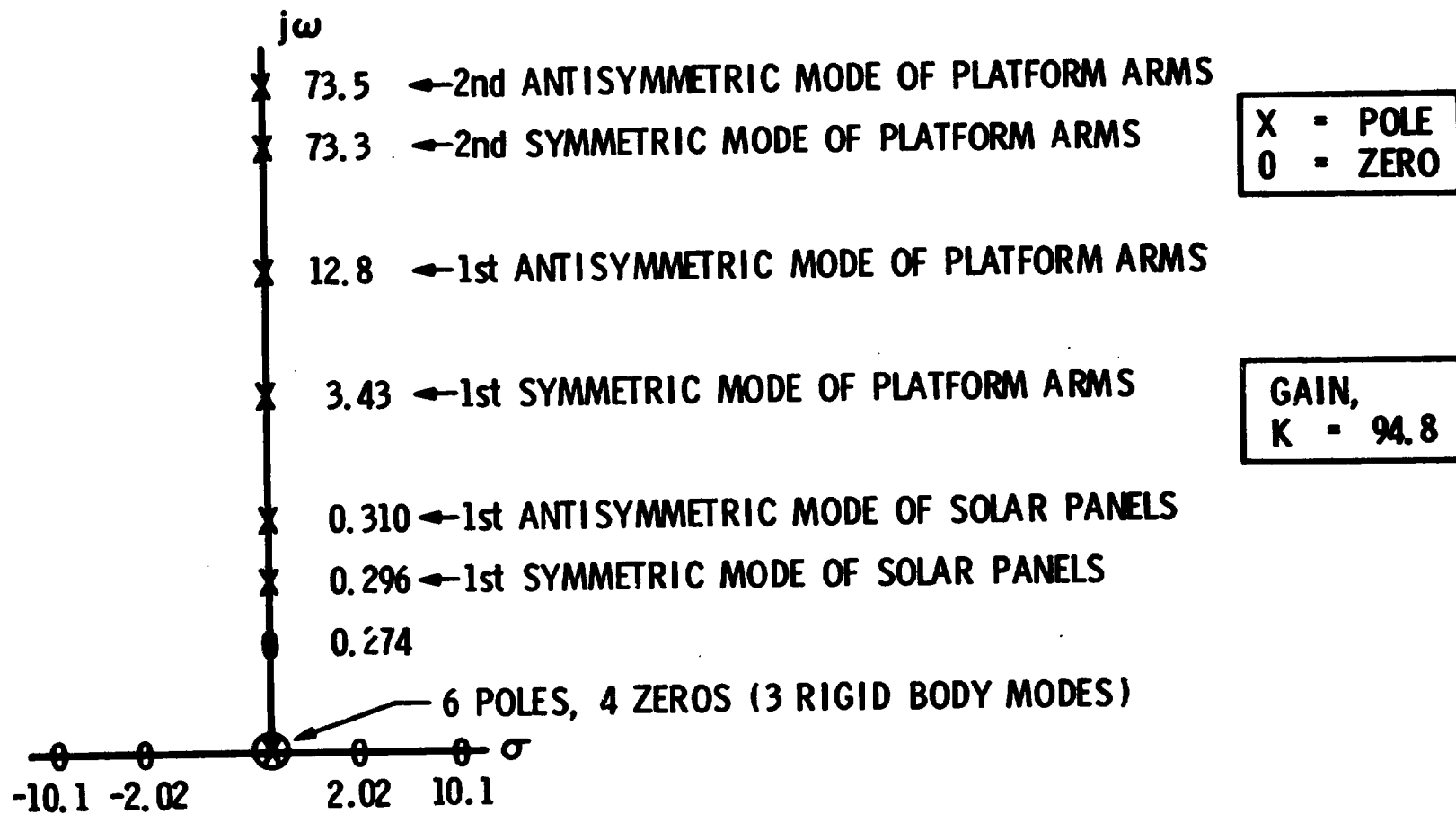


Fig. C-5. Pole/Zero Configuration for  $\theta_1/T_3(S)$  and  $\theta_3/T_1(S)$

## APPENDIX D. MODEL FOR PLATFORM WITH TWO HINGED EXPERIMENTS ATTACHED

This Appendix extends the model of Appendix B to include two hinged experiment packages, each having a single rotational degree of freedom. It is assumed that these packages are rigid. The resulting model has eleven degrees of freedom. The mass and stiffness matrix for the combined system is given.

### 1. Configuration

Figure 2-1 shows the configuration for the Reference Platform. This configuration is the same as that in Appendix B except for the two experiment packages represented by the masses  $M_{e1}$ ,  $M_{e3}$ . The additional degrees of freedom are given by the angles  $\gamma_1$  and  $\gamma_3$ .  $\gamma_1$  and  $\gamma_3$  are taken to positive for a rotation about the plus x axis.  $\gamma_1$  is measured from the negative y axis and  $\gamma_3$  is measured from the positive y axis (i.e. for the nominal configuration shown in Fig. 2-1, both  $\gamma_1$  and  $\gamma_3$  are zero).

### 2. Development of Equations of Motion for an Experiment Package

Figure D-1 shows a sketch of the experiment packages located on the y axis of the platform arm. Figure D-2 shows a free body diagram. The model developed will be for  $\gamma_1$  and  $\gamma_3$  near zero so that forces along the y axis will not be considered. Symbols are defined as follows:

$T_3$  = torque applied about the x axis of the experiment package located on the plus y axis.

$F_{v3}$  = reaction force applied by the base mount to the hinge point ( $P_3$ ) of the experiment package in the direction of the z axis.

$P_3$  = point of force application

$\gamma_3$  = angle of rotation about the x axis relative to the inertially fixed axis y.

$V_3$  = inertial displacement of point  $P_3$  along z axis.

$M_{e3}$  = mass of experiment package at location 3.

$I_{e3}$  = inertia of experiment package about hinge point  $P_3$ .

$L_{e3}$  = distance between hinge point  $P_3$  and center of mass of experiment.

$T_1$ ,  $F_{v1}$ ,  $P_1$ ,  $\gamma_1$ ,  $V_1$ ,  $M_{e1}$ ,  $L_{e1}$  are defined similarly.

Now, if the point  $P_3$  were initially fixed, then we would have

$$T_3 = I_{e3} \ddot{\gamma}_3$$

But, since  $P_3$  is not fixed we must account for the base acceleration. The proper relationship in this case is (Ref. D-1, p. 146)

$$\underline{M}_{-p} = \underline{\rho}_{-c} \times M \ddot{\underline{r}}_{-p} = \dot{\underline{H}}_{-p} \quad (D-1)$$

where

- $\underline{M}_{-p}$  = torque about point  $P_3$
- $\underline{\rho}_{-c}$  = vector from point  $P_3$  to cm
- $M$  = mass =  $M_{e3}$
- $\ddot{\underline{r}}_{-p}$  = acceleration of point  $P_3$  relative to inertial space
- $\dot{\underline{H}}_{-p}$  = rate of change of angular momentum relative to point  $P_3$ .

The model being considered will consider only motion along the z axis and rotation about the x axis (actually there is also rotation about the y axis because of x-y axis coupling but this effect will be neglected in what follows).

For  $\gamma_3$  near zero we have

$$\begin{aligned} \underline{M}_{-p} &= T_3 \underline{e}_x \\ \underline{\rho}_{-c} &= L_{e3} (\underline{e}_y + \gamma_3 \underline{e}_z) \\ \ddot{\underline{r}}_{-p} &= \ddot{V}_3 \underline{e}_z \\ \dot{\underline{H}}_{-p} &= I_{e3} \ddot{\gamma}_3 \underline{e}_x \end{aligned}$$

The assumption here is that x is a principal axis for the experiment package and that base motion is along z only.  $\underline{e}_x$ ,  $\underline{e}_y$ , and  $\underline{e}_z$  are unit vectors along the x, y, and z axes respectively.

Substitution into Eq. (D-1) gives

$$T_3 \underline{e}_x = L_{e3} (\underline{e}_y + \gamma_3 \underline{e}_z) \times M_{e3} \ddot{V}_3 \underline{e}_z = I_{e3} \ddot{\gamma}_3 \underline{e}_x \quad (D-2)$$

or

$$T_3 - M_{e3} L_{e3} \ddot{V}_3 = I_{e3} \ddot{\gamma}_3$$

$$T_3 = M_{e3} L_{e3} \ddot{V}_3 + I_{e3} \ddot{\gamma}_3 \quad (D-3)$$

Now, we can obtain the force equation by application of Newton Law.

$$F_{v3}e_z = M_{e3} \times (\text{acceleration of CM of experiment package})$$

Since the position of the CM of the experiment package relative to inertial space is given by  $(V_3 + \gamma_3 L_{e3}) e_z$  we have

$$F_{v3} = M_{e3} (\ddot{V}_3 + L_{e3} \ddot{\gamma}_3) \quad (D-4)$$

Equations (D-3) and (D-4) gave the force and torque applied to the experiment package at point  $P_3$ . The force and torque applied to the platform arm at this point is the same with a minus sign.

For the experiment package on the  $-y$  axis of the platform arm Eqs. (D-3) and (D-4) must be modified slightly. Equation (D-2) becomes

$$T_1 e_x - L_{e1} (-e_y - \gamma_1 e_z) \times M_{e1} \ddot{V}_1 e_z = I_{e1} \ddot{\gamma}_1 e_x \quad (D-5)$$

or

$$T_1 = -M_{e1} L_{e1} \ddot{V}_1 + I_{e1} \ddot{\gamma}_1 \quad (D-6)$$

Also, since the CM position for this experiment package is  $(V_1 - \gamma_1 L_{e1}) e_z$  we have

$$F_{v1} = M_{e1} (\ddot{V}_1 - \ddot{\gamma}_1 L_{e1}) \quad (D-7)$$

To summarize what we have so far:

For the experiment package on  $+y$  axis (location 3) the forces and torque applied to the experiment package are

$$T_3 = M_{e3} L_{e3} \ddot{V}_3 + I_{e3} \ddot{\gamma}_3$$

$$F_{v3} = M_{e3} (\ddot{V}_3 + L_{e3} \ddot{\gamma}_3)$$

For the experiment package on  $-y$  axis (location 1) the forces and torques applied to the experiment package are

$$T_1 = -M_{e1} L_{e1} \ddot{V}_1 + I_{e1} \ddot{\gamma}_1$$

$$F_{v1} = M_{e1} (\ddot{V}_1 - L_{e1} \ddot{\gamma}_1)$$

The forces and torques applied to the bus are of opposite sign.



### 3. The Mass Matrix

Define the new state variable vector to be

$$[V_1 V_2 V_3 \theta_1 \theta_3 \theta_2 V_4 V_5 V_6 \gamma_1 \gamma_3]^T$$

The equations of interest are:

$$\begin{aligned} F_1 &= F_{a1} + F_{e1} \\ &= F_{a1} - M_{e1} (\ddot{V}_1 - L_{e1} \ddot{\gamma}_1) \end{aligned} \quad (D-8)$$

$$\begin{aligned} F_3 &= F_{a3} + F_{e3} \\ &= F_{a3} - M_{e3} (\ddot{V}_3 + L_{e3} \ddot{\gamma}_3) \end{aligned} \quad (D-9)$$

$$F_4 = F_{a4} - T_1 \quad (D-10)$$

$$F_5 = F_{a5} - T_3 \quad (D-11)$$

$$F_{10} = -M_{e1} L_{e1} \ddot{V}_1 + I_{e1} \ddot{\gamma}_1 = T_1 \quad (D-12)$$

$$F_{11} = M_{e3} L_{e3} \ddot{V}_3 + I_{e3} \ddot{\gamma}_3 = T_3 \quad (D-13)$$

where

$F_1$  = sum of external forces ( $F_{a1}$ ) and experiment package reaction forces ( $F_{e1} = -F_{v1}$ ) applied to  $M_1$ .

$F_3$  = sum of external forces ( $F_{a3}$ ) and experiment package reaction forces ( $F_{e3} = -F_{v3}$ ) applied to  $M_3$ .

$F_4$  = sum of external torques ( $F_{a4}$ ) and experiment package reaction torques ( $-T_1$ ) applied to  $I_1$ .

$F_5$  = sum of external torques ( $F_{a5}$ ) and experiment package reaction torques ( $-T_3$ ) applied to  $I_3$ .

$F_{10} = T_3$  = torque applied to experiment package at location 3 about hinge point  $P_3$ .

$$\begin{aligned} \text{Now, let } m_{ij} \quad & i = 1,9 \\ & j = 1,9 \end{aligned}$$

be the mass matrix elements of Appendix B. Then, by using Eqs. (D-8) to

(D-13) we can obtain the new mass matrix as

$$m'_{11} = m_{11} + M_{e1}$$

$$m'_{33} = m_{33} + M_{e3}$$

$$m'_{1,10} = -M_{e1}L_{e1}$$

$$m'_{3,11} = M_{e3}L_{e3}$$

$$m'_{10,10} = I_{e1}$$

$$m'_{11,11} = I_{e3}$$

$$m'_{10,1} = m'_{1,10}$$

$$m'_{11,3} = m'_{3,11}$$

$$m'_{10,j} = 0 \quad \text{for all } j \text{ except } 1 \text{ and } 10$$

$$m'_{11,j} = 0 \quad \text{for all } j \text{ except } 3 \text{ and } 11$$

$$m'_{i,10} = 0 \quad \text{for all } i \text{ except } 1 \text{ and } 10$$

$$m'_{i,11} = 0 \quad \text{for all } i \text{ except } 3 \text{ and } 11$$

$$m'_{ij} = m_{ij} \quad \text{for all other } i \text{ and } j.$$

#### 4. The Stiffness Matrix

The stiffness matrix is unchanged from that of Appendix B except for the addition of zero elements to increase the dimension from 9 to 11. This is because the rotations  $\gamma_1$  and  $\gamma_3$  can be made without any strain energy (i.e. there are no forces or torques proportional to  $\gamma_1$  or  $\gamma_3$ ).

Hence, the new stiffness matrix is given by

$$k'_{ij} = k'_{ij} \quad i = 1,9$$

$$j = 1,9$$

$$k'_{10,j} = k'_{11,j} = k'_{1,10} = k'_{1,11} = 0$$

for  $i = 1,11$

$$j = 1,11$$

C-2

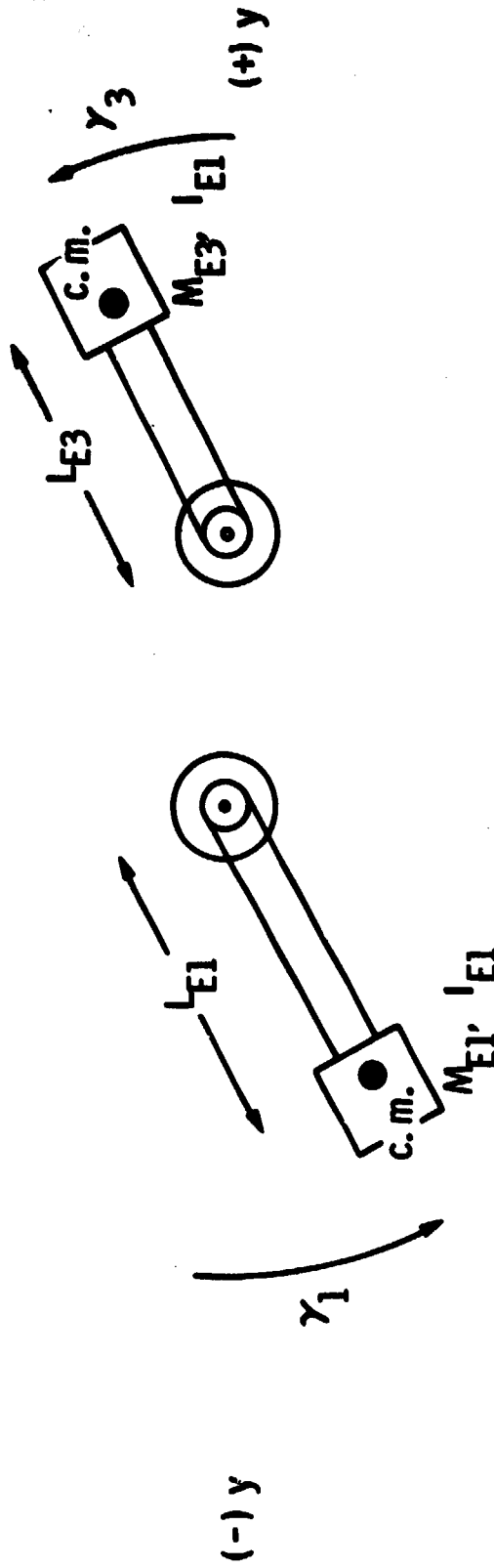


Fig. D-1. Experiment Package Configurations

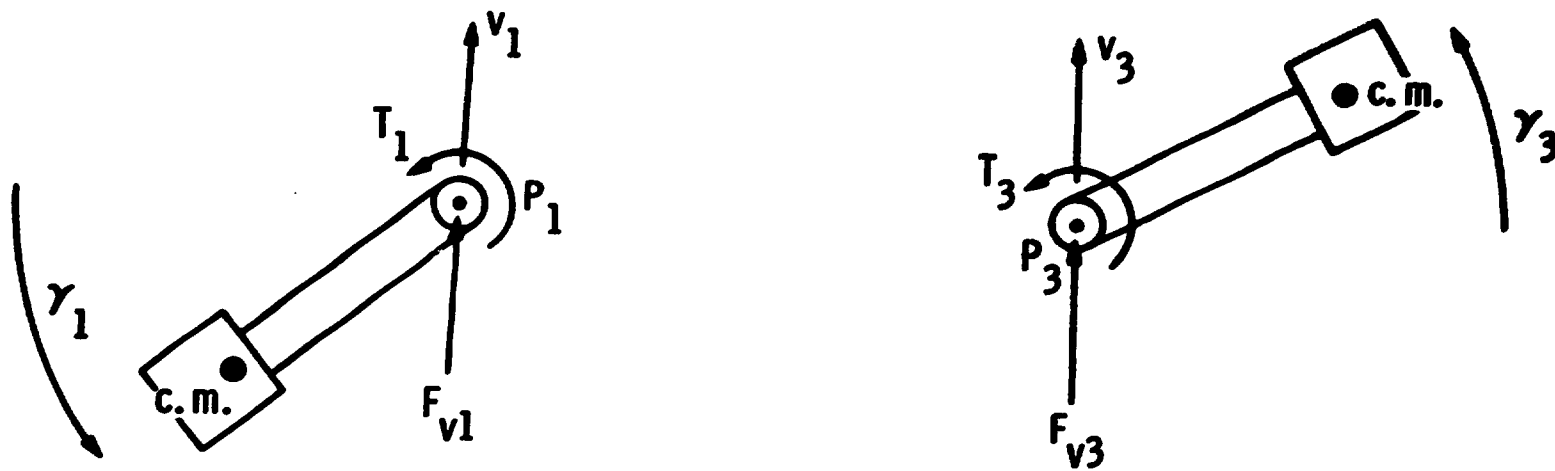


Fig. D-2. Free Body Diagram for Experiment Packages

## APPENDIX E. A TECHNIQUE FOR RESHAPING THE RIGID BODY MODES OF A SPACECRAFT

This Appendix presents a technique which can be used to reshape the eigenvectors associated with a common eigenvalue. This is of particular interest for application to reshaping rigid body mode shapes for flexible spacecraft. Standard eigenvalue/eigenvector programs do not necessarily give rigid body mode shapes which are pleasing. The algorithm presented here allows considerable freedom for reshaping the modes.

### 1. System Equations

The system to be considered is of the form

$$M\ddot{x} + Kx = 0$$

where  $M$  is the system mass matrix (symmetric, positive definite)

$K$  is the stiffness matrix (symmetric, positive semidefinite)

$x$  is the coordinate vector (dimension  $n$ )

Suppose we set  $x = \phi q$

where  $\phi$  satisfies

$$\phi^T M \phi = I_n \tag{E-1}$$

$$\phi^T K \phi = \Lambda^2 \tag{E-2}$$

$$\Lambda^2 = \text{diag.} (\lambda_1^2, \lambda_2^2, \dots, \lambda_n^2)$$

$I_n$  = Identity matrix

$\phi$  is the matrix of system eigenvectors, or mode shapes.  $\Lambda$  is the matrix of system natural frequencies.

### 2. Reshaping Algorithm

Suppose the first  $m$  eigenvalues are repeated (for example, all zero for the rigid body modes).

$$\text{Set } \phi = [\phi_1 \ \phi_2 \ \dots \ \phi_n]$$

where  $\phi_1$  is the  $i^{\text{th}}$  eigenvector. Then suppose we wish to reshape  $\phi_1, \phi_2, \dots, \phi_m$ . In particular suppose  $\phi_j = [\phi_{1j} \phi_{2j} \dots \phi_{nj}]^T$  and suppose we wish to eliminate  $\phi_{1j}$  for some  $i$  and for each  $j$

$$j = 2, 3, \dots, m.$$

In other words, we wish only  $\phi_1$  to contain the component  $i$ :

$$\phi_{11} \neq 0, \quad \phi_{1j} = 0 \quad j = 2, 3, \dots, m.$$

We can accomplish this by proceeding as follows:

First eliminate  $\phi_{12}$  from  $\phi_2$ . This can be accomplished by setting

$$\hat{\phi}_2 = \phi_2 + a \phi_1$$

$$\text{where } a = -\frac{\phi_{12}}{\phi_{11}}$$

now  $\hat{\phi}_2$  and  $\phi_1$  are no longer orthogonal with respect to  $M$  and  $K$  so we must modify  $\phi_1$ . So set  $\hat{\phi}_1 = \phi_1 + b \phi_2$ . Then to maintain the orthogonality conditions of Eqs. (E-1) and (E-2) we must have

$$\hat{\phi}_1^T M \hat{\phi}_2 = 0 \tag{E-3}$$

$$\hat{\phi}_1^T K \hat{\phi}_2 = 0 \tag{E-4}$$

so we must have

$$(\phi_1^T + b \phi_2^T) M (\phi_2 + a \phi_1) = 0$$

$$\text{or } a \phi_1^T M \phi_1 + b \phi_2^T M \phi_2 = 0$$

$$\text{so that } b = -a \frac{\phi_1^T M \phi_1}{\phi_2^T M \phi_2} = -a$$

likewise we must have

$$(\phi_1^T + b \phi_2^T) K (\phi_2 + a \phi_1) = 0$$

$$\text{or } b \phi_2^T K \phi_2 + a \phi_1^T K \phi_1 = 0$$

but if  $\phi_2^T K \phi_2 = \phi_1^T K \phi_1 = \lambda_1^2$  then again  $b = -a$  does it.

Now note that

$$\begin{aligned} (\phi_1^T + b \phi_2^T) M (\phi_1 + b \phi_2) &= \phi_1^T M \phi_1 + b^2 \phi_2^T M \phi_2 \\ &= 1 + b^2 = 1 + a^2 \end{aligned}$$

and

$$\begin{aligned} (\phi_2^T + a \phi_1^T) M (\phi_2 + a \phi_1) &= \phi_2^T M \phi_2 + a^2 \phi_1^T M \phi_1 \\ &= 1 + a^2 \end{aligned}$$

So to renormalize  $\hat{\phi}_1$  and  $\hat{\phi}_2$  we must divide each of them by  $\sqrt{1 + a^2}$ .

This results in the following:

$$\begin{aligned} \hat{\phi}_1 &= (\phi_1 - a \phi_2) / (\sqrt{1 + a^2}) \\ \hat{\phi}_2 &= (\phi_2 + a \phi_1) / (\sqrt{1 + a^2}) \\ \text{where } a &= -\frac{\phi_{12}}{\phi_{11}} \end{aligned}$$

This procedure can now be repeated using  $\hat{\phi}_1$  and  $\phi_3$  to eliminate the component  $\phi_{13}$  from  $\phi_3$ , and so on until we have a new set of  $m$  rigid body eigenvectors, only one of which has the component  $\phi_{ij} \neq 0$ .

Now we can work with  $m-1$  eigenvectors, and eliminate a different coordinate from all but one of these; and so on until for the  $m^{\text{th}}$  eigenvector  $m-1$  components have been eliminated. This procedure is illustrated in Fig. E-1 for the case  $M = 5$ . Note that at each step any one coordinate can be eliminated from the remaining eigenvectors. These coordinates need not be consecutive as shown in Fig. E-1.

### 3. A Property of the Reshaping Algorithm

Suppose that  $\phi_1$  is to be used to eliminate  $\phi_{12}$  from  $\phi_2$ . Then we can show that  $\hat{\phi}_{11}$  has the same magnitude as  $\phi_{11}$ .



In particular we have

$$\begin{aligned}\hat{\phi}_1 &= (\phi_1 - a \phi_2) / (\sqrt{1 + a^2}) \\ &= (\phi_1 + \frac{\phi_{12}}{\phi_{11}} \phi_2) / (\sqrt{1 + (\frac{\phi_{12}}{\phi_{11}})^2})\end{aligned}$$

so that

$$\begin{aligned}\hat{\phi}_{11} &= (\phi_{11} + \frac{\phi_{12}}{\phi_{11}} \phi_{12}) / (\sqrt{1 + \frac{\phi_{12}^2}{\phi_{11}^2}}) \\ \frac{\hat{\phi}_{11}}{\phi_{11}} &= (1 + \frac{\phi_{12}^2}{\phi_{11}^2}) / (\sqrt{1 + \frac{\phi_{12}^2}{\phi_{11}^2}}) \\ &= \sqrt{1 + a^2}\end{aligned}$$

This property shows us that if  $\phi_1$  begins with a large value for  $\phi_{11}$  then it will still have this large value after the reshaping process. In other words, we are assured of a certain amount of computational stability.

#### 4. Examples of Ways in Which the Reshaping Algorithm Can Be Used

As an illustration of how the reshaping algorithm might be applied consider the following example. Suppose the rigid body modes for a spacecraft include rotation and translation of the Center of Mass (CM). An attitude control system does not control CM translation. If there are 3 CM translational coordinates for the spacecraft, then it would be desirable to eliminate CM translation from all but 3 of the rigid body modes. This can be accomplished using the reshaping algorithm of this appendix provided that the eigenvectors contain coordinates defining the CM location. If the

eigenvectors do not contain the CM coordinates, then they can be augmented so that they do by using the mass properties of the spacecraft.

If the CM translations are not eliminated from the eigenvectors used to design an attitude control system, then there will be uncontrollable modes associated with the design problem. These uncontrollable modes can be eliminated by reshaping followed by truncation.

As a second example consider the following control problem. Suppose we wish to design an attitude control system for a single spacecraft axis using classical design techniques. If the spacecraft model has 3 rigid body rotational degrees of freedom then two of these are uncontrollable when performing a single-axis design. If the actuator/sensor pair used to accomplish single-axis control is colocated, then we can eliminate the rotational coordinate with which they are associated from all but one rigid body mode using the reshaping algorithm. If they are not colocated we could choose either the coordinate associated with the actuator or the one associated with the sensor and eliminate it from all but one mode. In this way we can eliminate two rigid body rotational modes from the spacecraft model which are either uncontrollable, unobservable, or both uncontrollable and unobservable. Through this process we can achieve a cleaner mathematical system model for use in the control design problem.

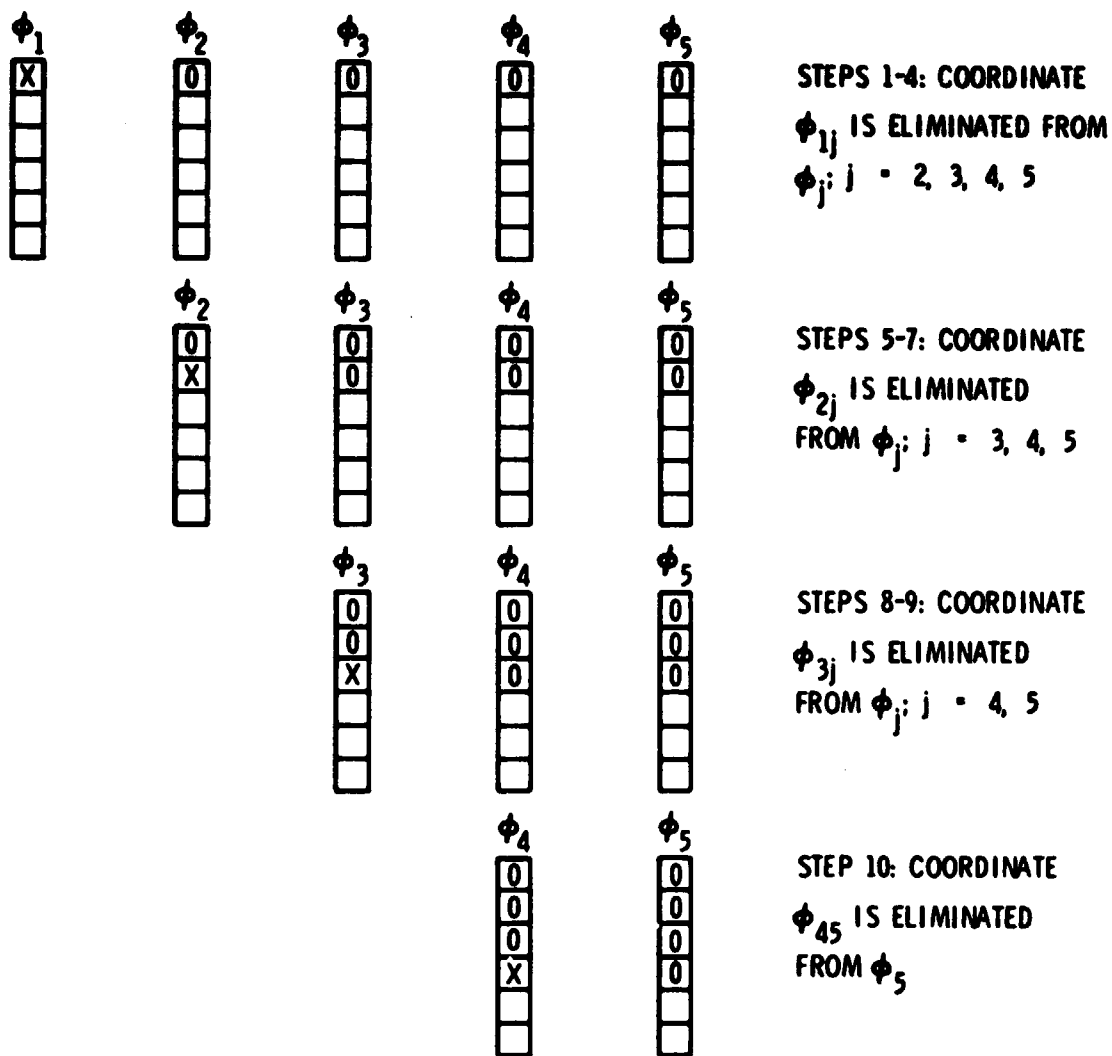


Fig. E-1. Reshaping Process for Mode Shapes Having Identical Eigenvalues

## APPENDIX F. TIME RESPONSE PLOTS FOR RUN F10

In this Appendix time plots are presented which illustrate the transient response for a representative simulation (Run F10 of Table 4-1). Simulations were conducted using ACSL (Advanced Continuous Simulation Language) on an 1100/81 Univac computer.

Figure F-1 shows the experiment 1 actuator torque and angular response.

Figure F-2 shows the central bus actuator torque and angular response.

The actuator torque and angular response of experiment 3 is shown in Fig. F-3. Comments on individual plots follow.

### 1. Figure F-1

The actuator torque ( $T_1$ ) and angular response ( $\gamma_1$ ) for experiment 1 are shown in Fig. F-1. The commanded torques ( $T_{c1}$ ) for this run were +20 N-m for the first 14 seconds, -20 N-m for the next 14 seconds, and zero thereafter. The commanded angle ( $\gamma_{c1}$ ) was consistent with this. The actual torque applied shows the strong influence of the structural elastic response fed back to the controller by the rate and position sensor. The two dominant frequencies seen in the torque curve are at .30 rad/s (.048 Hz) and 2.8 rad/s (.45 Hz). Note that the time plot results of Fig. F-1 agree with the closed loop eigenvalues plotted in Fig. 4-6. Figure 4-6 along with Table 2-2 show that the .3-rad/s frequency is associated with the solar panel asymmetric mode (open loop .4-rad/s) and that the 2.8-rad/s frequency is associated with the arm symmetric mode (open loop 5.7 rad/s).

### 2. Figure F-2

The actuator torque ( $T_2$ ) and angular response ( $\theta_2$ ) are shown in Fig. F-2. The commanded angle ( $\theta_{c2}$ ) was zero. The primary response is a rigid body rotation which occurs because the bus controller frequency is low (0.01 Hz) compared to the frequency of the disturbance input. The only structural vibration frequency evident in this plot is at .048 Hz and is associated with the solar panel asymmetric mode.

### 3. Figure F-3

The actuator torque ( $T_3$ ) and angular response ( $\gamma_3$ ) are shown in Fig. F-3. The commanded angle ( $\gamma_{c3}$ ) was zero. The frequency content of  $T_3$  is very similar to that of  $T_1$  for this run. In fact, after about 40 seconds, the two torques are almost identical. Both of these torques show the influence of the structural vibrations associated with the solar panel asymmetric mode (.048 Hz) and the arm symmetric mode (.45 Hz). Note that the oscillation caused by the solar panel asymmetric mode is  $\pm 1$   $\mu$ rad at the 100-second point of this plot. This oscillation all by itself is well in excess of the .05- $\mu$ rad pointing requirement presented in Table 3-1.

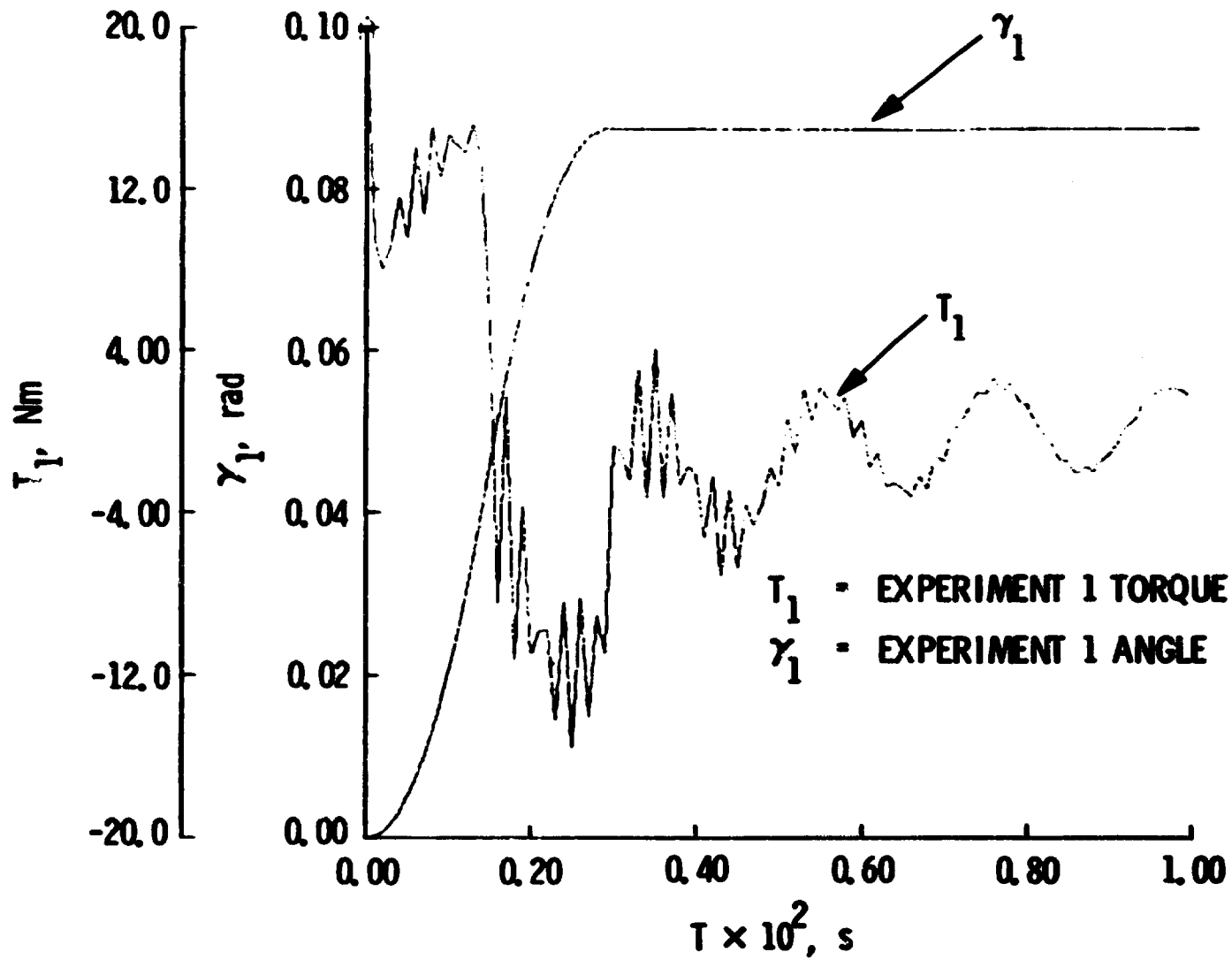


Fig. F-1. Actuator Torque and Angular Response for Experiment 1, Run F-10.

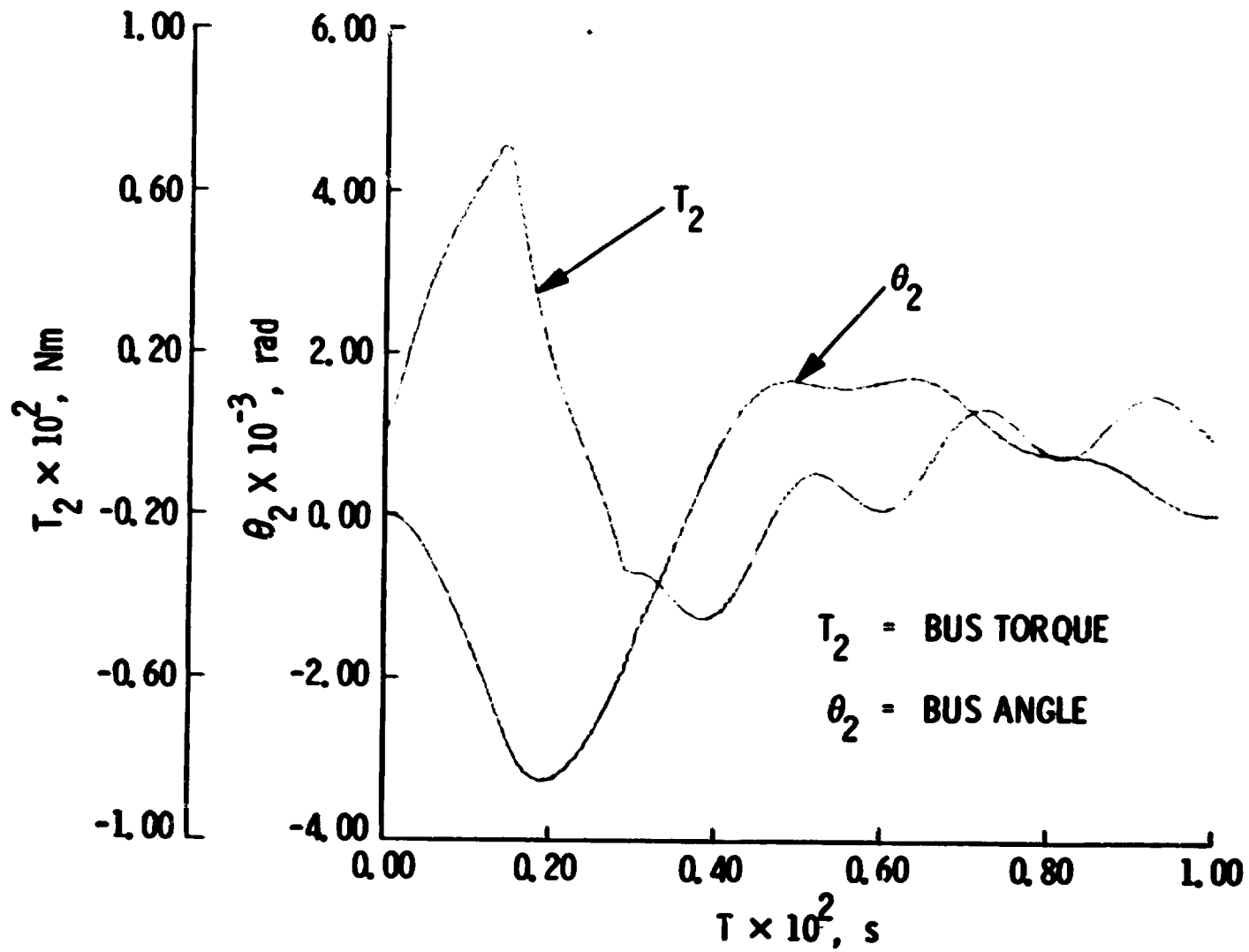


Fig. F-2. Actuator Torque and Angular Response for Central Bus, Run F-10.

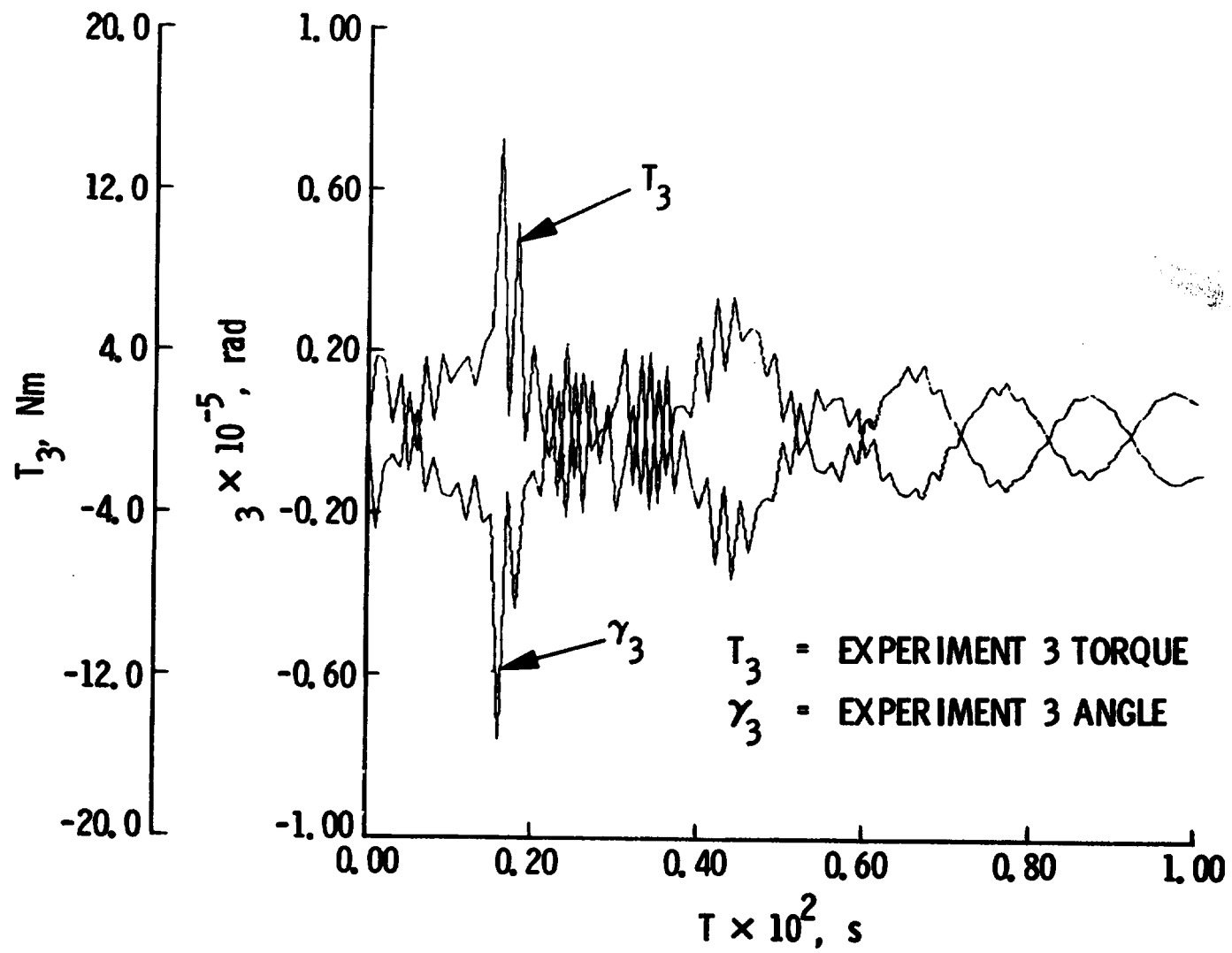


Fig. F-3. Actuator Torque and Angular Response for Experiment 3, Run F-10.



## REFERENCES

- 2-1. P.C. Hughes and R.E. Skelton, "Stability, Controllability, and Observability of Linear Matrix-Second-Order Systems," in Proceedings of the Joint Automatic Control Conference (JACC), American Institute of Chemical Engineers, New York, N.Y., June 1979.
- A-1. R.W. Clough, and J. Penzien, Dynamics of Structures, Mc-Graw-Hill, New York, N.Y., 1975.
- A-2. Handbook of Engineering Fundamentals, O.W. Eshbach - Editor, Third Edition, John Wiley and Sons, New York, N.Y., 1975.
- C-1. E.P. Popov, Introduction to Mechanics of Solids, Prentice-Hall, Englewood Cliffs, N.J., 1968.
- D-1. D.T. Greenwood, Principles of Dynamics, Prentice-Hall, Englewood Cliffs, N.J., 1965.